Study on Tritium Behavior in the WCCB Blanket Using LTZO Ceramic Pebbles

一本杉, 旭人

Ph.D. Dissertation

Study on Tritium Behavior in the WCCB Blanket Using LTZO Ceramic Pebbles

Akito Ipponsugi

March 2024

KYUSHU
UNIVERSITY

Table of Contents

Abstract

DT fusion reactors, being expected as a next-generation energy source, rely on a significant quantity of tritium, a radioactive isotope of hydrogen, as its principal fuel. Since the natural abundance of tritium is only about 3 kg, it is imperative to establish a self-sufficient tritium fuel cycle. This cycle encompasses the processes of production, recovery, separation, purification, storage, and delivery of tritium to the reactor. In each component of the complex fuel cycle, tritium is present dynamically and statically, and its concentration and temperature vary widely by orders of magnitude. In addition, the target tritium throughput far exceeds the tritium throughput that humanity has experienced in the past. Hence, there is an urgent need for tritium engineering research and development efforts. Furthermore, it is imperative to thoroughly evaluate the safety of the tritium fuel cycle as substantial tritium chemical plants, given the increasing social attention and demands for safety associated with nuclear facilities handling radioactive materials.

This study primarily examines blanket and coolant systems among the various cycle components, assuming the newly developed $Li_{2+x}TiO_{3+y}$ + 20 wt% Li_2ZrO_3 (LTZO) ceramic pebbles are loaded into the blanket as an advanced tritium breeding material. This Ph.D. dissertation is devoted to JA-DEMO and divided into three research topics: Li mass loss behavior, tritium release behavior, and tritium permeation behavior. The outline of each chapter is as follows:

Chapter 1 introduces a concise overview of the imperatives and technical complexities of the tritium fuel cycle in DT fusion reactors. Subsequently, it delves into individual study topics, addressing their respective technical concerns and outlining their objectives.

Chapter 2 provides an overview of the essential principles of fusion tritium engineering, for instance, the mass transfer theory and models, intending to enhance comprehension of the subsequent chapters.

Chapter 3 presents the characterization of the LTZO pebbles as advanced tritium breeders from the fusion engineering aspect. The crystal structure of the base material, Li_2TiO_3, and the fabrication process of the LTZO ceramic pebbles are introduced. The literature on Li_2TiO_3 with excess Li anticipates LTZO structure. In addition, the results of XPS, XRD, TDS, SEM-EDX, and specific surface area measurements delineate the LTZO characteristics and determine the stoichiometric ratio of the LTZO.

Chapter 4 discusses the Li mass loss behavior. Experiments quantify the Li mass loss rate and the maximum mass loss. The same fundamental analysis method as in Chapter 2 observes the macroscopic and microscopic structure. Finally, the Li mass loss rate simulates its effects on the tritium production compared with the Li burn-up rate in JA-DEMO.

Chapter 5 discusses the tritium release behavior. Firstly, the theoretical equation characterizes the LTZO pebble from the perspective of nuclear physics. Then, experiments evaluate the tritium release behavior from the as-received and long-term heated LTZO pebbles based on the tritium mass balance and elucidate the tritium release mechanisms.

Chapter 6 comprehensively analyzes the tritium permeation behavior between the high-temperature and high-pressurized water. Experimental results establish the water-to-water tritium permeation model. The experimentally obtained tritium mass transfer coefficients simulate the time variation of the tritium concentration in the primary and secondary cooling water systems. The required design of the tritium-containing water treatment system is obtained based on the tritium mass balance, varying the tritium concentration limits in the primary water coolant.

Chapter 7 concludes the whole dissertation, and then Chapter 8 presents the future outlook of the studies that this dissertation focuses on.

Appendix A and B are complementary additions to the discourse presented in Chapter 5. Appendix A conveys how to calibrate ionization chambers. Appendix B pursues the causes of the tritium recovery gap in theoretical and experimental values using a Monte Carlo simulation code and the heat conduction equation approach.

Chapter 1. Introduction

1.1 Tritium Fuel Cycle

Fusion energy is projected to be game-changing in the middle of this century. DT (Deuterium-Tritium) fusion energy is one of the most promising approaches for achieving sustainable, clean, and abundant power generation. The DT fusion reaction occurs by fusing deuterium and tritium nuclei under extremely high temperatures and high pressure, yielding helium, a neutron, and an enormous amount of energy. The energy released from 1 g of fuel is comparable to that from 8 t of oil.

$$D + T \rightarrow {}^4He \ (3.52 \ MeV) + n \ (14.1 \ MeV) + 17.6 \ MeV \tag{1.1}$$
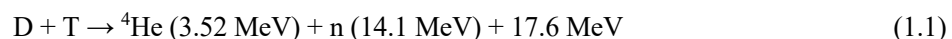
While deuterium is abundant in seawater at 150 ppm and is inexhaustible, unfortunately, tritium is exceedingly scarce at 10^{-12} ppm and is present in only 3 kg. Considering a fusion thermal output of 3 GW, about 450 g of tritium must be consumed daily. Therefore, it is pivotal to establish a self-sufficient tritium fuel cycle, including tritium production, recovery, separation, and purification, where the tritium production rate must be constantly higher than the tritium consumption, loss, and decay. Figure 1.1 illustrates a schematic diagram of the tritium fuel cycle based on the current Japanese demonstration reactor (JA-DEMO) design [1-5]. Based on the previous study [4], brief remarks on each component are given.

Figure 1.1 Schematic diagram of the tritium fuel cycle. Hydrogen isotopes are indicated as Q.
Explicitly, H, D, and T denote hydrogen (^{1}H), deuterium (^{2}H), and tritium (^{3}H), respectively.

- Fueling System

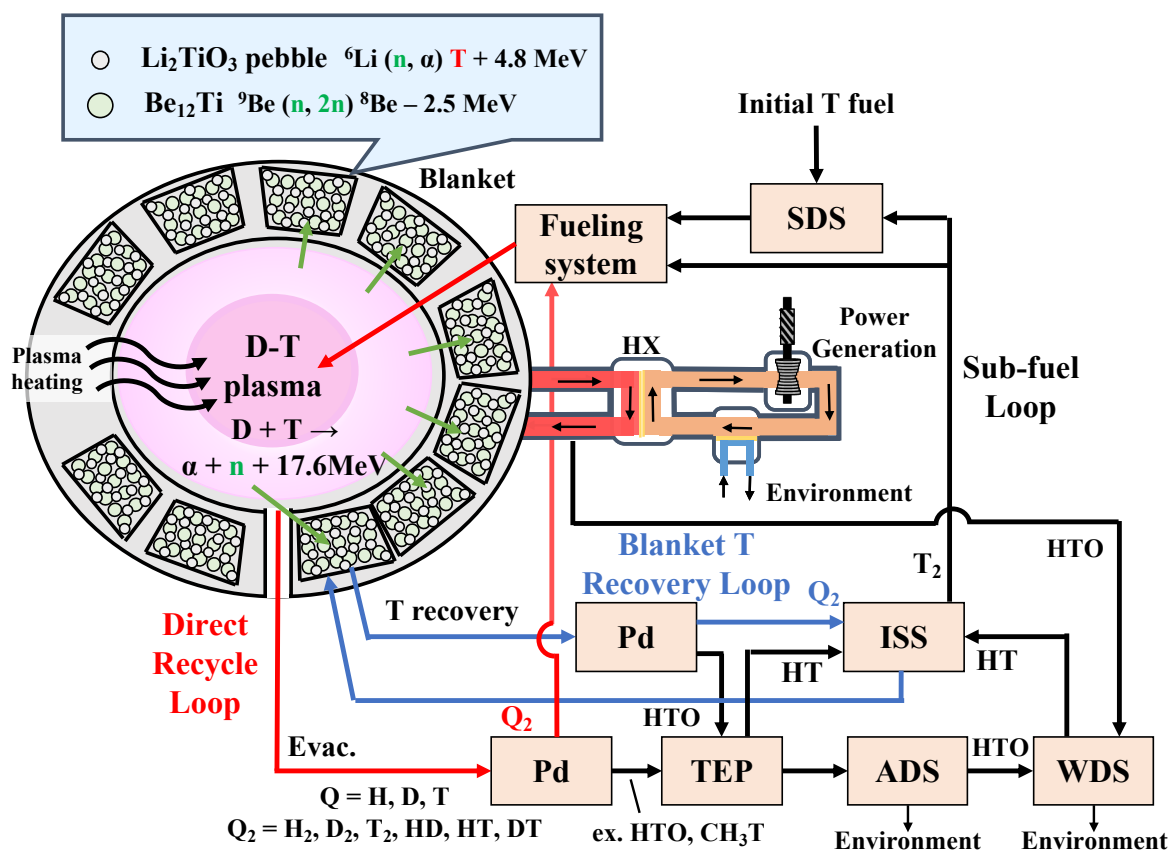There are three types of fueling ways: gas puffing, pellet injection, and neutral beam injection. Given the fusion thermal output and reaction ratio, injecting 10^{22} orders of tritium atoms every second is essential.
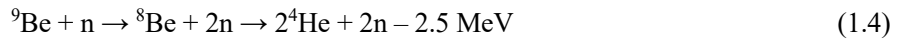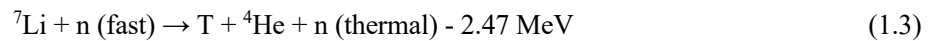
- Tritium Storage and Delivery System (SDS)

ZrCo beds store fuel-grade tritium as a zirconium hydride. Temperature swings control tritium absorption and desorption.

- Vacuum Exhaust System

It comprises roughing vacuum pumps, turbomolecular pumps, and cryopumps. Vacuum vessels and cryostats require a high vacuum environment of at least 10^{-5} and 10^{-3} Pa, respectively. Since the DT nuclear fusion reaction ratio is a few percent, most injected fuel is evacuated quickly. The exhaust gas partially contains gaseous contaminants due to plasma-wall interactions.

- Blanket

It plays a vital role in producing tritium, transferring heat, and shielding neutrons. JA-DEMO adopts a Water-Cooled Ceramic-Breeder (WCCB) blanket approach composed of Li_2TiO_3–based ceramics and beryllium alloys (e.g., $Be_{12}Ti$ or $Be_{12}V$) for self-breeding tritium. Those materials interact with the by-product neutron of the DT fusion reaction. Considering the reactivity to thermal neutrons and reaction heat, equation (1.2) is preferable to equation (1.3). Therefore, ^6Li is enriched from an isotope ratio of 7.6% to 90%. Regarding power generation, high-temperature and high-pressurized primary water coolant loops carry the thermal energy radiated from the plasma and deposited by the following nuclear reactions to the secondary water coolant loop. The heat vaporizes the secondary water coolant, and steam circulates the turbine blades.

$$^6Li + n \rightarrow T \ (2.73 \ \text{MeV}) + {}^4He \ (2.05 \ \text{MeV}) + 4.78 \ \text{MeV} \tag{1.2}$$

$$^7Li + n \ (\text{fast}) \rightarrow T + {}^4He + n \ (\text{thermal}) - 2.47 \ \text{MeV} \tag{1.3}$$

$$^9Be + n \rightarrow {}^8Be + 2n \rightarrow 2{}^4He + 2n - 2.5 \ \text{MeV} \tag{1.4}$$
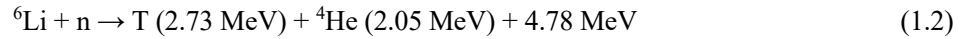
- Pd Diffuser

It quickly separates hydrogen isotopes in molecular form, namely Q_2, from the impurity-containing gas., For instance, it separates H_2, HT, and T_2 gas from the purge gas in the blanket tritium recovery loop. Likewise, it separates D_2, DT, and T_2 gas from the exhaust gas from the vacuum chamber and helps supply them to the reactor promptly in the direct recycle loop.

- Tokamak Exhaust Processing System (TEP)

Tritium-containing gasses (e.g., HTO and CH_3T) from the direct recycling loop and blanket tritium recovery loop are converted to the molecular form of tritium, HT.

- Hydrogen Isotope Separation System (ISS)

It separates hydrogen from Q_2 and purifies deuterium and tritium in a fuel grade. All processes are performed around 20 K to draw on the slight difference in boiling points of H_2, HD, HT, D_2, DT, and T_2.

- Atmosphere Detritiation System (ADS)

Tritium leaked into the air in each tritium confinement barrier is transported to the ADS and converted to the vapor form, HTO. In fact, a trace amount of tritium is expelled into the environment, obeying the domestic regulation value to release into the air. Tritium-free gasses (e.g., He, CO_2, and CO) from the TEP are also expelled.

- Water Detritiation System (WDS)

HTO from the ADS is converted to HT via tritium-containing water. In parallel, some primary water coolant containing tritium is partially bypassed to the WDS. Then, the ISS processes the converted HT.

Since JA-DEMO pursues 1.5 GW fusion thermal output, the tritium fuel cycle must circulate roughly 14 kg day^{-1} of tritium, based on the DT fusion reaction ratio of 1.7% and tritium breeding ratio (TBR) of 1.05 [4]. Once the operation starts, tritium is expected to be widely present throughout the fusion power plant site, either dynamically or statically. Its concentration ranges from nearly 100% to below domestic regulation values for water vapor exhaust into the air, 0.8 Bq mL^{-1}, and for water exhaust to the ocean, 60 Bq mL^{-1}. Furthermore, it exists in various states of matter with different time scales, ranging from as low as 20 K in liquid to as high as 10 keV in plasma. The tritium fuel cycle must fulfill these requirements and specifications to sustain the fusion reaction.

Fortunately, existing industrial techniques and handling experience provide a solid foundation for tritium processing. In heavy water reactors, where heavy water (D_2O) serves as a coolant and a moderator, tritium is predominantly generated via neutron capture reactions, represented by the following equation. Notably, a typical CANDU reactor generates 3 TBq kg^{-1}-D_2O and 74 GBq kg^{-1}-D_2O tritium at most in the moderator and coolant [6]. They are subsequently processed to remove the tritium, which assists the WDS design work.

$$D + n \rightarrow T + \gamma + 6.25 \text{ MeV} \tag{1.5}$$
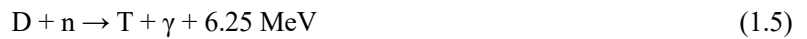
In addition, certain research institutes have acquired experience in tritium handling. Tritium Process Laboratory (TPL) commenced operations in 1988, focusing on developing a tritium confinement and removal system. Overall, TPL effectively handled a combined quantity of 60 g of tritium [7, 8]. During the 1990s, Tokamak Fusion Test Reactor (TFTR) processed 148 TBq per day and 35 PBq per run of tritium within the limitations of a 1.85 PBq site constraint and a 740 TBq machine constraint [9]. Tritium Systems Test Assembly (TSTA) conducted operations utilizing 100 g of tritium in the integrated tritium fuel processing loop [10, 11]. Tritium Laboratory Karlsruhe (TLK), in operation since 1994, possesses a license to manipulate a maximum of 40 g of tritium [12]. TLK has undertaken a variety of investigations so far. Joint European Torus (JET) ran a DT campaign in 1997, utilizing a tritium facility with a capacity of 20 g [13, 14]. JET has

recently increased its capability to accommodate 70 g of tritium [15]. Kyoto Fusioneering Ltd, a Japanese fusion private sector, will shortly demonstrate a tritium fuel cycle [16] in partnership with Canadian Nuclear Laboratories (CNL). International Thermonuclear Experimental Reactor (ITER) will commence DT operation in December 2035. Subsequently, ITER will be required to manage a substantial tritium within the site limitation of 4 kg.

Nevertheless, the current tritium handling techniques must be significantly improved to fulfill the anticipated demands of large-scale DT fusion reactors like JA-DEMO. JA-DEMO requires an initial tritium inventory equivalent to the natural resource and involves a sophisticated tritium fuel cycle encompassing tritium breeding, extraction, separation, purification, and fueling procedures. This highlights an urgent need for research and development in a tritium engineering approach, depending on the constituent elements.

Furthermore, it is crucial to thoroughly evaluate the safety of JA-DEMO as a facility that handles a tremendous amount of tritium. Most DT fusion power plants operate with more tritium than existing nuclear fission power plants. Since the catastrophe in Fukushima in 2011, research and development need to cater to the growing demands for the safety of nuclear facilities. Hence, it is imperative to possess scientific data to convince citizens and construct fusion power plants.

1.2 Technical Issues of the Tritium Fuel Cycle

The tritium fuel cycle comprises many components, as described above, and each has technical challenges to withstand extreme environments. This dissertation specializes in the blanket, water coolant loops, and WDS from tritium-related perspectives. Specifically, it digs into Li mass loss and tritium release behaviors from LTZO ceramic pebbles, newly developed as an advanced tritium breeding material, and tritium permeation behavior between the primary and secondary water coolants. The following subsections carefully itemize technical challenges related to these behaviors.

1.2.1 Lithium Mass Loss Behavior

As mentioned previously, the DT fusion plant operation heavily depends on whether an overall TBR is over 1, namely whether the amount of bred tritium is greater than that of tritium consumption, decay, and loss. Therefore, the National Institutes for Quantum Science and Technology (QST), a leading research institute for fusion R&D in Japan, has invested in techniques for ^{6}Li enrichment [5, 17, 18], a fabrication method known as the emulsion method [19-25], and Li density enhancement [19, 21-25] to realize higher TBR. JA-DEMO has employed Li_2TiO_3 pebbles in its blanket design [1-5] because it has good mechanical robustness, poor chemical reactivity with water vapor, good tritium release properties, etc. Meanwhile, Li_2TiO_3 loses Li quickly because Li is a highly volatile element and reactive with other chemicals. This phenomenon adversely influences tritium breeding performance and tritium production rate.

Furthermore, a tendency has been clarified that the extra Li to boost Li density inversely enhances this behavior [26-28]. Such Li-containing gaseous compounds are corrosive and affect the material soundness and chemical compatibility of reduced activation ferritic-martensitic steel [29, 30]. Although this behavior has been observed to occur inevitably regardless of the type of Li compounds [31-34], the optimum operational scenario for mitigating the Li loss has yet to be fixed, even today. This trade-off needs to be optimized.

1.2.2 Tritium Release Behavior

Despite the wealth of foundational research, uncertainties persist in applying these findings to a DEMO reactor environment, which may differ significantly from lab-scale experimental conditions. One example is the long-term usage in an environment as high as 1173 K. While many post-irradiation experiments (PIE) on tritium release behavior from many kinds of as-received tritium breeding materials have been conducted [35-37], few studies attempt to elucidate the effect of the long-term heating environment on the tritium release behavior. JA-DEMO is expected to utilize the solid blanket module continuously for two years. This long period of operations may lead to structural changes in Li_2TiO_3 pebbles, resulting in neighboring grains combining and then affecting the tritium migration path inside the grain and the pores. If these changes degrade tritium release properties, the tritium inventory in the material will surge. This is an enormous threat from operation, maintenance, radiation protection, and safety perspectives.

In addition, it should be noted that the released bred tritium chemical formula strongly dictates workload requirements for downstream processing units. For instance, as shown in Figure 1.1, HT release is preferred over HTO to reduce the workload of the TEP [4], which converts HTO and CH_3T to HT. Since the exhaust gas is expected to primarily consist of the D_2 and T_2 gas, the chemical form of the released tritium in the blanket (i.e., HTO or HT) is critical to designing TEP specification. Furthermore, T_2 release is much more desirable than HT to reduce the workload of the ISS [4], which removes hydrogen and enriches deuterium and tritium to a fuel grade. Based on the current design [38, 39], H-containing He purge gas is introduced to enhance the tritium recovery. In fact, this method is incompatible with ISS and merely increases its burden because hydrogen is a troublesome impurity that obstructs the DT fusion reaction and requires tremendous energy for removal to make the most of tiny differences from tritium. Besides, this causes the reduction of the TiO_2 of Li_2TiO_3 pebbles, possibly leading to unexpected degradation of the tritium release behavior. Alternative tritium extraction without hydrogen should be contemplated.

1.2.3 Tritium Permeation Behavior

The permeation between the gas phase through a metal has been carefully done so far [40, 41]. It applies to the permeation of the released tritium from the tritium breeder into the water coolant by the blanket. However, unfortunately, it is still challenging to describe tritium permeation behavior from water to water through a metal. This is because a physics model for water-to-water tritium permeation, namely its dependences on concentration, pressure, temperature, and so on, has yet to be fully clarified. Nevertheless, based on the recent JA-DEMO design [1-4], high-temperature and high-pressurized water coolant loops are selected as a heat medium to remove the heat and generate power.

This ultimately leads to an inevitable tritium leakage into aquatic environments as existing nuclear facilities globally discharge vast amounts of tritium. In the case of JA-DEMO, impinged tritium from the edge plasma [41, 42] and bred tritium in the blanket [41] can permeate through metals and piping, eventually reaching the primary water coolants. Then, it is brought to the environment with heat transport through the heat exchanger [43], the secondary water coolant, and the condenser. From the point of view of public safety, the tritium concentration in the cooling water system should be carefully investigated.

Additionally, the tritium inventory in the primary and the secondary cooling water needs to be evaluated as a source term in the event of a piping rupture accident. Hence, the WDS is necessary to suppress tritium concentration in the primary coolant loop to mitigate the potential risk of tritium. Also, credible assessments can help devise countermeasures against tritium release during the maintenance period of the power generation unit. Therefore, tritium permeation significantly impacts the feasibility of fusion power plants from the viewpoints of tritium control, safety, and public acceptance of the following commercial fusion plants.

1.3 Research Objectives

The primary goal of this work is to bridge the existing research gaps and contribute to the design work of JA-DEMO. Hence, this work conducted an in-depth study, including analyses, experiments, and simulations to accomplish the following objectives:

- Characterization of LTZO (Chapter 3)

The purpose is to characterize the LTZO ceramic pebbles from a fusion engineering perspective to make a database for future work and to perform further investigations and fruitful discussion in the following chapters.

- Li Mass Loss Behavior (Chapter 4)

The first objective is to experimentally elucidate Li evaporation rates from the LTZO pebbles. Another goal is to examine the structural changes due to the long-term heating. The last goal is to evaluate the negative impact of the Li mass loss on the tritium breeding performance through 1D simulation using the experimentally obtained Li evaporation rate.

- Tritium Release Behavior (Chapter 5)

The first aspiration is to experimentally clarify how transmuted tritium releases from LTZO under different purge gas species and assess its tritium release performance based on tritium mass balance. Subsequently, this work aims to inspect the influence of structure change on tritium release behavior, exploring HT/T_2 release experimental conditions.

- Tritium Permeation Behavior (Chapter 6)

First, this work aims to establish a water-to-water tritium permeation model, integrating the existing experimental data. Then, this work attempts to simulate the transition of tritium concentration in the primary and secondary water coolants. Lastly, this work tries to appraise the required specifications for the WDS based on global standards.

1.4 Structure of Dissertation

This Ph.D. dissertation encompasses three areas of research: Li mass loss behavior, tritium release behavior, and tritium permeation behavior. Chapter 1 functions as an introductory section, providing a concise overview of the imperatives and technical complexities related to the tritium fuel cycle. Subsequently, it delves into individual study topics, addressing their respective technical concerns and outlining their objectives. Chapter 2 provides an overview of the essential principles of fusion tritium engineering, intending to improve comprehension of the subsequent chapters. Chapters 3, 4, 5, and 6 provide an in-depth analysis of the experimental data and simulation outcomes. Chapter 3 provides a comprehensive analysis of the LTZO. It focuses on key aspects to shed light on its Li mass loss behavior, further explored in Chapter 4, and its tritium release behavior, elaborated in Chapter 5. Chapter 6 comprehensively discusses the tritium permeation behavior between the high-temperature and high-pressurized water. Chapter 7 concludes the dissertation. Chapter 8 provides the future outlook regarding each study. Finally, Appendices A and B serve as complementary additions to the discourse presented in Chapter 5.

References

[1] K. Tobita et al., Fusion Sci. Technol., 75, (2019), 372–383, doi: 10.1080/15361055.2019.1600931.

[2] Y. Someya et al., Fusion Eng. Des., 146, (2019), 894-897, doi: 10.1016/j.fusengdes.2019.01.107.

[3] Y. Kawamura et al., Fusion Eng. Des., 161, (2020), 112050, doi: 10.1016/j.fusengdes.2020.112050.

[4] Y. Iwai et al., Fusion Eng. Des., 166, (2021), 112261, doi: 10.1016/j.fusengdes.2021.112261.

[5] Y. Ishi et al., Fusion Sci. Technol., 77, (2021), 532–548, doi: 10.1080/15361055.2021.1925030.

[6] K. M. Song et al., Fusion Sci. Technol., 48, (2005), 290-293, doi: 10.13182/FST05-A929.

[7] T. Yamanishi et al., Fusion Eng. Des., 83, (2008), 1359-1363, doi: 10.1016/j.fusengdes.2008.08.010.

[8] R. Kurata et al., Fusion Sci. Technol., 71, (2017), 687-692, doi: 10.1080/15361055.2017.1290953.

[9] A. von Halle, "Final operations of the Tokamak Fusion Test Reactor (TFTR)," 17th Symposium on Fusion Engineering (SOFE), San Diego, USA, 1997.

[10] J. L. Anderson et al., Fusion Eng. Des., 28, (1995), 183-189, doi: 10.1016/0920-3796(95)90038-1.

[11] S. Konishi et al., Fusion Eng. Des., 28, (1995), 258-264, doi: 10.1016/0920-3796(95)90046-2.

[12] L. Dörr et al., Fusion Sci. Technol., 48, (2005), 262-267, doi: 10.13182/FST05-A924.

[13] R. Lässer et al., Fusion Eng. Des., 46, (1999), 307-312, doi: 10.1016/S0920-3796(99)00023-X.

[14] R. Lässer et al., Fusion Eng. Des., 47, (1999), 173–203, doi: 10.1016/S0920-3796(99)00082-4.

[15] J. Mailloux et al., Nuclear Fusion, 62, (2022), 042026, doi: https://doi.org/10.1088/1741-4326/ac47b4.

[16] C. Baus et al., J. Fusion Energy, 42, (2023), 10, doi: 10.1007/s10894-023-00346-y.

[17] T. Hoshino, Desalination, 359, (2015), 59-63, doi: 10.1016/j.desal.2014.12.018.

[18] K. Morita et al., Solid State Ionics, 355, (2020), 115434, doi:10.1016/j.ssi.2020.115434.

[19] T. Hoshino et al., Fusion Eng. Des., 87, (2012), 486-492, doi: 10.1016/j.fusengdes.2012.01.005.

[20] T. Hoshino, Fusion Eng. Des., 89, (2014), 1431-1435, doi: 10.1016/j.fusengdes.2013.12.052.

[21] T. Hoshino, Fusion Eng. Des., 98-99, (2015), 1788-1791, doi: 10.1016/j.fusengdes.2015.04.023.

[22] T. Hoshino, Fusion Eng. Des., 109-111, (2016), 1114-1118, doi: 10.1016/j.fusengdes.2016.01.012.

[23] T. Hoshino, Nucl. Mater. Energy, 9, (2016), 221-226, doi: 10.1016/j.nme.2016.05.004.

[24] Y. Kawamura et al., Fusion Eng. Des., 136, (2018), 1550-1556, doi: 10.1016/j.fusengdes.2018.05.055.

[25] T. Hoshino et al., J. Plasma Fusion Res., 93-02, (2017), 83-90, in Japanese.

[26] K. Katayama et al., Fusion Eng. Des., 136, (2018), 362-366, doi: 10.1016/j.fusengdes.2018.02.032.

[27] K. Mukai et al., J. Phys. Chem., 124, (2020), 10870-10877, doi: 10.1021/acs.jpcc.0c02454.

[28]A. Ipponsugi et al., Nucl. Mater. Energy, 25, (2020), 100777, doi: 10.1016/j.nme.2020.100777.

[29]E. Gaisina et al., J. Nucl. Mater., 564, (2022), 153677, doi: 10.1016/j.jnucmat.2022.153677.

[30]C. Wagn et al., Ceram. Int. 49, (2023), 17851-17858, doi: 10.1016/j.ceramint.2023.02.151.

[31]G. Weber et al., J. Therm. Anal. Calorim., 132, (2018), 1055-1064, doi: 10.1007/s10973-017-6943-7.

[32]S. Gu et al., Nucl. Fusion, 63, (2023), 046006, doi: 10.1088/1741-4326/acb220.

[33]R. Chen et al., Appl. Cera. Technol., 20, (2023), 2576-2585, doi: 10.1111/ijac.14392.

[34]S. Kikuchi et al., Fusion Eng. Des., 193, (2023), 113793, doi: 10.1016/j.fusengdes.2023.113793.

[35]T. Kinjyo et al., Fusion Eng. Des., 83, (2008), 580-587, doi: 10.1016/j.fusengdes.2007.11.011.

[36]Q. Qi et al., Nucl. Mater. Energy, 28, (2021), 101036, doi: 10.1016/j.nme.2021.101036.

[37]M. H. H. Kolb et al., J. Nucl. Mater., 489, (2017), 229-235, doi: 10.1016/j.jnucmat.2017.03.051.

[38]Y. Kawamura et al., Fusion Eng. Des., 136, (2018), 1550-1556, doi: 10.1016/j.fusengdes.2018.05.055.

[39]R. Hiwatari et al., Fusion Eng. Des., 143, (2019), 259-266, doi: 10.1016/j.fusengdes.2019.03.174.

[40]T. Shiraishi et al., J. Nucl. Mater., 254, (1998), 205-214, doi: 10.1016/S0022-3115(97)00362-0.

[41]K. Katayama et al, Fusion Sci. Technol., 71, (2017), 261-267, doi: 10.1080/15361055.2017.1288423.

[42]K. Katayama et al., Fusion Eng. Des., 169, (2021), 112576, doi: 10.1016/j.fusengdes.2021.112576.

[43]K. Katayama et al., J. Nucl. Mater., 565, (2022), 153723, doi: 10.1016/j.jnucmat.2022.153723.

Chapter 2. Fundamentals in Fusion Tritium Engineering

Outline

This chapter introduces the fundamental principles of tritium physics, establishing a solid basis for comprehending the subsequent chapters. The first seven sections are necessary for the tritium breeding material and are dedicated to Chapters 3, 4, and 5. Sections 2.4, 2.6, 2.8, 2.9, and 2.10 are crucial for the tritium permeation behavior and are dedicated to Chapter 6.

2.1 Surface Water

Water vapor in the gas phase is adsorbed and desorbed onto the grain surface of the Li ceramic pebbles. It is categorized into two types of water vapor adsorption: physisorption and chemisorption. This dissertation defines physisorption as the water vapor adsorbed by the van der Waals force. It depends on the partial pressure of water vapor in the gas phase. Therefore, it is effortless to remove it by purging the pebbles even at room temperature. Chemisorption is defined as the water vapor adsorbed by chemical bonds. It depends only on the temperature. Therefore, it is necessary to heat the pebbles to energize the vapor molecules for desorption. It is imperative to note that this definition differs from the conventional surface science definitions based on the adsorption energy.

2.2 BET-Specific Surface Area

Specific surface area is the overall surface area of a substance divided by its mass or volume. This property is crucial for materials whose performance is highly surface-dependent, such as catalysts, adsorbents, and battery materials. Brunauer-Emmett-Teller (BET) surface area analysis [1] is a method to measure the specific surface area of materials, providing valuable information about a material's porosity and surface characteristics, even though it depends on the International Union of Pure and Applied Chemistry (IUPAC) type classification. The BET method involves adsorbing a layer of gas molecules onto the material's surface and measuring the amount of gas adsorbed at various pressures. The BET theory postulates that the gas molecules form a monolayer on the surface. Once the first layer is formed, subsequent adsorption layers can form on top of it. This method can apply to the range of 0.05 to 0.35 of the relative pressure of the isotherm. The following BET equation calculates the gas required to form a monolayer. This quantity is then used to compute the BET-specific surface area by considering the known cross-sectional area of the adsorbed gas.

$$\frac{P}{V(P_0 - P)} = \frac{C-1}{V_m C}\frac{P}{P_0} + \frac{1}{V_m C}, \tag{2.1}$$

$$A_{tot} = N_A\,\sigma\,V_m\,/\,22414, \tag{2.2}$$

$$A_{spe} = A_{tot}\,/\,M, \tag{2.3}$$

where P and P_0 [Pa] are the equilibrium pressure and saturation pressure of adsorbate at the specific temperature, V and V_m [m^3(STP) g^{-1}] are the adsorption amount and monolayer adsorption capacity at the specific pressure and temperature, C [-] is the BET constant, A_{tot} [m^2] is the total surface area of the adsorbent, N_A [mol^{-1}] is Avogadro's number, σ [m^2] is the effective cross-sectional area of adsorbate, 22414 [m^3] is the molar volume of the ideal gas, A_{spe} [m^2 g^{-1}] is the specific surface area of the adsorbent, and M [g] is the mass of the adsorbent.

The following equation obtains the theoretical specific surface area based on the assumption that the grains are spherical.

$$A_{th} = \frac{4\pi \left(\frac{d}{2}\right)^2}{\rho_{th} \frac{4\pi}{3}\left(\frac{d}{2}\right)^3} = 6 / \rho_{th}\, d, \tag{2.4}$$

where A_{th} [m^2 g^{-1}] is the theoretical specific surface area, ρ_{th} [g m^{-3}] is the theoretical density, and d [m] is the average grain diameter. The difference between the specific surface area and the theoretical specific area means the specific surface area of the closed pores, which the adsorbent gas molecule could not reach.

2.3 Li Mass Loss

Tritium breeding materials are supposed to be placed in a high-temperature environment. During the operation, they are exposed to radiation heat from the plasma and nuclear reaction heat generated by equations (1.2), (1.3), and (1.4). Therefore, as mentioned in section 1.2.1, it is inevitable for Li_2TiO_3 pebbles to lose some Li due to evaporation. This results from Li, Li_2O, or LiOH. LiOH is formed by chemical interaction with water vapor in the gas.

$$Li_{(s)} \rightarrow Li \uparrow \tag{2.5}$$

$$Li_2O_{(s)} \rightarrow Li_2O \uparrow \tag{2.6}$$

$$Li_{(s)} + H_2O \rightarrow 2LiOH_{(s)} \rightarrow 2LiOH \uparrow \tag{2.7}$$

Previous work [2] highlighted that vapor containing gas more than 0.1 ppm, equivalent to 0.01 Pa, promoted the chemical interaction with the water vapor in the gas stream, as in equation (2.7). Whatever blanket design fusion plants employ, it is exceptionally challenging to reduce the water vapor concentration in the gas to less than 0.1 ppm as long as sweep gas contacts to the breeding material to extract the bred tritium or to remove the heat. Considering the capabilities of commonly used adsorbents, more or less 10 ppm of water vapor must be present in the sweep gas. In short, equation (2.7) is more critical than equations (2.5) and (2.6) in terms of Li desorption in the breeding zone.

Hence, this work primarily focused on the Li mass loss due to equation (2.7). The following elementary processes are designed to grasp the Li mass loss dynamics. The rate-determining elementary process is likely the LiOH evaporation rather than the LiOH formation.

1. LiOH formation reaction on the surface of the grain, as in equation (2.7).

2. LiOH evaporation from the grain surface.

3. LiOH mass transfer to the geometrical surface of the pebble through the pores.

4. LiOH mass transfer to the purging gas flow through the fluid film.

Moreover, the Li mass loss behavior is modeled to be driven by the disparity in the chemical potential. It spontaneously proceeds according to the partial pressure of the water vapor in the gas and temperature. Therefore, in the case of the LTZO, it should exponentially lose energetically unstable Li_2O, locating the interstitial sites.

$$dY / dt = - k (Y - Y_s), \tag{2.8}$$

$$Y = Y_s + (1 - Y_s)\, e^{-kt}, \tag{2.9}$$

$$k = AP_{H2O}^{1/2} \exp(- E / RT), \tag{2.10}$$

where Y and Y_s [-] are the weight of the pebble and the stable component normalized by its original weight before heating, t [s] is the time, k [s^{-1}] is the mass transfer coefficient, A [Pa$^{-1/2}$ s^{-1}] is the pre-exponential factor, P_{H2O} [Pa] is the water vapor partial pressure, E [J mol^{-1}] is the activation energy required to evaporate, R [J mol^{-1} K^{-1}] is the gas constant, and T [K] is the temperature.

2.4 Tritium

Tritium is a radioactive isotope of hydrogen, distinct from other stable isotopes: hydrogen and deuterium. As seen in Figure 2.1, tritium has additional neutrons, which make it radioactive and less stable. The number of unpaired electrons determines the chemical characteristics of substances. The hydrogen isotopes have only one electron, so they chemically behave the same. By contrast, their mass significantly differs, so they do not physically behave the same.
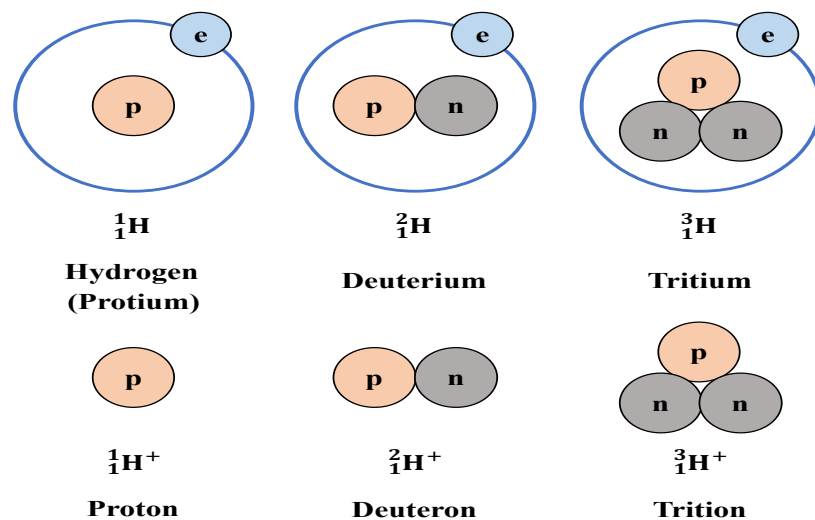

Figure 2.1. Schematic of the hydrogen isotopes.

In general, the radioactivity, A [Bq], is proportional to the number of atoms present at the specific moment, N [-]. Mathematically, A and N are expressed as follows:

$$A = dN / dt = - \lambda N, \tag{2.11}$$

$$N = N_0 \, e^{-\lambda t}, \tag{2.12}$$

$$\lambda = \ln 2 / T_{1/2}, \tag{2.13}$$

where λ [s^{-1}] is the decay constant, and $T_{1/2}$ [s] is the half-life required to halve the number of atoms. In the case of tritium, the decay constant is 1.78×10^{-9} s^{-1}, and the half-life is 12.3 years. During the decay, tritium emits a low-energy beta particle, β^-, and transmutes into ^{3}He.

$$T \rightarrow {}^3He + \beta^- + \bar{\nu}_e + 18.6 \text{ keV}. \tag{2.14}$$

The beta particle's kinetic energy varies within 18.6 keV, with an average of 5.7 keV. The low-energy beta particles cannot penetrate the human skin, so their external exposure risk is negligible. On the other hand, if tritium is ingested, inhaled, or absorbed into the human body, it poses considerable hazards. Its energy is large enough to damage DNA, which brings vast toxicity and a threat to our lives. It takes 10 days to halve the tritium intake naturally. If it organically binds to proteins, fats, carbohydrates, etc., the duration extends to 40 days. Therefore, understanding tritium behavior is extremely important for fusion applications that handle large amounts of tritium.

Its limited natural abundance originates from its short half-life. The annual amount of tritium generated from natural sources is 70×10^{15} Bq. Meanwhile, the frequent nuclear weapon tests in the 1950s and 1960s drastically surged the tritium abundance to approximately 200×10^{18} Bq. It has been decreasing gradually, but the existing nuclear facilities worldwide release massive amounts of tritium into the environment at a rate as large as the natural yielding rate. For example, the La Hague nuclear fuel reprocessing plant in France annually releases about 10×10^{15} Bq. After all, tritium exists roughly 1×10^{18} Bq today, corresponding to 1 kmol and 3 kg. Based on equation (2.11), Avogadro's number, and tritium's atomic and molecular mass, Table 2.1 summarizes the relationship between the amount of substance, radioactivity, and weight.

Table 2.1. Unit conversion coefficients for tritium atom, T, and tritium molecule, T_2.

For T atom		For T_2 molecule	
Bq mol^{-1}	1.07×10^{15}	Bq mol^{-1}	2.15×10^{15}
mol Bq^{-1}	9.31×10^{-16}	mol Bq^{-1}	4.66×10^{-16}
Bq g^{-1}	3.56×10^{14}	Bq g^{-1}	7.12×10^{14}

2.5 Nuclear Reaction

Nuclear reactions usually occur by bombarding a target nucleus with particles, such as protons, neutrons, photons, heavy ions, etc. Nuclear reactions are incredibly diverse because there are many types of target and incident particles. Also, their behavior dramatically differs depending on the collision energy. As exemplified in equation (2.15), the reaction in which an incident particle, a, strikes a target, A, and then the target transmutes into another element, B, emitting another particle, b, is expressed as A(a, b)B. For example, the nuclear reactions that occurred in the tritium breeding zone, as in equations (1.2) and (1.4), are described in ^{6}Li(n, α)T and ^{9}Be(n, 2n)2^{4}He. Both ^{6}Li and ^{9}Be initially capture neutrons and then split into multiple particles.

$$a + A \rightarrow b + B. \tag{2.15}$$

The following equation theoretically determines its radioactivity on the condition that the generated nucleus is radioactive.

$$A_B = \sigma_A \, N_A \, \phi \, (1 - e^{-\lambda t}), \tag{2.16}$$

where A_B [Bq] is the generated radioactivity, σ_A [m^{-2}] is the cross-section of the target atom A, N_A [-] is the number of the target atom A, ϕ [cm^{-2} s^{-1}] is the incident particle flux, and t [s] is the exposure time to the incident particles. Once the radioactive elements are created, they immediately start to decay. Therefore, equation (2.16) has the term to represent the decay. While exposed to the incident particles, the number of produced atom B is balanced based on equations (2.11) and (2.12).

$$dN_B / dt = \sigma_A \, N_A \, \phi - \lambda N_B = \sigma_A \, N_A \, \phi \, e^{-\lambda t}. \tag{2.17}$$

This means that the production rate, $\sigma_A \, N_A \, \phi$, is constant, and the decay rate, λN_B, changes over time. Immediately after the irradiation ceases, the number of atom B decreases exponentially over time based on equation (2.12).

Many hot atoms, which have a higher energy level than their ground state, are generated during irradiation. This heightened energy, which can manifest as increased kinetic energy or excited electronic states, is a typical result of nuclear reactions. Due to their excess energy, hot atoms are generally more reactive than those in thermal equilibrium. The energy surplus leads them to participate in chemical reactions that would not usually occur. While the binding energy of ordinary compounds is about a few eV, the recoil energy, especially in light atoms, is enormous enough to break the surrounding potential energy.

2.6 Diffusion

When tritium has a non-uniform distribution in a solid substance, tritium flows in a direction that reduces the non-uniformity. This diffusion phenomenon is known as Fick's First Law and is expressed as follows:

$$J = - D \, \nabla C, \tag{2.18}$$

where J [mol m^{-2} s^{-1}] is the tritium diffusion flux, D [m^2 s^{-1}] is the tritium diffusion coefficient in the substance, and C [mol m^{-3}] is the tritium concentration in the substance.

Plus, there is a relationship between J and $C,$ considering the balance of the solute particles in a finite volume element, as in equation (2.19). From these two equations, equation (2.20) is obtained on the condition that the dependence of diffusion coefficient on solute concentration can be ignored and known as Fick's Second Law.

$$\partial C / \partial t = \nabla J. \tag{2.19}$$

$$\partial C / \partial t = - D \, \nabla^2 C. \tag{2.20}$$

On a microscopic scale, diffusion refers to the transition of a tritium particle from one system to another due to a random walk, driven by the concentration gradient along the diffusion direction represented in equation (2.20). Countless defects are thermally equilibrium in the substance, like vacancy, dislocation, interstitial, and impurity atoms. Tritium atoms diffuse from one stable position to another adjacent stable position in the lattice of the substance. During this migration, the crystal lattice experiences local strains as the lattice atoms are pushed aside. Therefore, this transition requires significant energy to overcome the repulsion from the displaced lattice atoms, which is derived from the thermal vibrations of the atoms. The vibrational energy and the activation energy barrier affect this jumping movement frequency. These factors determine the diffusion coefficient, D, which is described more specifically based on the Arrhenius equation.

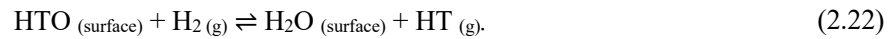$$D = D_0 \exp(- E_\mathrm{d} / RT), \tag{2.21}$$

where D_0 [m^{-2} s^{-1}] is the pre-exponential factor, E_d [J mol^{-1}] is the activation energy for diffusion, R [J mol^{-1} K^{-1}] is the gas constant, and T [K] is temperature.

It is known that non-metallic light elements in a metallic substance like tritium have considerably smaller ionic radius than metallic elements. The lattice that metallic elements constitute is spacious for tritons. This allows tritons to move around the spaces in the lattice with less displacement, occupying interstitial positions such as octahedral and tetrahedral sites. As a result, tritium can diffuse inside swiftly.

2.7 Tritium Release

The tritium release process consists of many mass transfer processes, as listed below. The rate-determining elementary process depends on the gain size. The tritium diffusion process in the ceramic is relatively fast. As the pebble consists of finer grains, its surface area increases, leading to a more outstanding surface effect than the bulk. In short, the surface reaction, as in the elementary process 4, determines the overall mass transfer rate when the ceramic pebble comprises small grains. Figure 2.2 illustrates the tritium migration pathway.

1. ^{6}Li(n, α)T and ^{7}Li(n, n α)T reactions in a crystal grain, as in equations (1.2) and (1.3).

2. Thermalization of the hot tritium by elastic and inelastic collisions, introducing irradiation defects.

3. Tritium diffusion to the grain surface through grain boundaries, interacting with the irradiation defects generated in the crystal grain.

4. Surface reaction on the grain surface with purge gas species.

4.1 Adsorption and desorption of HTO and H_2O.

4.2 Isotope exchange reactions between HTO surface water and H_2 and H_2O in the gas phase.

$$\text{HTO }_{(surface)} + \text{H}_{2\ (g)} \rightleftharpoons \text{H}_2\text{O }_{(surface)} + \text{HT }_{(g)}. \tag{2.22}$$

$$\text{HTO }_{(surface)} + \text{H}_2\text{O }_{(g)} \rightleftharpoons \text{H}_2\text{O }_{(surface)} + \text{HTO }_{(g)}. \tag{2.23}$$

4.3 Water formation reaction between oxides and H_2 in the gas phase.

$$\text{H}_2 + \text{MO}_x \rightarrow \text{H}_2\text{O} + \text{MO}_{x-1}. \tag{2.24}$$

5. Mass transfer of HT and HTO through the interconnected pores to geometrical surfaces of the pebbles.

6. Mass transfer of HT and HTO through fluid film formed between geometrical surfaces of the pebbles and the purge gas flow.
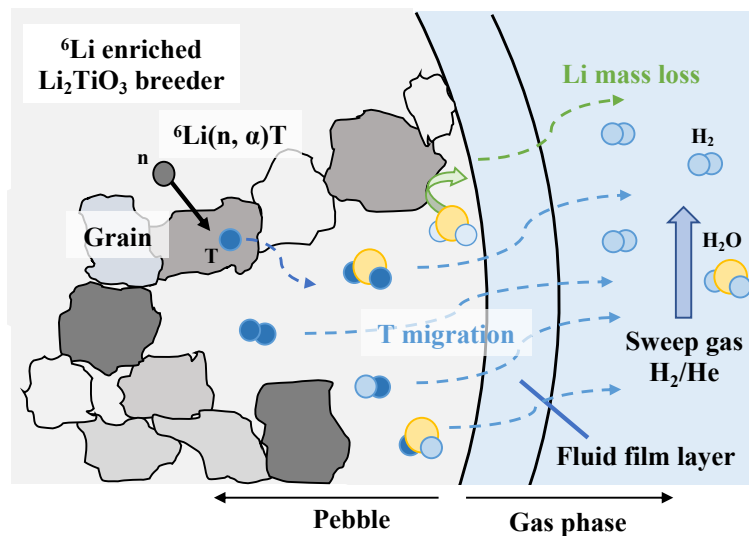

Figure 2.2. Schematic of the migration pathway of the produced tritium and evaporated Li.

2.8 Surface Interaction

The potential barrier for tritium molecules is critical for dissolving into a substance. It can interact with solid surfaces in two ways, either weak or strong bonding, depending on the electronic structure of the solid [3]. First, tritium molecules can form weak van der Waals bonds on the surface. Then, it advances to the following element process, comparing the activation energy to dissociate into two tritium atoms with the potential energy when dissolved into the substance. Based on Henry's law, if the activation energy is higher, it dissolves into the substance in a molecule form.

$$C = HP, \tag{2.25}$$

where C [mol m^{-3}] is the solute tritium concentration, H [mol m^{-3} Pa^{-1}] is Henry's constant, and P [Pa] is the partial pressure of tritium molecules. It is known that molten salts such as FLiBe conform to Henry's law.

Conversely, if the activation energy is lower, it dissociates into two atoms. Equation (2.26) expresses its rate. Then, it dissolves into the substance in an atomic form based on Sieverts' law.

$$\phi_{\text{dissoc}} = K_d P, \tag{2.26}$$

$$C = SP^{1/2}, \tag{2.27}$$

where ϕ_{dissoc} [mol m^{-2} s^{-1}] is the tritium dissociation flux, K_d [mol m^{-2} s^{-1} Pa^{-1}] is the dissociation constant, and S [mol m^{-3} Pa$^{-1/2}$] is Sieverts' constant. It is known that metals that have an affinity with tritium, such as Ni, Pd, Li, and LiPb, conform to Sieverts' law. The potential energy in the case of Sieverts' law is depicted in Figure 2.3. Henry's and Sieverts' constants can also be described using the Arrhenius equation with the pre-exponential factors, H_0 [mol m^{-3} Pa^{-1}] and S_0 [mol m^{-3} Pa$^{-1/2}$], and the activation energy, E_{sH} and E_{sS} [J mol^{-1}].

$$H = H_0 \exp(-E_{\text{sH}} / RT), \tag{2.28}$$

$$S = S_0 \exp(-E_{\text{sS}} / RT), \tag{2.29}$$

In parallel, association and desorption also occur on the surface, corresponding to the dissociation and adsorption processes. Those surface dynamics reach a state of equilibrium. Beyond surface interaction, there's also the potential to culminate in hydrides based on the system's pressure-composition-temperature curve.
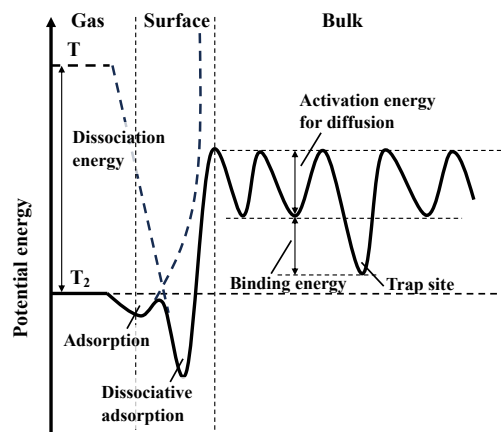

Figure 2.3. An example schematic of the potential energy regarding the solution and diffusion process.

2.9 Permeation

Permeation is the process in which surface kinetics and diffusion combine in a series. Therefore, each rate strongly affects the permeation rate. Only cases of permeation accompanied by dissociative adsorption are discussed here. Tritium dissolved into the solid surface can make a tritium concentration distribution. Subsequently, it diffuses according to the concentration gradient based on Fick's First Law. This diffusion flux can be described as follows:

$$J_T = - D \, (C_2 - C_1) / d, \tag{2.30}$$

where C_1 and C_2 [m^{-3}] are the solute tritium concentration on both ends, and d [m] is the thickness of the solid substance. As delineated above, equation (2.30) can be rewritten in the following equation.

$$J_T = - DS \, (P_2^{1/2} - P_1^{1/2}) / d = K \, (P_1^{1/2} - P_2^{1/2}) / d, \tag{2.31}$$

$$K = K_0 \exp(- E_K / RT), \tag{2.32}$$

where the tritium partial pressure on the representative sides is denoted as P_1 and P_2 [Pa]. The permeation coefficient and the pre-exponential factor are represented by K and K_0 [mol m^{-1} s^{-1} Pa$^{-1/2}$]. The activation energy to permeate is denoted as E_k [J K^{-1}].

In the case of diffusion-limited permeation, the diffusion rate determines the overall mass transfer rate. As equation (2.31) says, its permeation rate is proportional to the square root of the partial pressure of tritium molecules. This permeation model can apply to most cases.

In contrast, it has been experimentally observed that permeation depends on the first power of the hydrogen isotope gas pressure [4]. This transition boundary is on the order of 10^2 Pa, which slows down the dissociation process expressed in equation (2.26) and determines the overall mass transfer rate. The tritium concentration in the gas flow is uniform thanks to the diffusion and advection under the flow. However, as the pressure drops, diffusing within the thin film between the surface and the gas becomes time-consuming. The mass flow rate of the supply gas significantly affects the thickness of the boundary film, which is crucial to estimating the permeation behavior with higher credibility.

To wrap up, the rate-controlling step of the permeation process differs depending on the combination of materials and operation conditions. The surface interaction or diffusion process limits the overall mass transfer rate because the permeation process is continuous. Figure 2.4 exemplifies the tritium concentration in the permeation system according to either the surface- or diffusion-limited case.
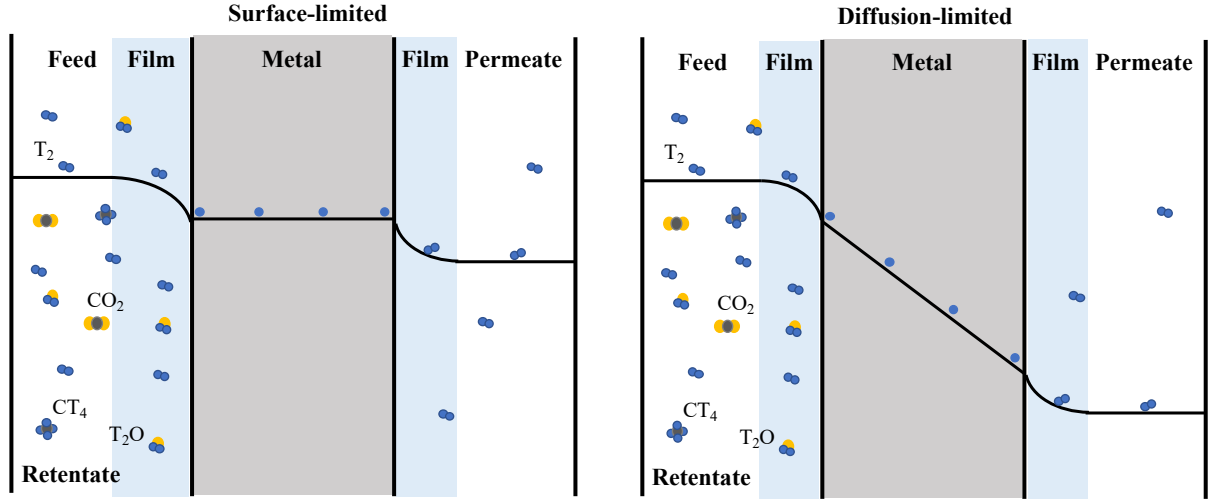
Figure 2.4. An example schematic diagram of the tritium permeation behavior.

In parallel with the tritium permeation, hydrogen and deuterium also permeate. There are limited sites and paths to dissolve into the surface and diffuse inside. When there are multiple species of hydrogen isotopes in a system, it can be helped to share them with all the hydrogen isotopes according to their existence ratio, and they co-permeate through a substance. This is known as Hickman's law [5] and experimentally observed [6]. Thus, equation (2.31) is rewritten as follows:

$$J_T = y_T K \left(P_{tot1}^{1/2} - P_{tot2}^{1/2} \right) / d, \qquad (2.33)$$

where y_T [-] is the molar fraction of tritium molecules to other hydrogen isotopes, and P_{tot1} and P_{tot2} [Pa] are the total pressure of hydrogen isotope species on both ends. This contributes to reducing the tritium permeation loss in a way.

On the other hand, it has also been experimentally observed that hydrogen isotopes behave independently [7]. In this case, equation (2.31) is applicable directly.

2.10 Isotope Effects

While the monoatomic gas molecules have degrees of freedom only in translation, the diatomic and polyatomic gas molecules have degrees of freedom in translation, vibration, and rotation. The average velocity of these gas molecules, v [m^2 s^{-1}], follows the Maxwell-Boltzmann distribution.

$$v = (8k_\mathrm{b}T / \pi m)^{1/2}, \tag{2.34}$$

where k_b [J K^{-1}] is the Boltzmann constant, and m [kg] is the mass of the gas molecule. As illustrated in Figure 2.1, hydrogen isotopes possess a distinct mass difference. Thus, properties regarding their velocity also have outstanding differences. For instance, the incident flux is proportional to the velocity, so its difference between hydrogen isotopes is also expressed with the square root of the mass ratio. Then, the incident particles to the surface initiate the permeation process. Therefore, parameters such as diffusion coefficient, Sieverts' constant, and permeation coefficient manifest disparate values among different isotopes and are described below.

$$D_\mathrm{H} / D_\mathrm{T} = \sqrt{3}. \tag{2.35}$$

$$S_\mathrm{H} / S_\mathrm{T} = \sqrt{3}. \tag{2.36}$$

$$K_\mathrm{H} / K_\mathrm{T} = D_\mathrm{H} S_\mathrm{H} / D_\mathrm{T} S_\mathrm{T} = 3. \tag{2.37}$$

$$K_\mathrm{D} / K_\mathrm{T} = D_\mathrm{D} S_\mathrm{D} / D_\mathrm{T} S_\mathrm{T} = 3/2. \tag{2.38}$$

References

[1] S. Brunauer et al., J. Am. Chem. Soc., 60, (1938), 309-319, doi: 10.1021/ja01269a023.

[2] K. Mukai et al., J. Phys. Chem., 124, (2020), 10870-10877, doi: 10.1021/acs.jpcc.0c02454.

[3] K. Christmann, Surf. Sci. Rep., 9, (1988), 1-163, doi: 10.1016/0167-5729(88)90009-X.

[4] H. D. Röhrig et al., Nucl. Eng. Des., 34, (1975), 157-167, doi: 10.1016/0029-5493(75)90164-8.

[5] R. G. Hickman, J. Less-Common Met., 19, (1969), 369-383, doi: 10.1016/0022-5088(69)90182-9.

[6] T. Shiraishi et al., J. Nucl. Mater., 254, (1998), 205-214, doi: 10.1016/S0022-3115(97)00362-0.

[7] T. Hayashi et al., Fusion Eng. Des., 89, (2014), 1520-1523, doi: 10.1016/j.fusengdes.2014.03.069.

Chapter 3. Characterization of LTZO

Outline

This chapter delves into an extensive characterization of LTZO ($Li_{2.4+x}TiZr_{0.2}O_{3.6+y}$) pebbles from a fusion engineering perspective, commencing with an introduction of Li_2TiO_3 based on a Li_2O-TiO_2 system. The discussion further reveals the foundational understanding of LTZO. Based on the literature, its crystal structure is anticipated, followed by a diligent examination of its properties through various fundamental analyses such as SEM-EDX, XPS, and XRD. The chapter concludes with a summary listing the critical discoveries.

3.1 Characteristics of Li_2TiO_3

A Li-Ti-O ternary oxide necessitates a Li_2O-TiO_2 phase diagram [1] from the viewpoint of material science. Figure 3.1 shows many combinations of ternary oxide by the mole ratio between Li_2O and TiO_2. Additionally, it indicates that Li_2TiO_3 has different phases depending on the temperature. α-Li_2TiO_3 is the one that is metastable and quickly transforms to β-Li_2TiO_3 by heat treatment above 573 K. The β-Li_2TiO_3 is the one that is stable from room temperature to 1428 K and converts to γ-Li_2TiO_3 above 1428 K. Considering the highest temperature of the blanket [2, 3], Li_2TiO_3 pebbles loaded in the blanket modules are always in the β-Li_2TiO_3 phase.

Narrowing down to β-Li_2TiO_3 based on the blanket temperature region, it exists as a single phase in the molar fraction of TiO_2 ranges from 47 to 51.5%. This range is converted in the ratio between Li and Ti to 1.88 < Li/Ti < 2.26. In other words, the β-Li_2TiO_3 can accommodate extra Li_2O as a solid solution without losing its physical properties. This is why QST pursues the pebbles with higher Li density and develops over-stoichiometric β-Li_2TiO_3-based pebbles.
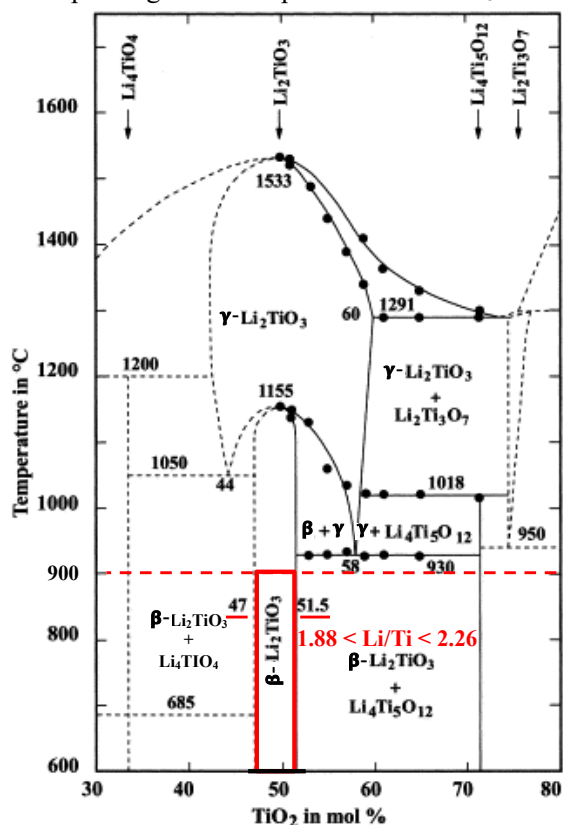

Figure 3.1. Li_2O-TiO_2 diagram [1]

Figure 3.2 illustrates the ideal crystal structure of the β-Li_2TiO_3 [4] from an inorganic material database, Atom Work [5]. It is visualized by VESTA version 3.5.8, a 3D visualization program for structural models

and volumetric data [6]. As can be seen, it exhibits a monoclinic C2/c crystal system with a Li, Ti, and O atom arrangement. It stacks a layer of six Li sites (Li6), a layer of six O sites (O6), and a layer of two Li and four Ti sites (Li2Ti4) along the [001] direction. These layers are composed of the unit cell. Li, Ti, and O atoms are allocated to three, two, and three sites, respectively. All the sites are thoroughly packed in the ideal condition. The cations (i.e., Li^+ and Ti^{2+}) occupy the octahedral sites surrounded by O^{2-} sites. Database of Ionic Radii [7] says their ionic radius is close to each other (Li^+: 0.76 Å, Ti^{4+}: 0.61 Å) when their coordinate number is six. On the other hand, O^{2-} is about twice as large as them.
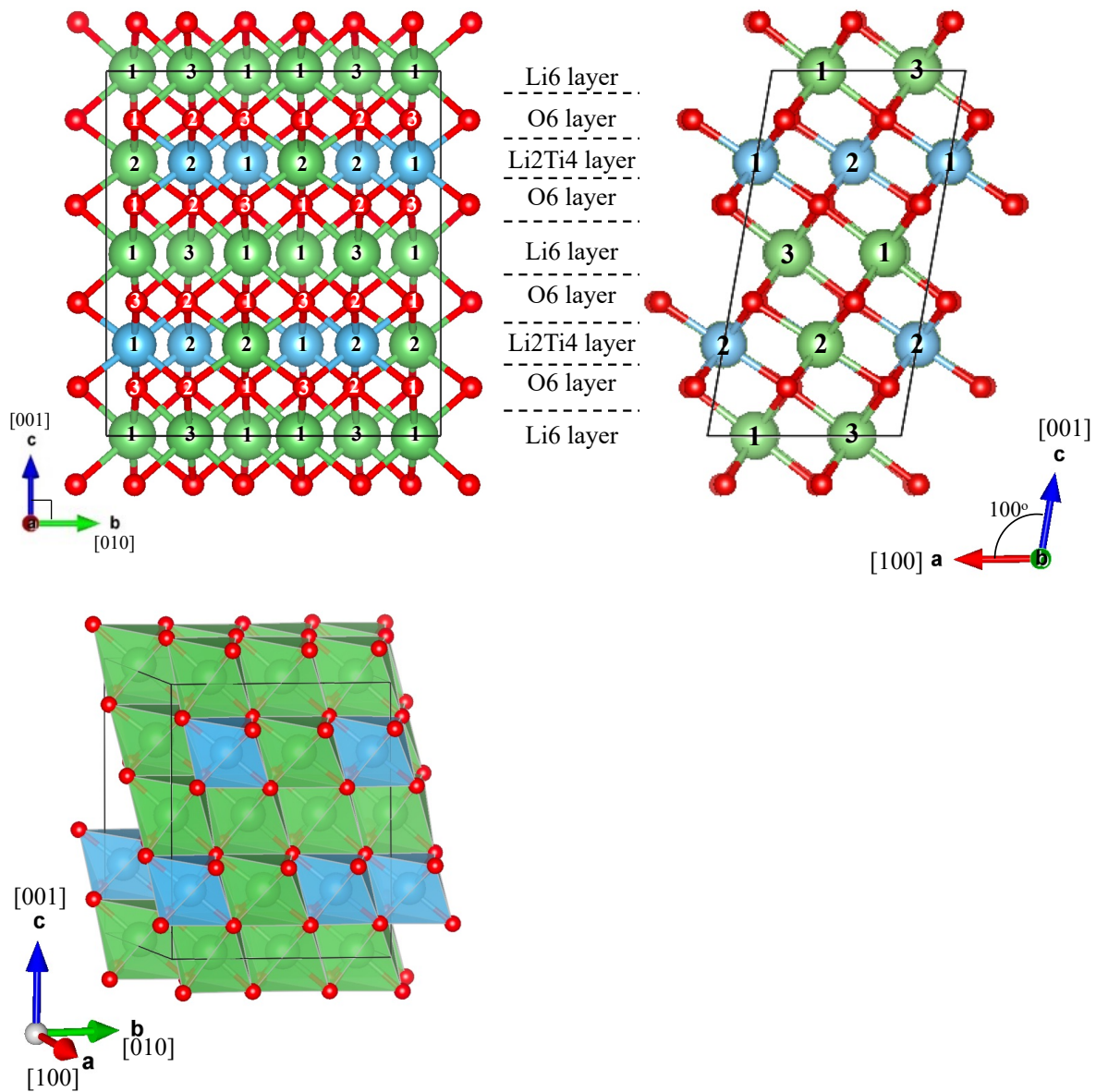

Figure 3.2. Schematic of the β-Li_2TiO_3 unit cell, coloring Li, Ti, and O in green, blue, and red, respectively.

(top left). (100) plane showing each element's sites.

(top right). (010) plane showing each site of Li and Ti.

(bottom). Cations positioned at the octahedral sites surrounded by O.

3.2 Foundation of LTZO Ceramic Pebbles

QST has conducted tremendous research and development activities for tritium breeding material to attain higher TBR. These activities found that Li_2TiO_3 mono-phase with extra Li has good material stability and guarantees good tritium productivity. An advanced tritium breeding material, LTZO, was recently developed by QST [8-10] and described as $Li_{2.4+x}TiZr_{0.2}O_{3.6+y}$. It is the most promising Li_2TiO_3-based ceramic pebble that has higher Li density than ordinary Li_2TiO_3 pebbles thanks to the additional 20 wt% of Li_2ZrO_3 without losing chemical stabilities.

The previous study [8] elaborates on synthesizing the LTZO pebble. It is made from $Li_{2+x}TiO_{3+y}$, composed of $LiOH \cdot H_2O$ and H_2TiO_3, and Li_2ZrO_3 derived from Li_2CO_3 and ZrO_2. The fabrication process also includes a slurry whose ingredients are $Li_{2+x}TiO_{3+y}$ powder, water, and a binder. Then, $Li_{2+x}TiO_{3+y}$ with 20 wt% Li_2ZrO_3 with slurry is mixed well with a ball mill and calcinated at 873 K to become an oxide consisting of Li, Ti, Zr, and O. Finally, it is sintered at 1373 K to obtain desirable grain size and densify. Its sintering temperature is roughly 70% of its melting point of 1813 K [11].

Its density is 83.4% of the theoretical density of 3.43 g cm^{-3}. The rest are pores and channels for tritium migration. XRD detects only a single phase of Li_2TiO_3 because Zr can solute perfectly into the crystal structure. Consequently, some are lost during the heat treatment, and then the ratio of Li/Ti becomes reportedly 2.15. The size and sphericity of pebbles are carefully controlled to avoid cracking induced by swelling due to neutron irradiation and to pack more into the blanket efficiently.
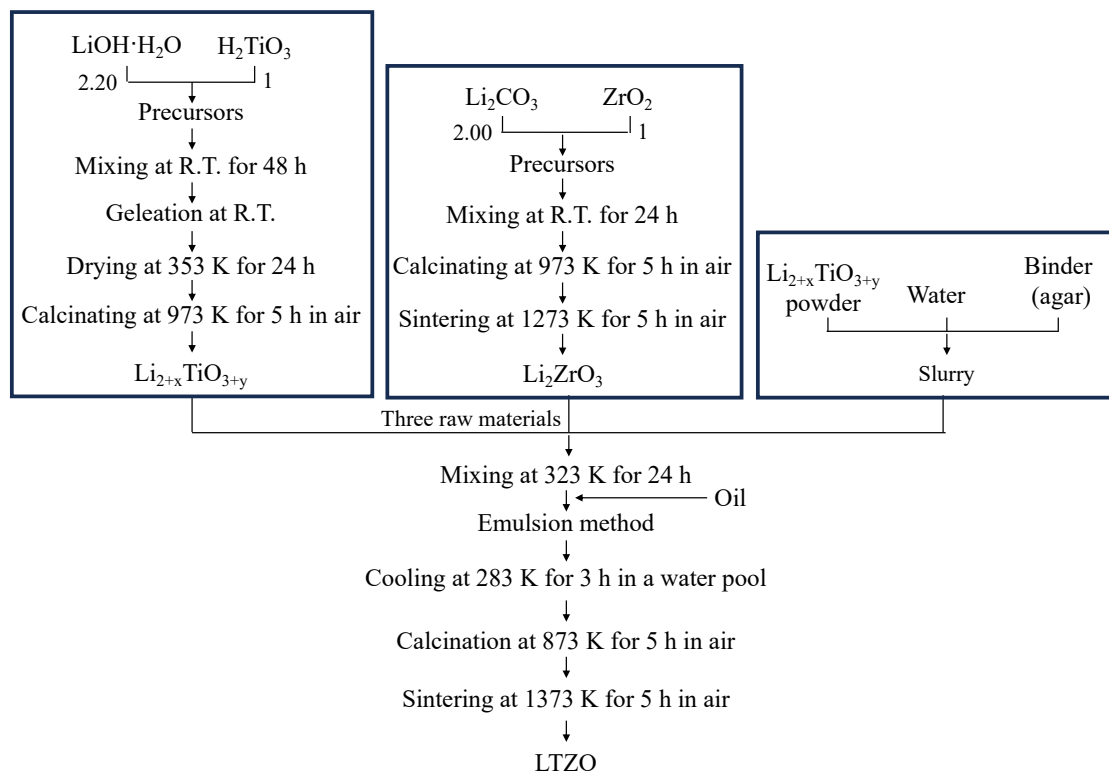

Figure 3.3. Fabrication process of the LTZO pebbles [8].

QST generously supplied 100 g of the LTZO sample, which is equivalent to about 5000 pebbles. It should be noted that [6]Li enrichment was never performed; thus, the LTZO sample contains 7.5% of [6]Li and 92.5% of [7]Li. Additionally, the sample shows low sensitivity to get charged, mainly through frictional interactions. As seen in Figure 3.4, it looks genuinely white and sphere and is almost 1 mm in diameter. All the samples have been stored in a vacuum.
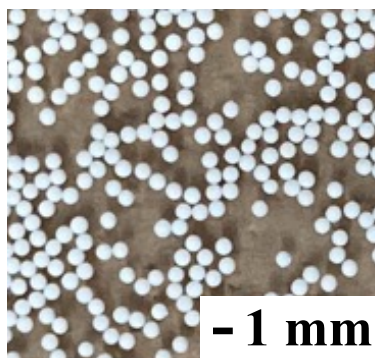

Figure 3.4. Appearance of the LTZO pebbles.

3.3 Properties of LTZO

3.3.1 Anticipation of LTZO's Characteristics.

The general explanation mentioned above helps guess LTZO's characteristics. Primarily, the careful discussion of $Li_{2+x}TiO_{3+y}$ pebble is followed. In either case of β-Li_2TiO_3 with excess Li or Ti, point defects play an essential role in possessing extra Li or Ti, depending on factors such as the temperature and O_2 partial pressure. In the case of β-Li_2TiO_3 with extra Li, Li^+ ions are expected to be in interstitial sites or be incorporated as an anti-site defect (Li_{Ti}^{3-}), providing charge compensation [12-15]. Neutron diffraction experimentally confirmed that Ti defects in the Li2Ti4 layer permit Li^+ to be at site number 2 to fit the tetrahedral site [16]. It is clarified with density functional theory calculation that Li^+ ions at the tetrahedral site are unstable and expected to evaporate priority.

Therefore, it is expected that the LTZO also should have some intrinsic point defects that help house extra Li. Additionally, the iconic radius of Ti^{4+} and Zr^{4+} are close to one another (Ti^{4+} 0.61 Å, Zr^{4+} 0.72 Å) [7]. Zr belongs to the same group as Ti. Thus, Zr atoms can solute not interstitially but substitutionally with some Ti atoms. Hence, the solid solution strengthening should appear in the LTZO grains.

The following fundamental analyses were performed to characterize the LTZO sample from a fusion engineering perspective and see if the above expectation is reasonable. The samples for XPS, XRD, SEM-EDX, surface area, and porosity analysis were heated in advance at 573 K, which corresponds to the lowest temperature in the blanket region, to eliminate impurities effects like adsorbed water vapor. They were heated until vapor release ceased and continuously monitored with a hygrometer (MDH-50, SHIMADZU Co.). As a reference material of the ordinary stoichiometric Li_2TiO_3, Pebble200 pebbles, which QST also presented, were used to compare.

3.3.2 XPS

XPS analysis (AXIS-165, Kratos Analytical Ltd.) was conducted to ensure that the received LTZO sample is genuinely composed of Li_2O, TiO_2, and ZrO_2 compared to Pebble200. SRD20 (Standard Reference Data) version 4.1 [17] was used as a reference to identify the signals. LTZO and Pebble200 were stabilized with carbon tape and placed in their original form on the stage without being ground into powders. Pebble200 tends to become easily charged by electrons during photon emission and friction, shifting the spectrum position and distortion. Additionally, the surfaces of both samples are subject to contamination with hydrocarbon. As a result, an adjustment was made to the obtained XPS spectrum based on the peak from C 1s orbit, which has a binding energy of 284.6 eV. The following discussion primarily focuses on the signals from Li 1s, Ti 2p, Zr 3d, and O 1s orbits.

As seen in Figure 3.5, the XPS signals revealed that the position and width of the peaks from the Li 1s, Ti 2p, and O 1s orbits of the LTZO closely aligned with those of Pebble200. Moreover, the peak corresponding to the Zr 3d orbit matched that of ZrO_2. In short, the XPS analysis affirmed that the LTZO comprised Li_2O, TiO_2, and ZrO_2. A notable discrepancy was observed in the intensity of the peaks from the Li 1s, O 1s, and Ti 2p orbits despite LTZO having larger Li and O contents than Pebble200. It might arise from the point defects accommodating additional Li and surface relaxation or reconstruction to minimize its potential energy. Generally, the detected signal primarily originates from the top few nanometers of the material without a depth profile. Hence, the lower intensity from the Li 1s and O 1s orbits in the LTZO did not necessarily mean that their contents were lower than those of the Pebble200. Therefore, this explanation could be extended to grasp the conformity in signals from the Ti 2p orbit, even though the LTZO signal should be less than the Pebble200 due to the partial replacement of Ti.
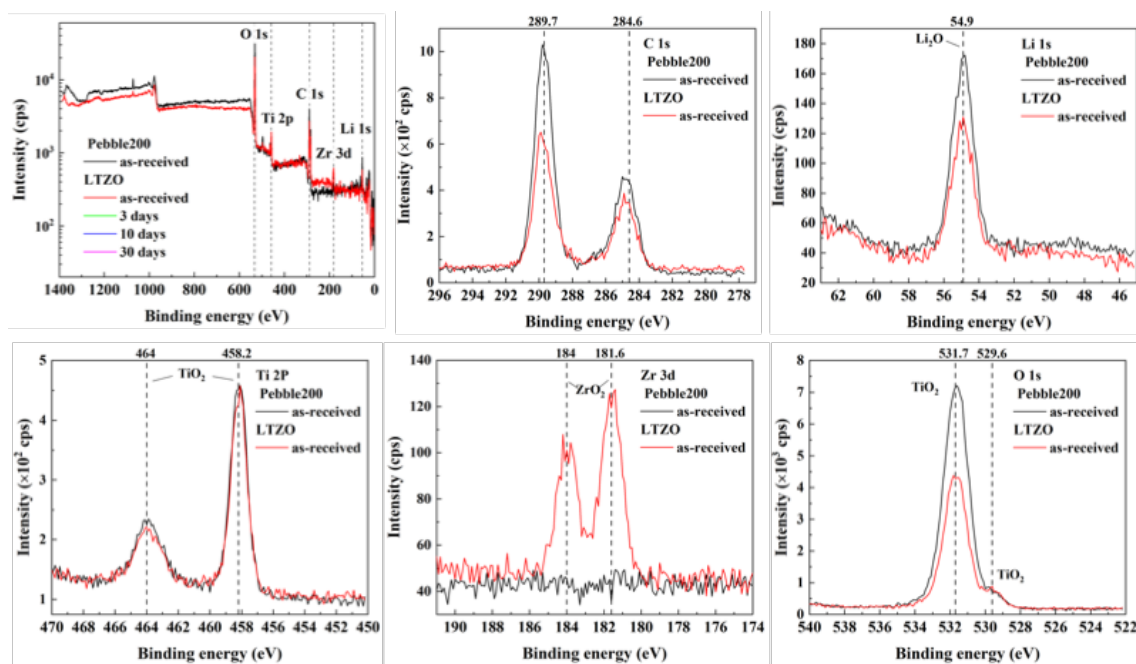

Figure 3.5. XPS signals with background signals, showing (top left) overall, (top center) C 1s, (top right) Li 1s, (bottom left) Ti 2p, (bottom center) Zr 3d, and (bottom right) O 1s orbits.

3.3.3 XRD

XRD analysis (SmartLab SE, Rigaku Co.) was conducted to ensure that the received LTZO sample is genuinely in the β-Li$_2$TiO$_3$ compared to the Pebble200. A reference of the β-Li$_2$TiO$_3$ was seized from ICSD (Inorganic Crystal Structure Database) [18] to identify the signals. Generally, the electrical insulation properties of the samples do not influence the XRD analysis, unlike XPS. Thus, LTZO and Pebble200 were placed neatly on the stage in their original form without being ground into powders.

Figure 3.6 assures that the Pebble200 possesses the β-Li$_2$TiO$_3$ crystal structure, as evidenced by its close resemblance to the reference pattern [19]. In contrast, the XRD signal from the LTZO did not exhibit a definitive similarity to the β-Li$_2$TiO$_3$. Nonetheless, it was observed that LTZO shares two significant peaks with the reference and the Pebble200 patterns. Also, the Li$_2$ZrO$_3$ pattern [20] was not observed, so additive Zr solutes substitutionally with Ti. As Zr expanded the lattice, the increased lattice constant resulted in the peak shift to the lower angle. The reason why major peaks have been missed, especially at 18.70 degrees, has yet to be identified. The calcination and sintering temperatures [8] are higher than the threshold temperature [1] for the phase transition from α-Li$_2$TiO$_3$ to β-Li$_2$TiO$_3$. The transition from a stable to a meta-stable phase does not occur naturally. These deny the existence of the α-Li$_2$TiO$_3$. Hence, the same explanation in section 3.3.2 addresses this discrepancy for now. In other words, the bulk had the same crystal structure as the β-Li$_2$TiO$_3$. Consequently, this investigation presented an unclear interpretation regarding the crystal structure of LTZO.
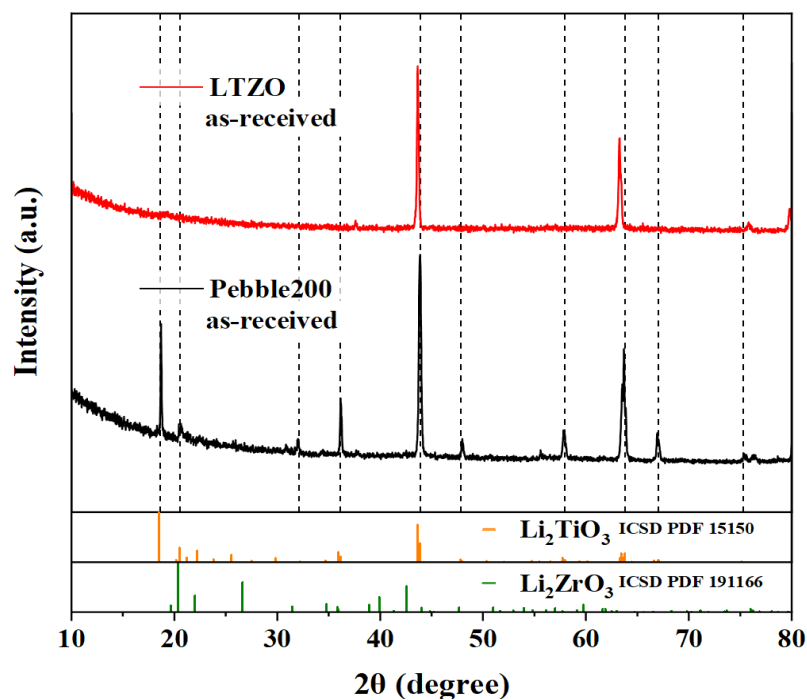

Figure 3.6. XRD spectrum from the LTZO in red, the Pebble200 in black, and the reference in orange.

3.3.4 TDS

A TDS analysis used a hygrometer (MAH-50D, SHIMADZU Co.) to obtain the water vapor desorption property. This is necessary to anticipate the dynamics of Li mass loss behavior and tritium release behavior, especially at the initial stage of the operation. To prevent the device from overshooting vapor concentration, the sample amount was limited to 0.5 g. The samples were heated from ambient temperature to 1173 K at the rate of 5 K min^{-1}, subsequently maintaining it at 1173 K, considering the blanket temperature range [2, 3]. Either 1×10^5 Pa Ar or 1×10^3 Pa H$_2$/Ar gas at the flow rate of 400 mL min^{-1} was introduced to the sample bed to discern any difference induced by the reducing H$_2$ gas, considering the tritium extraction purging gas species [9, 21]. The following discussion accentuates the desorption of the chemisorbed water vapor because of the negligible relevance of physisorption after the operation starts.

Figures 3.7 and 3.8 elucidate that the LTZO exhibited versatile water vapor release mechanisms, with some similarities to other Li$_2$TiO$_3$ pebbles [22, 23]. As a result, they had three out of five peaks in common. The first peak at 486 K and the second peak at 593 K resulted from the desorption of the chemisorption. The third one at 767 K was derived from LiOH thermal decomposition. This LiOH seemed to originate from the raw ingredient's leftover [8] or to be gradually generated through the interaction with slight water vapor during the sample storage, as in equation (2.7).

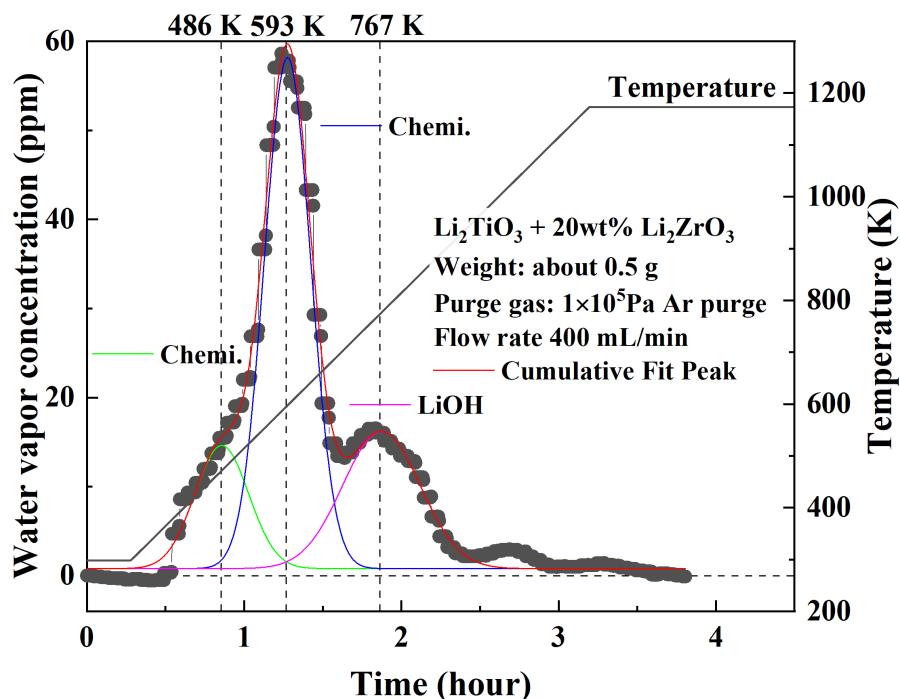$$2\text{LiOH} \rightarrow \text{Li}_2\text{O} + \text{H}_2\text{O}. \tag{3.1}$$

Figure 3.7. Water vapor desorption curve from the LTZO under the Ar atmosphere.

Meanwhile, two more outstanding peaks were detected exclusively under the reducing H_2 purging condition. Given LTZO's composition, these peaks were ascribed to the water formation reactions between H_2 and the oxides. The primary one at 993 K came from TiO_2, aligning with the peak temperature consistency observed in the previous work [23]. The secondary one at 1143 K was assumed to be an indigenous LTZO water vapor release peak, absent in Li_2TiO_3 and Li_2ZrO_3 pebbles [22-24]. Given this experimental temperature and oxygen partial pressure condition, Ellingham diagram firmly denies these reactions. Therefore, it can be said that the surface elements made these reactions possible. Also, this means that the lattice distortion induced by ZrO_2 leads to stabilization in a more energetically favorable configuration by reacting with the H_2 gas. This reaction manifested as a color transition to gray, as the previous work [25] reported. This oxygen-deficient reaction leads to oxygen vacancies.
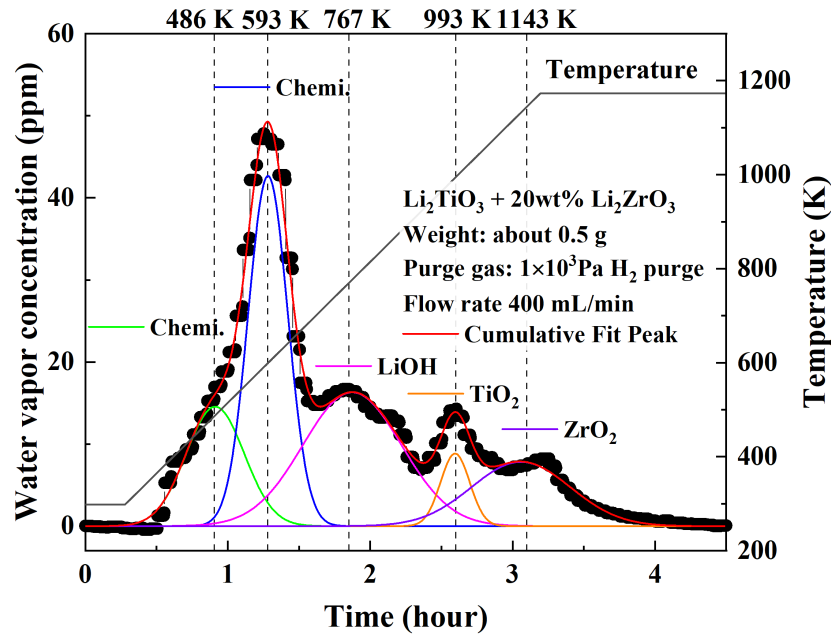
$$2TiO_2 + H_2 \rightarrow Ti_2O_3 + H_2O. \tag{3.2}$$

$$2ZrO_2 + H_2 \rightarrow Zr_2O_3 + H_2O. \tag{3.3}$$

Figure 3.8. Water vapor desorption curve from the LTZO under the H_2 atmosphere.
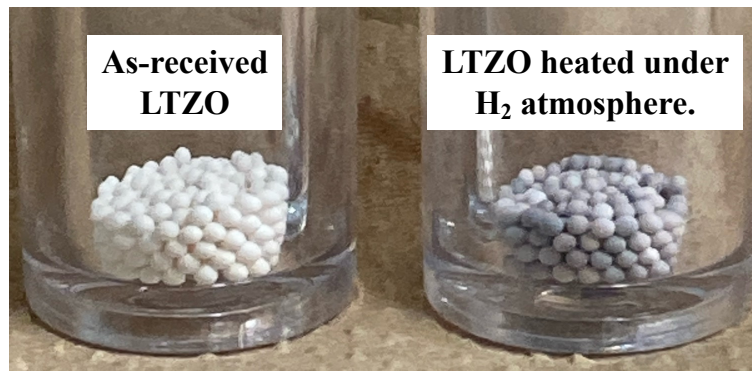

Figure 3.9. The appearance changes before and after heating the LTZO under the H_2 atmosphere.

3.3.5 SEM-EDX

The SEM-EDX analysis (JSM-IT500, JEOL Ltd.) was conducted to obtain fine-resolution images and elemental composition data of the ceramic pebble samples. Given that pebble surfaces are susceptible to contamination, commonly with hydrocarbons. Therefore, the focus of analysis is principally on the internal bulk rather than the surface of the LTZO. For the SEM imaging, the ceramic pebble was tightly pinched with tweezers and fractured into several pieces. The broken fragments were then placed on carbon tape. Depending on the region of interest, either the surface or the bulk, the orientation of the fractured pieces was adjusted to the electron gun. The working distance between the electron gun and the stage was around 10 mm, and the electron beam was accelerated to 10.0 keV to capture clear images. Representative SEM images of the surface and the internal structure are depicted in Figure 3.10. It shows that the LTZO sample did not have a Li_2CO_3 layer, and each grain looks distinguishable.
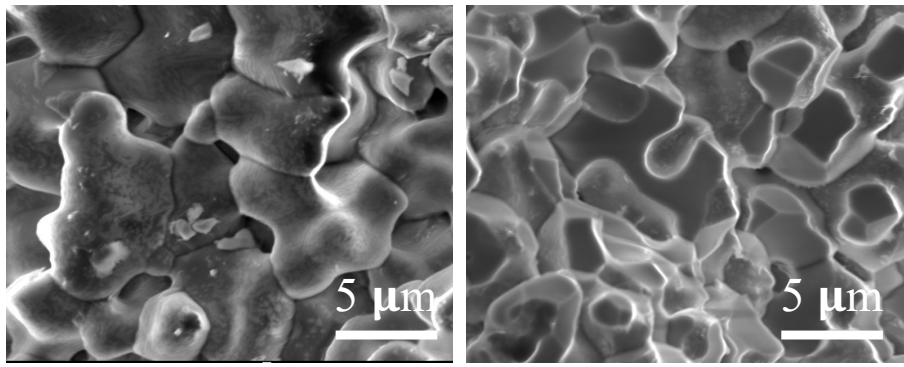

Figure 3.10. SEM image of the (left) surface and (right) internal of the LTZO pebble.

In the image analysis, 30 grains were randomly selected, and their average diameter was determined to be 3.3 μm using ImageJ version 1.53t 24 August 2022 [26], a public-domain Java image processing program. This value is as large as the target grain size of 5 μm, considered optimal for prompt tritium release. Figure 3.11 illustrates the grain size distribution.
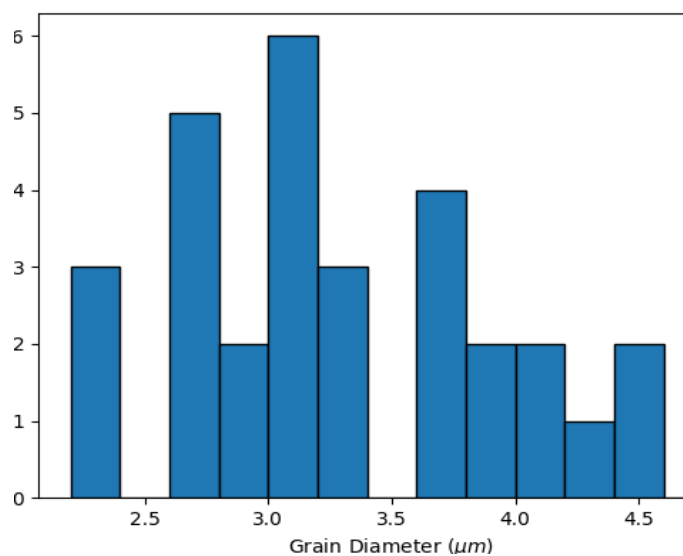

Figure 3.11. Histogram of the sampled grain diameter.

Figure 3.12 presents the corresponding elemental distributions. This work excluded the EDX signals for impurities from the data interpretation, such as C and Al, which came from the carbon tape and sample stage. Thus, the elemental analysis focused on Ti, Zr, and O. This device cannot detect Li. The atomic ratios of Ti, Zr, and O were 11.3, 3.3, and 85.4, respectively.
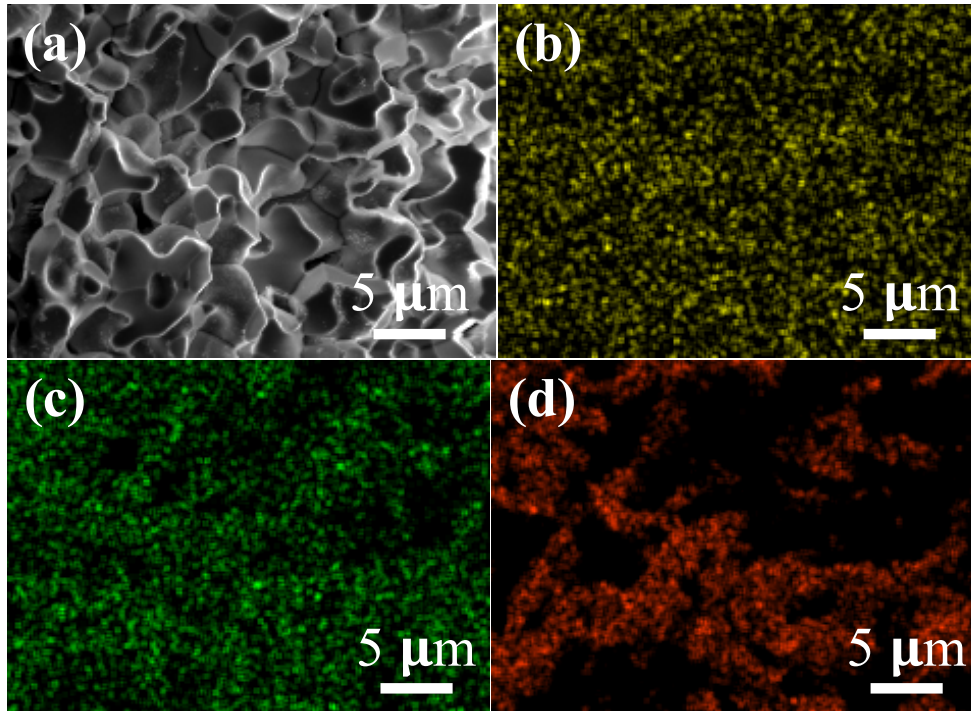

Figure 3.12. SEM-EDX images of (a) the internal of the LTZO pebble,
(b) the Ti-K line, (c) the Zr-L line, and (d) the O-K line.

To express the stoichiometry of the LTZO, it is temporarily represented as $Li_iTi_jZr_kO_l$. Based on the initial composition, which included 20 wt% Li_2ZrO_3, the Zr content is expected to be less than or equal to 0.2, as in equation (3.4). Additionally, some Ti sites are anticipated to be substituted by Zr, expressed in equation (3.5). The Li/Ti ratio is reported to be 2.15 [8], so it can be reinterpreted that the proportion of Li to Ti and Zr, Li/(Ti + Zr), was 2.15, according to equation (3.6). Furthermore, the overall electric charge of the LTZO should be zero, as indicated by equation (3.7). The atomic ratio was applied only for equation (3.5) because external factors amplify the O signal effortlessly. Considering these constraints, the stoichiometric chemical composition of LTZO was determined as $Li_{2.15}Ti_{0.8}Zr_{0.2}O_{3.075}$.

$$k \leq 0.2. \tag{3.4}$$

$$j + k = 1. \tag{3.5}$$

$$i / (j + k) = 2.15. \tag{3.6}$$

$$i + 4j + 4k - 2l = 0. \tag{3.7}$$

3.3.6 Surface Area and Porosity Analysis

The surface area and porosity analysis (TriStar II 3020, SHIMADZU Co.) were also conducted to obtain physical properties influencing the tritium release behavior. Those two properties were acquired by introducing inert N_2 gas into the test tube filled with a few pebbles at liquid nitrogen temperature 77 K. The samples were loaded as they were without shattering or powdering.

The adsorption and desorption isotherm of the LTZO is shown in Figure 3.13. IUPAC [27] classifies these isotherms as IUPAC type II, whose reversible isotherms are given by the physisorption of most gasses on non-porous or macro-porous (> 50 nm) adsorbents. A soaring in adsorption was observed at a relative pressure of 0.9 or higher, indicating the presence of macro-pores or the aggregation of particles with small grins. Point B - the beginning of the middle almost linear section of the isotherm - indicates the stage at which mono-layer coverage is complete and multi-layer adsorption is about to commence. While the Pebble200 had a distinctive Point B, the LTZO had a gradual curvature. This indicates that mono-layer coverage and multi-layer adsorption were significantly overlapped. It turned out that the adsorption capacity of the LTZO was less than that of the Pebble200.
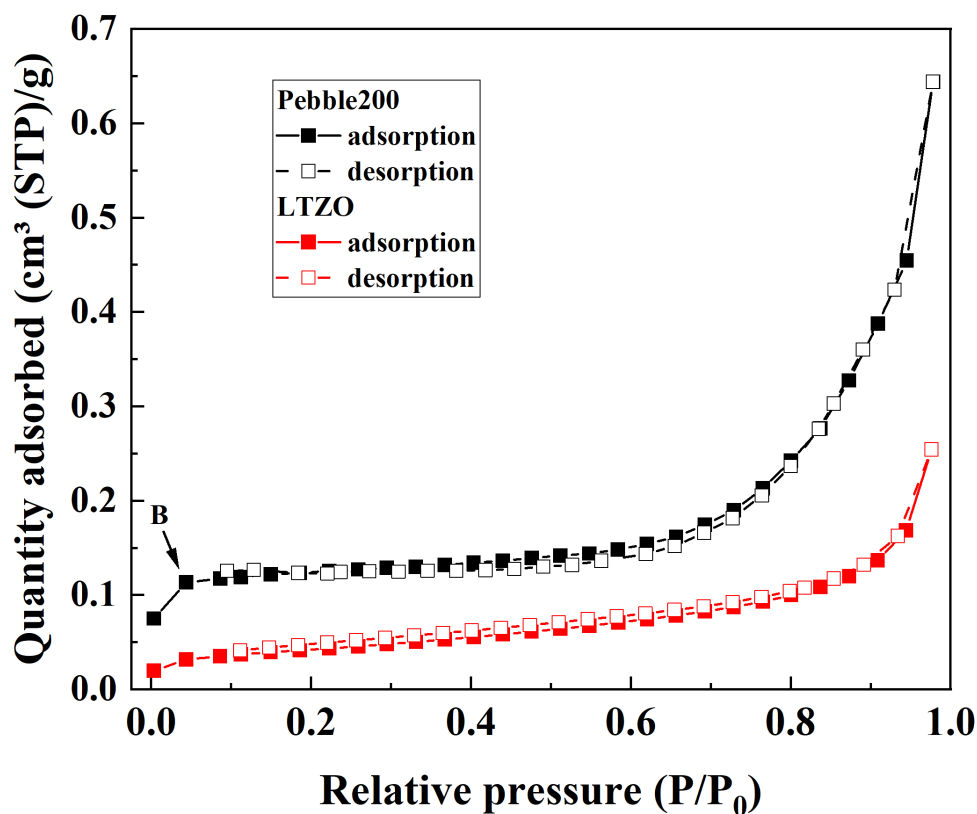

Figure 3.13. Adsorption and desorption isotherm of LTZO and Pebble200.

The BET method can apply to samples classified as IUPAC type II. As shown in Figure 3.14, a line expressed by equation (2.1) is extended to the experimental plots in the range of 0.08 to 0.25 relative pressure

of the isotherm. As a result, equation (2.3) resulted in the BET-specific surface areas of 0.15 and 0.40 $m^2\,g^{-1}$ for the LTZO and Pebble200, respectively. Equation (2.4) obtained the theoretical surface area. As mentioned earlier, 83.4% of the theoretical density and the 3.3 μm average grain diameter were substituted, and then t was calculated to 0.64 $m^2\,g^{-1}$. This difference between the theoretical and BET-specific surface area was 0.49 $m^2\,g^{-1}$.
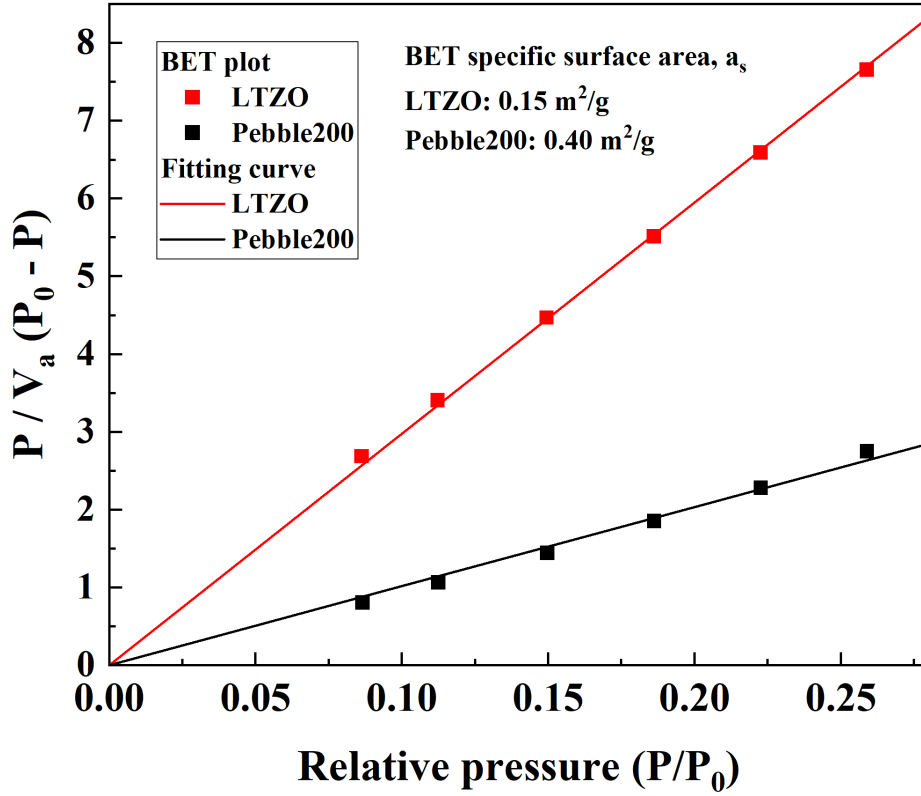

Figure 3.14. Application of BET equation to the isotherm plots.

The N_2 adsorption method goes well with the analysis for the micro-pores (< 2 nm) and meso-pores (< 50 nm) size distribution. Meanwhile, the isotherm illustrates that LTZO mainly consisted of many macro-pores. So, it was impossible to investigate the pore size distribution. Mercury intrusion porosimetry, for example, can be an alternative method.

3.4 Summary

Chapter 3 comprehensively characterizes LTZO ($Li_{2.4+x}TiZr_{0.2}O_{3.6+y}$) ceramic pebbles to build a solid understanding from a fusion engineering standpoint. A comprehensive compilation of the principal discoveries of the received LTZO through literature research, in-depth discussion, and fundamental analysis is presented here.

Key Findings:

1. **Literature Research**: The LTZO was expected to have the same crystal structure as β-Li_2TiO_3 with some point defects to facilitate extra Li accommodation.

2. **XPS Analysis**: The LTZO sample comprised Li_2O, TiO_2, and ZrO_2.

3. **XRD Analysis**: The LTZO probably was in the β-Li_2TiO_3 phase and showed no Li_2ZrO_3 pattern, which meant Zr solute substitutionally with Ti.

4. **TDS Analysis**: The LTZO had versatile water vapor release mechanisms: chemisorption, LiOH thermal decomposition, and water formation reaction due to the chemical interaction of oxides with H_2 gas.

5. **SEM-EDX Analysis**: The LTZO comprised many grains, which are 3.3 μm in diameter on average and fulfill the desirable maximum grain size of 5 μm. The stoichiometric chemical composition of LTZO was determined as $Li_{2.15}Ti_{0.8}Zr_{0.2}O_{3.075}$.

6. **Surface Area and Porosity Analysis**: The LTZO had fewer micro-pores (< 2 nm) and meso-pores (< 50 nm) and possibly more significant macro-pores (> 50 nm). The BET-specific surface area of LTZO was found to be 0.15 m^2 g^{-1}, in contrast to the theoretical specific surface area of 0.64 m^2 g^{-1}.

The following chapters discuss Li mass loss behavior and tritium release behavior based on these key findings. The provided LTZO was expected to have the same monoclinic crystal structure as the β-Li_2TiO_3 for now.

References

[1] H. Kleykamp, Fusion Eng. Des., 61-62, (2022), 361-366, doi: 10.1016/S0920-3796(02)00120-5.

[2] Y. Someya et al., Fusion Eng. Des., 146, (2019), 894-897, doi: 10.1016/j.fusengdes.2019.01.107.

[3] Y. Kawamura et al., Fusion Eng. Des., 161, (2020), 112050, doi: 10.1016/j.fusengdes.2020.112050.

[4] J. Claverie et al., Bull. Soc. Chim. Fr., (1966), 244-246.

[5] Y. Xu et al., Jpn. J. Appl. Phys., 50, (2011), 11RH02, doi: 10.1143/JJAP.50.11RH02.

[6] K. Momma et al., J. Appl. Crystallogr., 44, (2011), 1272-1276, doi: 10.1107/S0021889811038970.

[7] R. D. Shannon, Acta. Cryst., A32, (1976), 751-767, doi: 10.1107/S0567739476001551.

[8] T. Hoshino, Nucl. Mater. Energy, 9, (2016), 221-226, doi: 10.1016/j.nme.2016.05.004.

[9] Y. Kawamura et al., Fusion Eng. Des., 136, (2018), 1550-1556, doi: 10.1016/j.fusengdes.2018.05.055.

[10] T. Hoshino et al., J. Plasma Fusion Res., 93-02, (2017), 83-90, in Japanese.

[11] LTS Research Laboratories, Inc., Safety Data Sheet, Lithium Titanium Oxide. Retrieved November 22, 2023, from https://www.ltschem.com/msds/Li2TiO3.pdf.

[12] J. J. Bian et al., Mater. Sci. Eng. B, 176, (2011), 147-151, doi: 10.1016/j.mseb.2010.10.016.

[13] Y. Hao et al., J. Mater. Chem., 22, (2012), 23885-23892, doi: 10.1039/C2JM33788F.

[14] K. Mukai et al., J. Nucl. Mater., 442, (2013), S447-S450, doi: 10.1016/j.jnucmat.2013.04.050.

[15] S. T. Murphy et al., Chem. Mater., 26, (2014), 1629-1638, doi: 10.1021/cm4038473.

[16] M. Vijayakumar et al., J. Phys. Chem. C, 113, (2009), 20108-20116, doi: 10.1021/jp9072125.

[17] NIST X-ray Photoelectron Spectroscopy Database, NIST Standard Reference Database Number 20, National Institute of Standards and Technology, Gaithersburg MD, 20899 (2000), doi:10.18434/T4T88K, (retrieved April 25, 2023).

[18] NIST Inorganic Crystal Structure Database, NIST Standard Reference Database Number 3, National Institute of Standards and Technology, Gaithersburg MD, 20899, doi: https://doi.org/10.18434/M32147, (retrieved April 25, 2023).

[19] J. F. Dorrian et al., Mater. Res. Bull, 4, (1969), 179–184, doi: 10.1016/0025-5408(69)90054-3.

[20] Y. V. Baklanova et al., J. Solid State Chem., 298, (2013), 43-49, doi: 10.1016/j.jssc.2013.09.030.

[21] R. Hiwatari et al., Fusion Eng. Des., 143, (2019), 259-266, doi: 10.1016/j.fusengdes.2019.03.174.

[22] R. Yamamoto et al., Fusion Eng. Des., 124, (2017), 781-791, doi: 10.1016/j.fusengdes.2017.04.004.

[23] T. Hanada et al., J. Nucl. Mater., 417, (2011), 735-738, doi: 10.1016/j.jnucmat.2010.12.130.

[24] T. Kanazawa et al., Fusion Sci. Technol., 60, (2017), 1167-1170, doi: 10.13182/FST11-A12623.

[25] T. Kinjyo et al., Fusion Eng. Des., 83, (2008), 580-587, doi: 10.1016/j.fusengdes.2007.11.011.

[26] C. A. Schneider et al., Nat. Methods, 9, (2012), 671-675, doi: 10.1038/nmeth.2089.

[27] K. S. W. Sing et al., Pure Appl. Chem., 57, (1985), 603-619, doi: 10.1351/pac198557040603.

Chapter 4. Li Mass Loss Behavior

Outline

This chapter describes Li mass loss behavior from the LTZO pebbles. First, the background and aim of this work are briefly explained. Next, the Li mass loss behavior is elucidated through experiments. Then, fundamental material analyses discuss the long-term heating effects on the material properties. Subsequently, a one-dimensional simulation assessed the impact of the Li mass loss rate on tritium production. Finally, a summary of the results of this chapter is presented.

4.1 Introduction

The current JA-DEMO design employs the Li_2TiO_3 ceramic pebbles as the tritium breeding material [1, 2]. In this case, some Li interacts with the water vapor in the sweep gas to extract tritium, resulting in Li mass loss. This phenomenon undermines the benefits of Li addition. Furthermore, Li-containing gas species may cause corrosion damage to adjacent structural materials. Moreover, it has yet to be evident how severe the structural changes that long-term usage in a harsh environment induces are, even though the blanket module is supposed to be used continuously for at least two years. Plus, the structural changes potentially cause any difference in tritium release properties. From the viewpoint of the feasibility of the tritium fuel cycle, it is necessary to investigate the Li mass loss phenomena experimentally and the long-term heating effects on the material to contribute to designing the blanket system. To fulfill the goals, this chapter aims to conduct experiments to identify the Li mass loss rate and structural changes. Then, a simulation employs the experimental data to investigate its transient effect on TBR in simplified blanket conditions.

4.2 Long-term Heating Experiment

This section aims to experimentally obtain the Li mass loss rate.

4.2.1 Experimental Procedure

The Li mass loss amount as Li_2O, M_{Li2O} [g], was calculated using equation (4.1). The water vapor desorption mass, M_{H2O} [g], was subtracted from the mass difference between the pre-heating mass, M_{bef} [g], and post-heating mass, M_{aft} [g]. An electronic microbalance scale (IUW-200D, AS ONE Co.) weighed the sample mass, and a hygrometer (MAH-50D, SHIMADZU Co. or QMA 2030, Michell Instruments Ltd.) measured the water vapor desorption mass. To facilitate comparison between samples and Pebble200 and to examine mass transitions over time, the Li mass loss was normalized by preheating mass. Dividing the Li mass loss by its stoichiometric ratio obtains the net Li mass loss amount.

$$M_{Li2O} = (M_{bef} - M_{aft}) - M_{H2O}. \tag{4.1}$$

Figure 4.1 depicts the schematic diagram of the experimental device. Basically, 0.5 g of the sample pebbles were packed in a quartz tube and stabilized by two pieces of quartz wool at both ends. Initially, dry Ar gas stream was introduced into the sample bed at 400 mL min^{-1} to remove the physisorption. Subsequently, it was switched to dry 1000 Pa H_2/Ar gas mixture at 400 mL min^{-1}. At the same time, the sample was heated by an electric furnace to 1173 K with a ramp rate of 5 K min^{-1} to remove the chemisorption. When it reached 1173 K, the temperature got constant for the target heating periods for 3, 10, and 30 days. Later, the mass flow rate was reduced to 50 mL min^{-1} to save gas consumption after confirming the completion of the water vapor release. Empirically, it is known that the flow rate is not critical to the Li mass loss behavior. The sweep gas contained roughly 10 ppm at a pressure of 1 Pa even right after passing through a regenerated molecular sieve 5A. This leads to the Li mass loss reaction represented in equation (2.7). After the heating periods passed, the furnace was turned off, and the sample cooled naturally to room temperature for weight measurement with minimal exposure to the air.

Also, H_2O purging experiments were conducted to gain the parameters expressed in equation (2.10). A CuO catalyst bed heated at 673 K converted a 500 ppm H_2/Ar gas mixture to a 50 Pa H_2O/Ar gas mixture. Then, the water vapor gas was introduced to the sample bed. The mass flow rate and temperature ramping rate setting were consistent with the H_2 purging conditions. Samples were heated at 1173 K for 1, 1.8, and 9 days. In addition, isothermal and isobaric experiments were conducted to investigate the water vapor and temperature dependences of the mass transfer coefficient, k, expressed in equation (2.10).
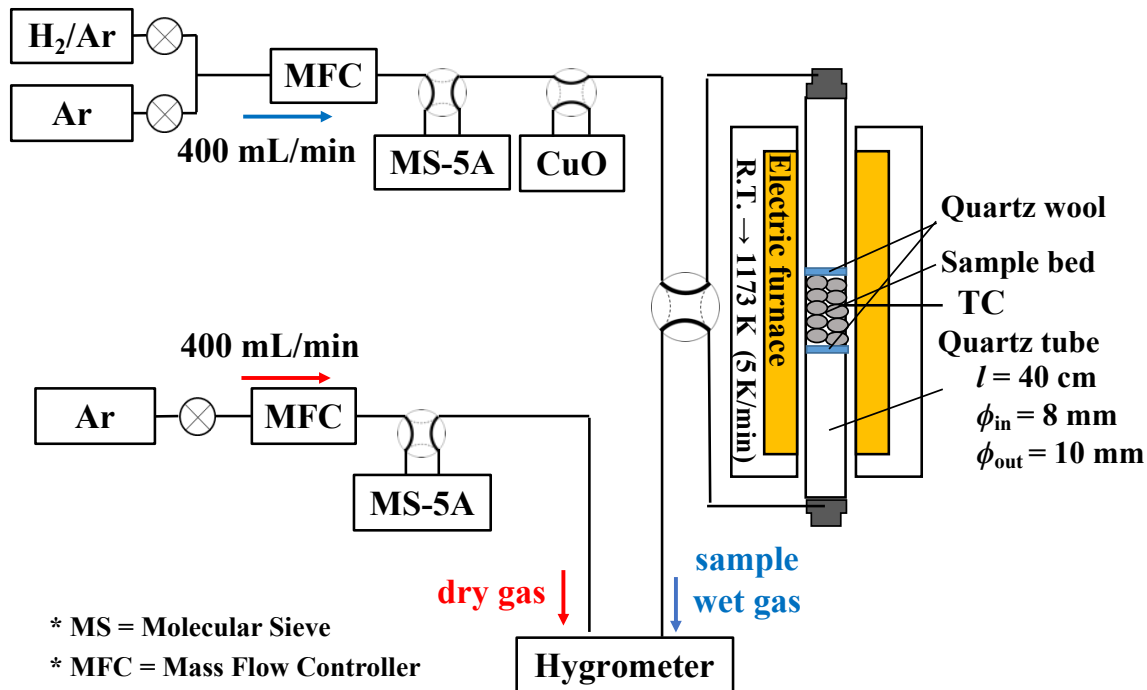

Figure 4.1. Experimental apparatus for the long-term heating experiment.

4.2.2 Results and Discussions

It was confirmed by a pH test paper that the white substance adhering to the quartz tube, which became visible when cooling down to room temperature, was LiOH. It should be noted that the pebble bed was entirely covered with a LiOH corrosive layer, as shown in Figure 4.2. In other words, the latest cylindrical blanket module design [1-3] has the potential risk of LiOH corrosion generated not only by direct contact [4-9] but also by mere evaporation. Also, the pebbles under H_2 purging turned gray mainly because of the reduction, and their color got darker and darker in proportion to the heating duration. On the other hand, they still looked pure white under H_2O purging conditions, no matter how long it was heated at 1173 K.

Based on these observations, another concern is that the tritium extraction sweep gas will carry the corrosive LiOH-containing gas to downstream piping. It was found that the LiOH-containing gas traveled as far as 14 cm from the pebble bed center. The extent of potential harm depends on the dispersion of LiOH, including its location, chemical state, and quantity. Previous studies [10-12] examined several aspects of material soundness for the LiOH blanket, including corrosion rate, weight loss, stress corrosion cracking, fatigue, and pitting. On top of these adverse effects, pressure drops and the piping system's obstruction may result from precipitation when it cools below its melting point of 735 K [13].

Conversely, the Li-containing corrosion layer covering the piping surface can produce tritium as far as the thermal neutrons reach. Still, it is concerned that its 4.78 MeV energy deposition may influence the corrosion layer, tritium production, and permeation [14]. Therefore, special attention should be paid to this matter, and further research is required to clarify the LiOH distribution and elucidate the potential effects on the surrounding materials to address these potential risks.
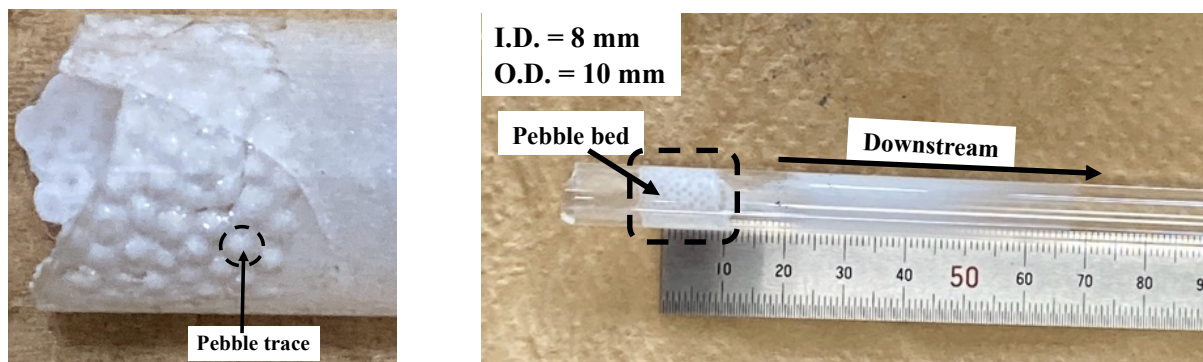

Figure 4.2. An example picture of the corrosion layer at (left) the pebble bed and on (right) the overall tube.

Figure 4.3 presents the pebble weight transition over time. Clearly, the LTZO lost Li more swiftly than Pebble200 in the H_2 atmosphere, and H_2O purging further accelerated the Li mass loss rate. A clear dependence on water vapor pressure was experimentally validated, indicating that the evaporation process expressed in equation (2.7) was more dominant than that of equations (2.5) and (2.6). Moreover, the experimental data reinforces the mass transfer model validity that Li_2O desorbs exponentially. According to

the model, Li_2O, equivalent to 1.5 wt% of LTZO, will eventually evaporate as LiOH. This figure corresponds to 5.6 wt% of Li depletion. The experimental observations revealed a gradual decrease in the Li / (Ti + Zr) ratio, from an initial value of 2.15 to 2.08 after 30 days under the H_2 conditions, eventually settling at 2.03. It took 140 days for the fitting curves to reach 2.03. In other words, it is inescapable that the LTZO will lose a nearly equivalent amount of the additional Li during the operation sooner or later. Li located at energetically unstable sites is expected to evaporate preferentially. Therefore, it is vital to carefully control the Li loss rate to draw on the higher Li density.

Furthermore, pH measurements provided additional insights. After three weeks of immersing both pebbles in tap water at room temperature, the pH level for an LTZO and Pebble200 pebble rose to 10.5 and 8.48, respectively. The definition of pH told that the LTZO markedly lost Li more than the Pebble200 by two orders of magnitude. This result also supported the mass transfer model that higher Li content increases Li mass loss. Despite both pebbles becoming soaked and fragile, they retained their spherical shape.
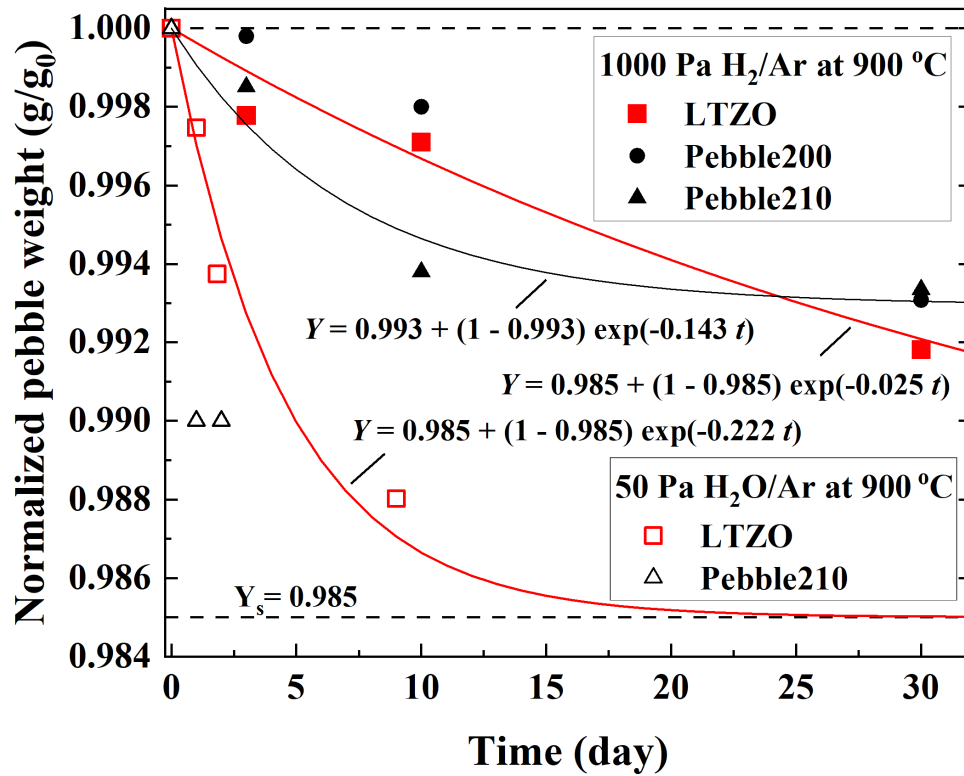

Figure 4.3. Time transition of the Li mass loss.

Pebble210 is over-stoichiometric Li_2TiO_3 ceramic pebble (Li/Ti = 2.10) [15].

To better understand the parameters expressed in equation (2.9), it is vital to carry out the isothermal and isobaric experiments in the domain where LTZO has room for losing Li. Based on the experimental data in Figure 4.3, the heating duration at 1173 K was limited to only 24 hours. The isothermal experiments were performed at 1173 K, varying the water vapor partial pressure at 18, 40, and 50 Pa. As seen in Figure 4.4, the fitting curve, which is proportional to the square root of the water vapor pressure, was applied to the experimental plots because the LiOH partial pressure, P_{LiOH} [Pa], can be described using the equilibrium constant, K_p [-], and water vapor partial pressure, P_{H2O} [Pa], as follows:

$$P_{LiOH} = K_p P_{H2O}. \tag{4.2}$$

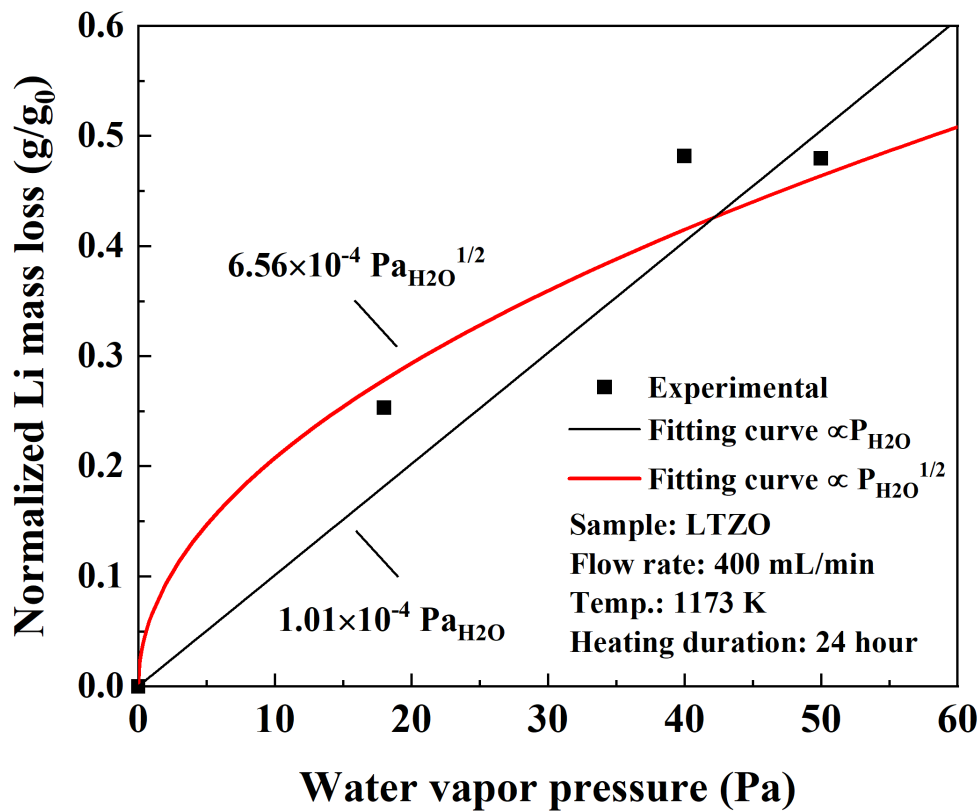
Figure 4.4. Isothermal experiments at 1173 K, varying water vapor pressure at 18, 40, and 50 Pa.

The isobaric experiments were performed under 50 Pa H_2O condition, varying the temperatures at 1173, 973, and 773 K. As seen in Figure 4.5, LTZO had a subtle temperature dependence. Its overall activation energy to lose Li was equivalent to 0.17 eV and extremely low. This implies that the generated LiOH quickly desorbs from the grain surface.
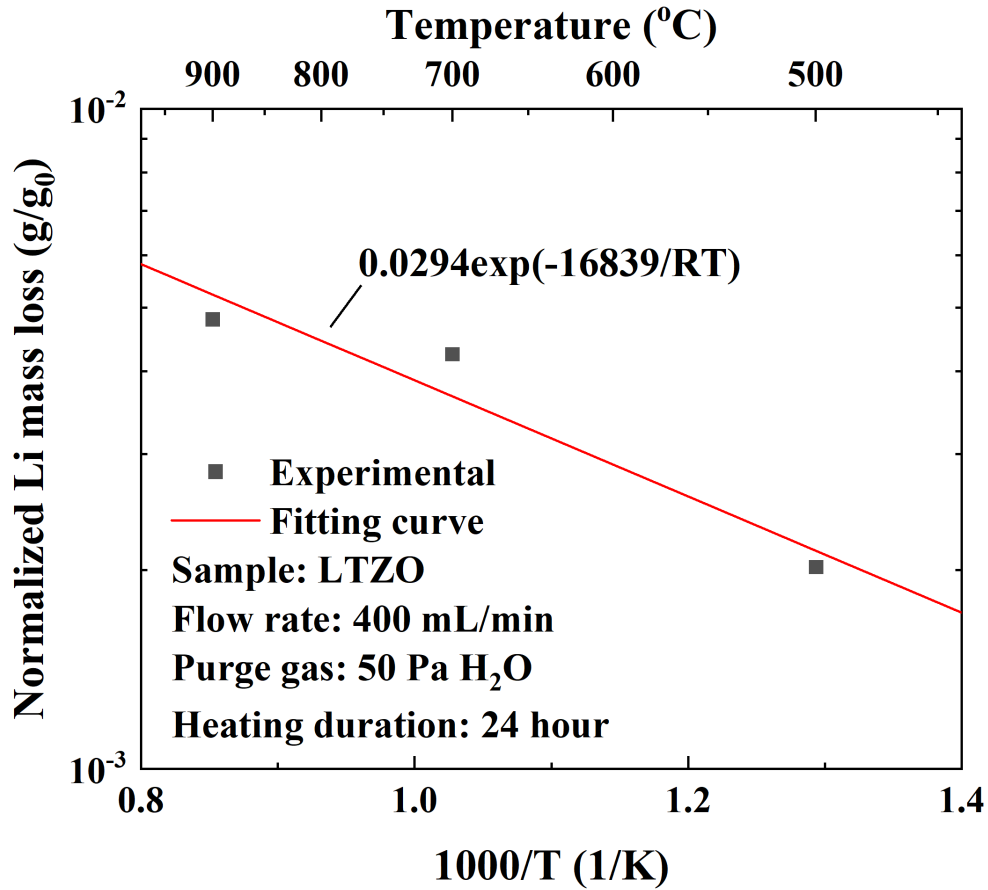

Figure 4.5 Isobaric experiments at 50 Pa H_2O, varying temperature at 1173,973, and 573 K.

Consequently, the following equation represents the Li mass loss rate. The stable component weight, Y_s, for the H_2O atmosphere was fixed at the value of the one for the H_2 atmosphere.

$$Y = 0.985 + 0.015 \exp(-0.029\, P_{H2O}^{1/2} \exp(-16839 / RT)\, t). \tag{4.3}$$

4.3 Structural Changes

This section attempts to identify structural changes due to long-term heating. The comprehensive analyses with the same method as in section 2.3 were performed on the sample heated for 3, 10, and 30 days.

4.3.1 XPS

As seen in Figure 4.6, the XPS analysis (AXIS-165, Kratos Analytical Ltd.) revealed that the intensity, position, and width of the peaks corresponding to the Li 1s and O 1s orbits of the LTZO closely align. Moreover, the peaks corresponding to the Ti 2p and Zr 3d orbits of the LTZO matched that of TiO_2 and ZrO_2. Even though Li_2O evaporates as LiOH and O depletion due to the water formation reaction equations (3.2) and (3.3), their peak intensities were not significantly changed. On the other hand, a decrease in the peak intensity of the heavier elements like Ti and Zr was observed. TiO_2 and ZrO_2 are chemically stable elements that should stay in the lattice. Thus, the coverage of the Li_2O weakened the signal, which the bulk supplied to the surface as soon as the LiOH generation because Li_2MO_3 ceramics (M = Ti, Mn, Sn, Ru, and Ir) are cation conductors. As seen in Fig.4.3, all the samples were in the middle of the Li depletion, and there still should be Li_2O left. In any case, no noticeable peaks for Ti_2O_3, Zr_2O_3, and LiOH were detected. Consequently, the XPS analysis affirms the compositional stability of LTZO heated for up to 30 days.
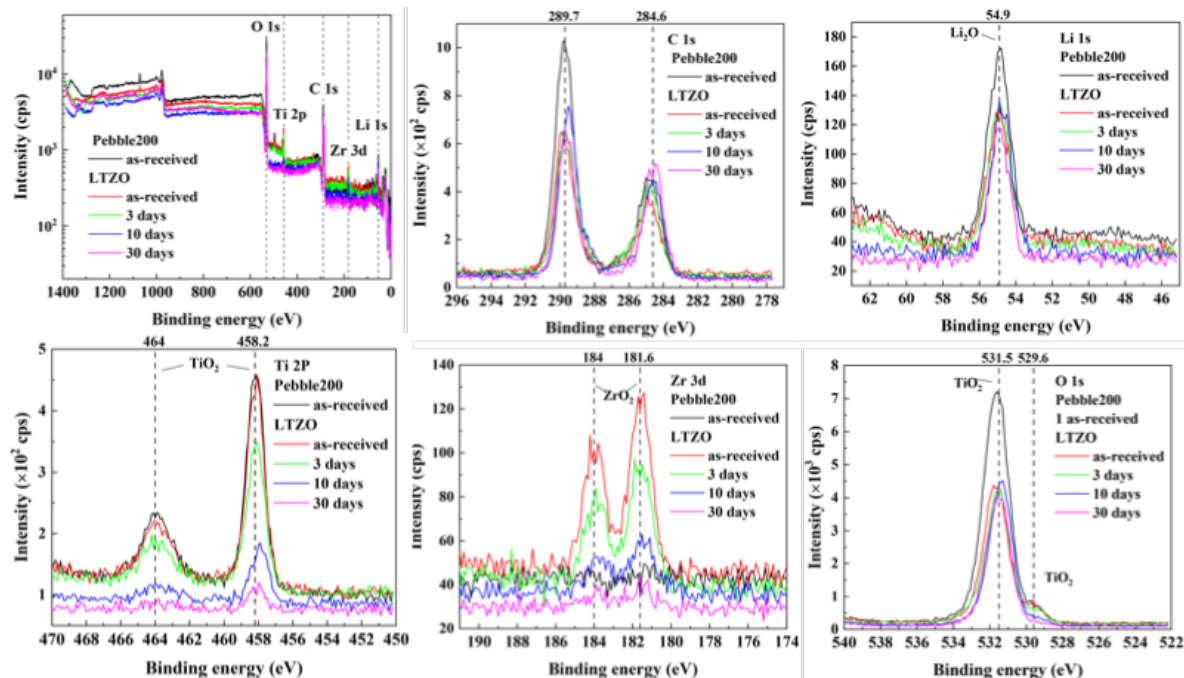

Figure 4.6. XPS signals with background signals, showing (top left) overall, (top center) C 1s, (top right) Li 1s, (bottom left) Ti 2p, (bottom center) Zr 3d, and (bottom right) O 1s orbits.

4.3.2 XRD

As seen in Figure 4.7, the XRD analysis (SmartLab SE, Rigaku Co.) indicated that the long-term heating of up to 30 days did not significantly alter the structure of the LTZO. All samples had nearly the same patterns as the reference [16] and no Li_2ZrO_3 [17] and LiOH [18]. In other words, the heated LTZO samples under H_2 retained the shape of the β-Li_2TiO_3 monoclinic crystal system, as in stacking the Li6, O6, and Li2Ti/Zr4 layers with the cations occupying the octahedral sites surrounded by O. Consequently, XRD analysis never observed noticeable structural changes in the long-term heated samples.
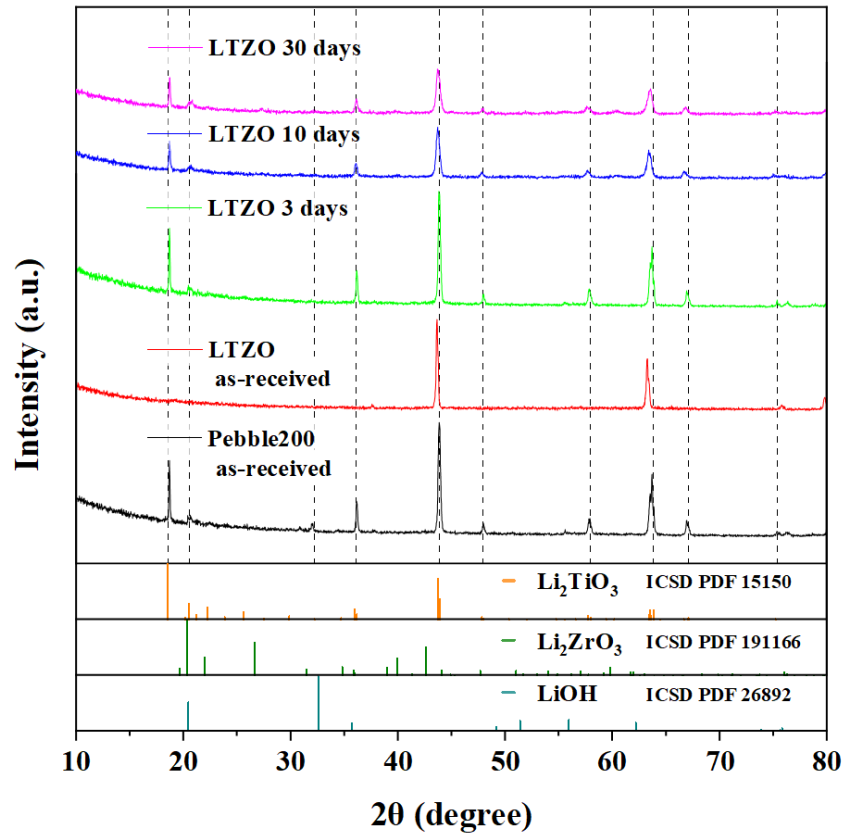

Figure 4.7. XRD spectrum from the LTZO in red, the Pebble200 in black, and the reference in orange.

4.3.3 SEM-EDX

Figure 4.8 presents representative SEM images of the internal structure of each heated sample and Pebble210 [15]. In these pictures, the grain boundaries appear less distinct than the as-received pebble, and surface roughness increases visually. This is likely because of the LiOH left on the grain surfaces.

A previous report [15] indicated the likelihood that some of the generated LiOH still adhered to the grain boundary, and they likely contribute to grain growth by acting as a binder between neighboring grains. Additionally, it proposed the grain growth model induced by the adhesive LiOH with the grain diameter, D [m], and grain growth rate, k_g [m s^{-1}].

$$\mathrm{d}D / \mathrm{d}t = k_g (Y - Y_s). \tag{4.4}$$

$$D = D_0 + k_g (Y_s - 1) \, e^{-kt} / k. \tag{4.5}$$

ImageJ proved that the average grain diameters of the heated samples were almost the same as the as-received pebbles, 3.3 μm. Therefore, this numerical model was inapplicable to LTZO because the difference in the grain diameter was too small to return the reliable fitting parameter, k_g. On the other hand, the LTZO had resistance to the grain growth. This is mainly because ZrO_2 prevented Li_2TiO_3 grain growth and partly because the generated LiOH quickly left the grain due to the low activation energy for Li mass loss.

Moreover, the sample heated for 30 days at 1173 K slightly differed in the EDX intensity ratio of Ti, Zr, and O compared with the as-received LTZO samples. Consequently, it is concluded that SEM-EDX showed little difference in the grain size and element intensities, except for their appearance.
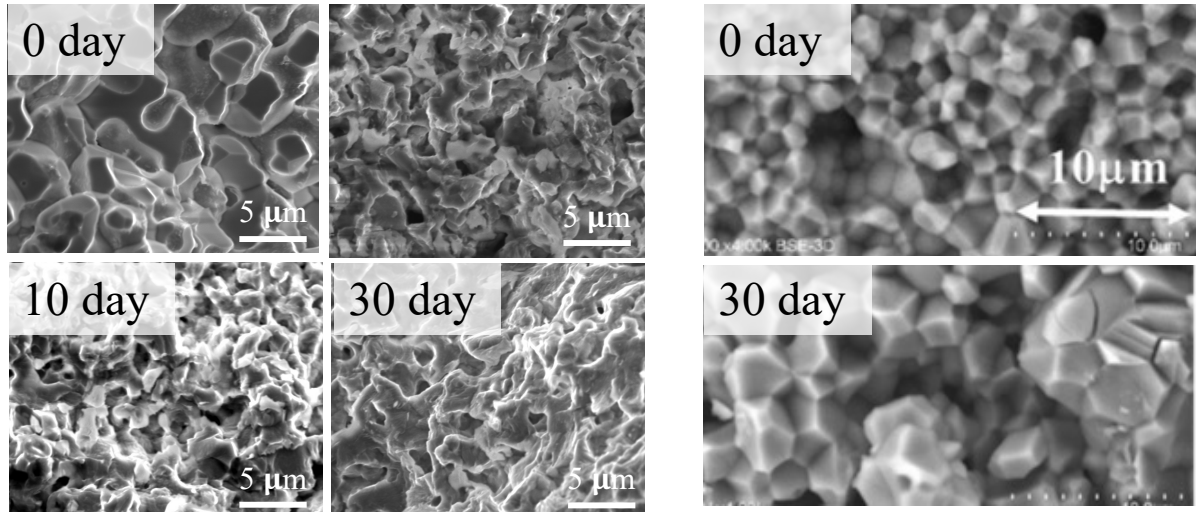

Figure 4.8. Representative SEM images of the inside of LTZO pebbles (left) and Pebble210 [15] (right).
LTZO heated (top left) for 0 days, (top right) for 3 days,
(bottom left) for 10 days, and (bottom right) for 30 days.
Pebble210 heated (top) for 0 days and (bottom) for 30 days.

4.3.4 Surface Area and Porosity Analysis

The surface analysis (TriStar II 3020, SHIMADZU Co.) was carried out multiple times with 0.5 g of the heated samples. Figure 4.9 delivers each of the averaged data. The sample loads were insufficient, so the device returned the data without reliability and duplicability, especially for the 10-day heated sample, which went negative. A tendency was found that heating generally raised the samples' porosity and BET-specific surface area. It was contradictory to the expectation that the grain growth and the surface energy optimization lessen porosity and surface area. Because noticeable grain growth was never confirmed, as mentioned in section 4.3.3, these data were deemed uncredible due to the possible inclusion of enormous measurement errors. Alternatively, it might be inferred that the porosity escalated with the length of heating. Therefore, it is never used for further discussion, and it concluded that heating LTZO for long does not cause significant changes in its surface area and porosity for now.
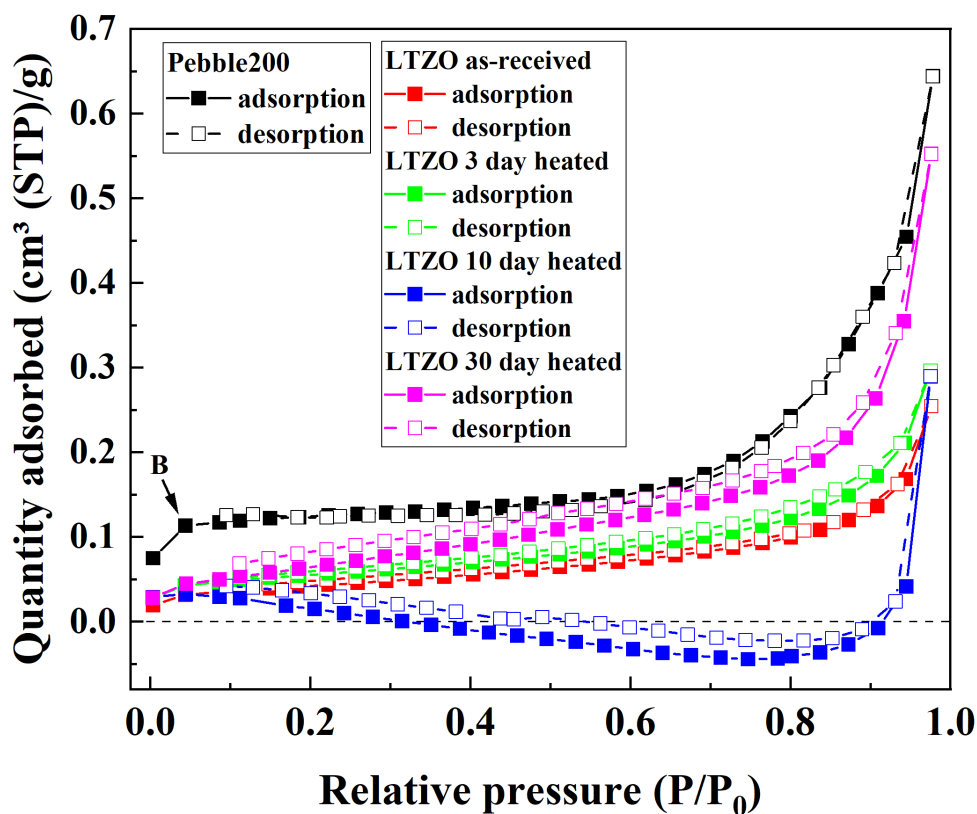

Figure 4.9. Adsorption/desorption isotherm of LTZO and Pebble200.

4.4 1D Simulation

This 1D simulation aims to forecast Li evaporation amount over a specific time frame and evaluate its impact on the tritium fuel cycle, particularly on the tritium production rate and TBR. This simulation is based on the experimentally obtained Li mass loss rate given by equation (4.3).

4.4.1 Simulation Methodology

Using simple mathematics, a 1D simulation assessed the relationship between Li burn-up and Li mass loss. In general, the Li burn-up rate is obtained based on the definition of TBR.

$$Li_{\text{burn-up }(t)} = T_{\text{consump}} \; TBR_{\text{eff }(t)} \; M_{\text{Li}} / N_{\text{A}}, \tag{4.6}$$

$$T_{\text{consump}} = P_{\text{th}} / H, \tag{4.7}$$

$$TBR_{\text{eff }(t)} = TBR_{\text{local}} \; \beta_{\text{vv}} \; N_{\text{Li }(t)}, \tag{4.8}$$

where $Li_{\text{burn-up}}$ [g s^{-1}] is the Li burn-up rate due to the nuclear reaction with the neutrons, T_{consump} [s^{-1}] is the tritium consumption rate due to the nuclear fusion reaction, P_{th} [W] is the target fusion thermal output of the plant, H [J] is the nuclear fusion reaction energy output, M_{Li} [g mol^{-1}] is the atomic weight of Li, N_{A} [mol^{-1}] is the Avogadro's number, TBR_{eff} and TBR_{local} [-] are effective and local TBR at the breeding blanket, respectively, and β_{vv} [-] is the effective coverage of the vacuum vessel for the breeding blanket. Given the Li depletion over operation time due to the Li burn-up and evaporation, the effective TBR keeps decreasing over time according to the normalized Li content by the initial value, N_{Li} [-]. M_{Li} is tailored to the ^{6}Li enrichment ratio, $R_{6\text{Li}}$ [-], as follows:

$$M_{\text{Li}} = 6R_{6\text{Li}} + 7(1 - R_{6\text{Li}}). \tag{4.9}$$

The amount of Li burn-up highly depends on the abundance of ^{6}Li, whose neutron cross-section is far higher than one of ^{7}Li. Summating each element's atomic weight according to the stoichiometric ratio presents the atomic mass of the specific tritium breeding material. Equation (4.3) can express the Li mass loss rate in s^{-1}. Hence, normalizing the Li burn-up rate, as in equation (4.6), by the initial loads of tritium breeding material enables discussion of the relationship between Li burn-up and Li mass loss.

Then, this work carried out a 1D simulation specifically using the JA-DEMO blanket design [19], a relatively more accessible geometry than the latest cylindrical water-cooled ceramic-breeder blanket geometry [2-4]. Figure 4.10 elaborates on the calculation geometry. The temperature distribution between the cooling piping was set parabolically, considering the current design of the water coolant outlet temperature [1, 2, 19] and the allowable maximum temperature in the breeding blanket module [2, 3].

$$T_{(x)} = - 0.92x^2 + 46x + 598, \tag{4.10}$$

where $T_{(x)}$ [K] is the temperature at position x and x [mm] is the position from 0 to 50 mm from the left coolant pipe. This temperature function was substituted into the experimentally obtained Li mass loss rate function expressed by equation (4.3). P_{H2O} was set at a constant value all over the calculation region to keep it simple.
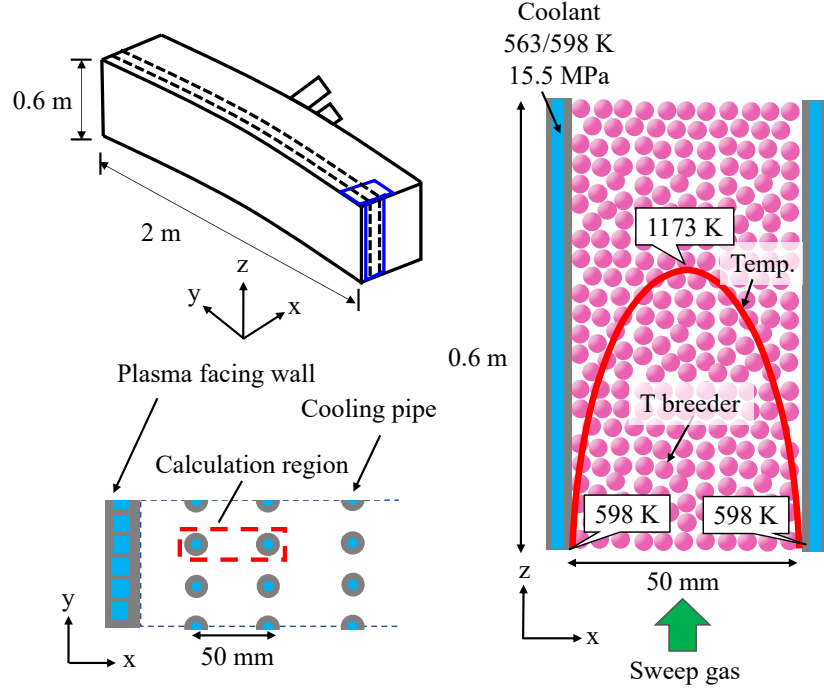
Figure 4.10. Schematic of the blanket geometry.

(Top Left) the blanket geometry that this work employed [19].

(Bottom Left) The X-Y profile of the blanket module shows the calculation region

enclosed by the broken red line.

(Right) The blanket module's X-Z profile performs 1D calculation along the x direction.

Table 4.1 lists all parameters required for this simulation, including reasonable estimates. The Li burn-up rate, $Li_{burn-up}$, is calculated as 5.0×10^2 g day^{-1} by equation (4.6). Since JA-DEMO has not explicitly fixed the loads of tritium breeding material yet, this work varied the loads of the tritium breeder from 50 to 1000 tons. LTZO, $Li_{2.15}Ti_{0.8}Zr_{0.2}O_{3.075}$, was selected as the tritium breeding material. Its molar mass gave the Li loads. The plant availability was simplified to 100%.

Table 4.1. Parameters used in this calculation.

Symbol/Term	Value	Unit	Ref.
P_{th}	1.5	[GW]	[4]
H	17.6	[MeV]	
TBR_{local}	1.41	[-]	[18]
β_{VV}	0.759	[-]	[20]
R_{6Li}	0.9	[-]	[19]
LTZO loads	50, 100, 500, 1000	[ton]	
Li loads	6.17, 12.3, 61.7, 123	[ton]	

4.4.2 Results and Discussion

Figure 4.11 illustrates that the LTZO is prone to rapidly lose Li when in contact with sweep gas that contains even a trace amount of water vapor as low as 1 Pa. Almost all of them would evaporate within three months. Because of its small temperature dependence, as shown in Figure 4.5, the LTZO would decrease Li density even at the position right close to the water coolant piping. This indicated that the benefits of the additional Li would be limited. The rate of the lost Li throughout the computational domain at 1 Pa water vapor, Li_{evap} [day^{-1}], was mathematically represented as follows:

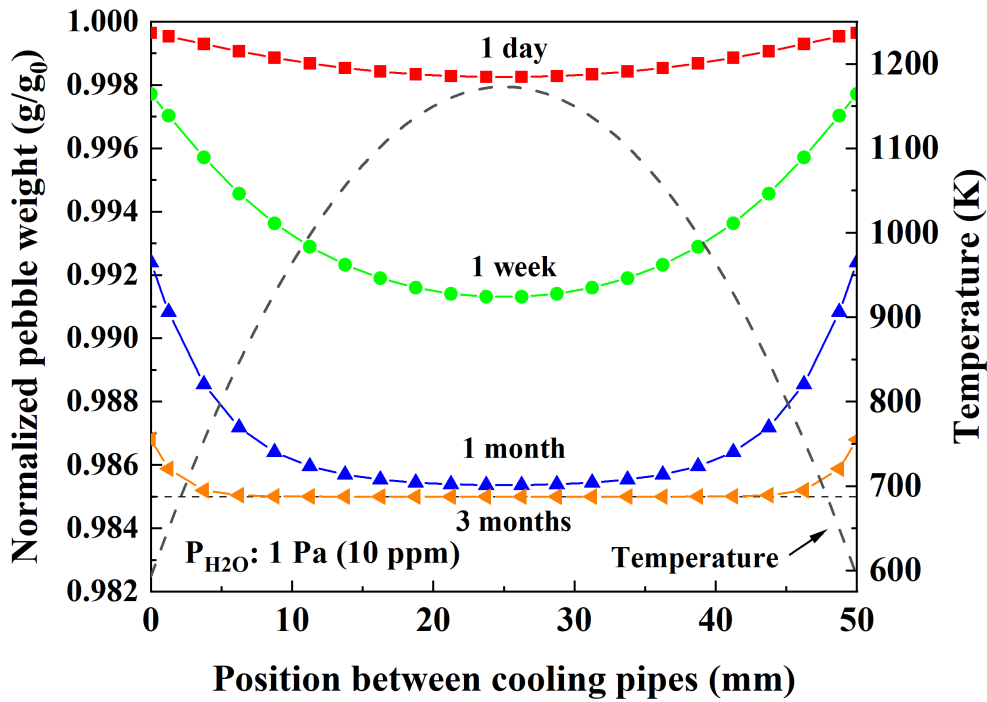$$Li_{evap} = 0.015 \, (1 - \exp(-0.0877 \, t)). \tag{4.11}$$

Figure 4.11. Li mass loss under 1 Pa H_2O condition, varying operation time.

The absolute Li evaporation amount will be 1.5 wt% of the loads of the LTZO. Therefore, it is suggested that the tritium breeders with different Li densities are strategically distributed following the blanket temperature distribution as the practice that pressurized water fission reactors do. It helps mitigate excessive LiOH gas formation and potential accident risks, for instance, a loss of coolant accident (LOCA).

Figure 4.12 emphasizes that the Li loss rate correlates directly with the water vapor concentration in the surrounding environment. Therefore, the water vapor concentration control is essential for limiting Li mass loss. As mentioned, keeping the water vapor partial pressure below 1 Pa should be practically challenging with commonly used adsorbents. As seen in Figure 3.7, water vapor is expected to be released from the breeder pebbles at around 593 and 773 K. Moreover, as seen in Figure 3.8, an H_2-containing sweep gas further promotes water vapor formation by interacting with TiO_2 and ZrO_2 in high-temperature regions, especially during the initial operational phases. Water vapor is also likely to desorb from the surrounding structural materials. Hence, it is advisable to preheat the tritium breeding bed thoroughly in advance to minimize the detrimental impact of water vapor on Li evaporation and to maximize the benefits of Li addition for tritium production.
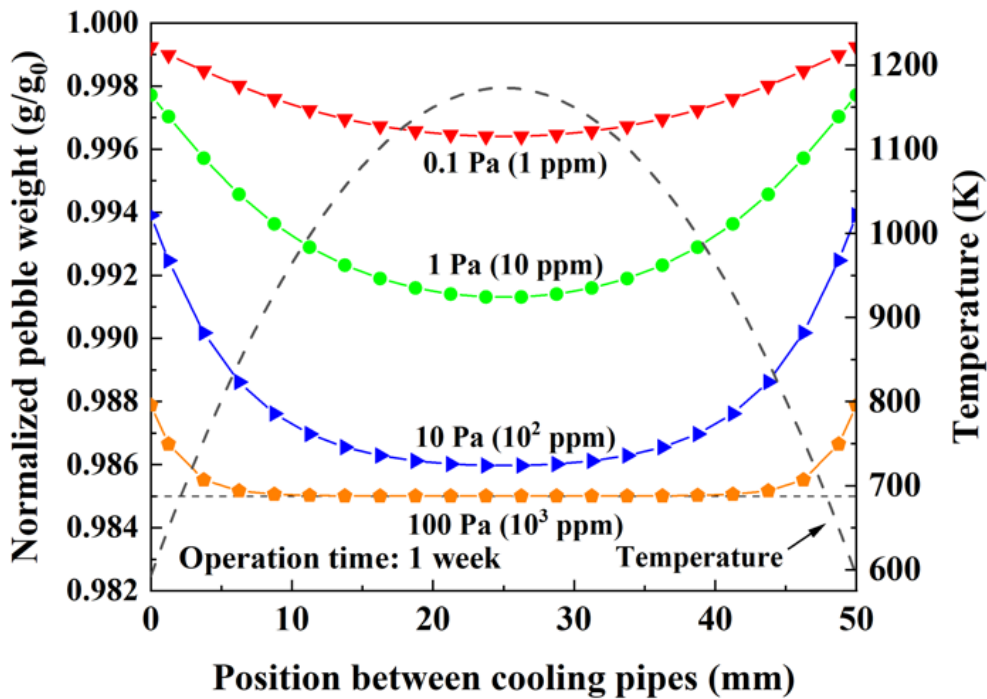

Figure 4.12. Li mass loss in 1 week, varying the vapor concentration.

Figure 4.13 displays the effect of Li evaporation on tritium production by varying the LTZO loads during the first two years of practical blanket use. The Li mass loss rate represented in black was drawn using equation (4.11). Consequently, it was observed that the overall negative impact of Li evaporation on tritium production was limited because Li mass loss will cease at 1.5 wt% reduction. However, it should be noted that the Li mass loss was more overriding than the Li burn-up in the first four months.

Considering the current design [21], which says 100 tons of Li_2TiO_3 pebbles are expected to be loaded, and Li_2ZrO_3 blanket [22], which says 70 tons of Li is required for 3 GW fusion thermal output, a practical Li burn-up rate can be extrapolated between the green and blue lines. This is presumably because excess Li, equivalent to more than 90% of the total, can guarantee high TBR and tritium production even in the late operation phase. They will then be reprocessed and loaded into the next breeding blanket module.

Figure 4.13 illustrates the change in the TBR over time. The TBR declines with the Li content, as in equation (4.8), resulting from the Li mass loss and Li burn-up. At the initial stages of operation, Li mass loss would severely affect the TBR. However, the adverse effects on the TBR were also limited in the long run. Given the anticipated loading of the tritium breeding material [21, 22], the net TBR would decrease by just a few percent of the initial design value of the TBR.
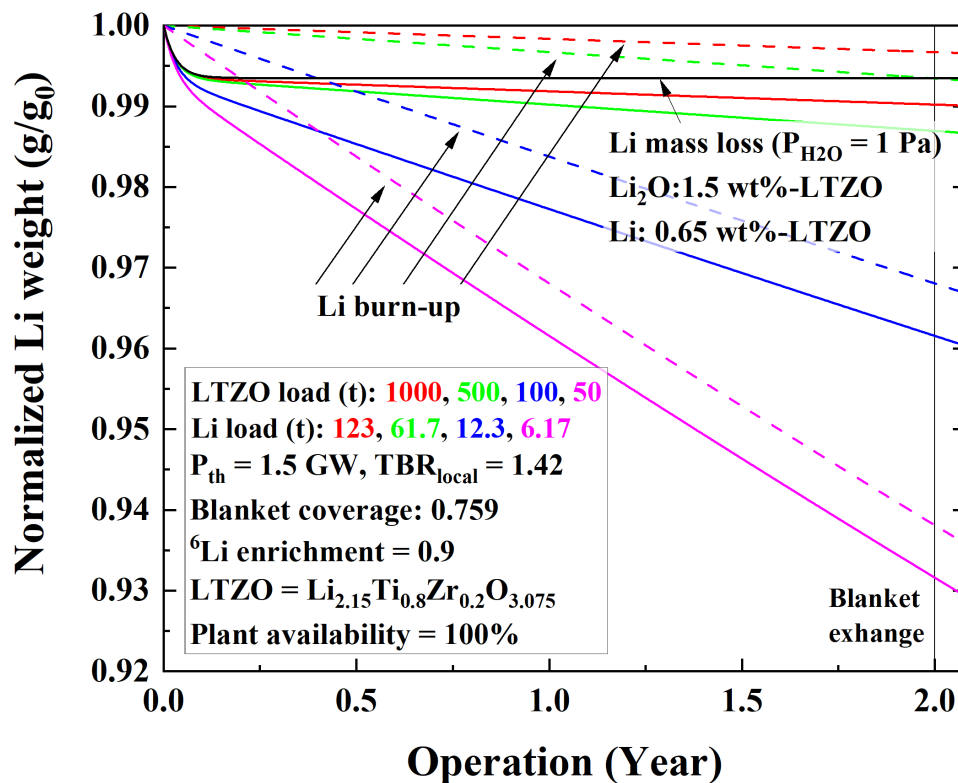

Figure 4.13. Comparison between Li mass loss and Li burn-up amounts.

4.5 Summary

Chapter 4 delves into the Li mass loss behavior from the fusion engineering aspects. A comprehensive compilation of the principal discoveries derived from experimental observations and computational simulations is presented here.

Key Findings:

1. **Li Mass Loss Behavior**: Li loss in LTZO pebbles occurred exponentially through the chemical interaction of Li_2O, which was likely energetically unstable, with the water vapor in the gas phase. It is represented by $Y = 0.985 + 0.015 \exp(- 0.029 P_{H2O}^{1/2} \exp(-16839 / RT) t)$. Temperature and vapor concentration influenced the Li mass loss behavior until 1.5 wt% of LTZO depletion.

2. **Corrosion Concerns**: Li mass loss behavior created a LiOH corrosive layer on the wall. In addition, the sweep gas carries the gaseous LiOH further. They indicate a potential risk of the mechanical soundness to adjacent structures and downstream piping.

3. **Structural Changes**: In the case of LTZO, the long-term heating at 1173 K under H_2 purging conditions did not significantly change composition, crystal structure, and grain diameter. The ZrO_2 and quick desorption of the generated LiOH prohibited the LTZO from grain growth.

4. **Li Loss in the Blanket**: Li was rapidly desorbed from the LTZO in a fusion environment, so the benefits of the additional Li were limited.

5. **Effects on Tritium Production**: The 1.5 wt% Li depletion did not profoundly affect tritium production, but its amount exceeded the tritium production during the first few months.

References

[1]   Y. Someya et al., Fusion Eng. Des., 146, (2019), 894-897, doi: 10.1016/j.fusengdes.2019.01.107.

[2]   Y. Kawamura et al., Fusion Eng. Des., 161, (2020), 112050, doi: 10.1016/j.fusengdes.2020.112050.

[3]   Y. Ishi et al., Fusion Sci. Technol., 77, (2021), 532–548, doi: 10.1080/15361055.2021.1925030.

[4]   T. Hernández et al., Nucl. Mater. Energy, 15, (2018), 110-114, doi: 10.1016/j.nme.2018.03.005.

[5]   K. Mukai et al., Nucl. Mater. Energy, 15, (2018), 190-194, doi: 10.1016/j.nme.2018.04.010.

[6]   N. Takahashi et al., Plasma Fusion Res., 16, (2021), 2405032, doi: 10.1585/pfr.16.2405032.

[7]   H. Masaki et al., Plasma Fusion Res., 17, (2022), 1405075, doi: 10.1585/pfr.17.1405075.

[8]   E. Gaisina et al., J. Nucl. Mater., 564, (2022), 153677, doi: 10.1016/j.jnucmat.2022.153677.

[9]   C. Wagn et al., Ceram. Int., 49, (2023), 17851-17858, doi: 10.1016/j.ceramint.2023.02.151.

[10] K. L. Wrisley et al., Fusion Eng. Des., 13, (1990), 45-42, doi: 10.1016/0920-3796(90)90031-Z.

[11] D. J. Duquette et al., J. Nucl. Mater., 191-194, (1992), 992-996, doi: 10.1016/0022-3115(92)90623-S.

[12] J. H. Zheng et al., Corrosion, 49, (1993), 372-376, doi: 10.5006/1.3316062.

[13] LTS Research Laboratories, Inc., Safety Data Sheet, Lithium hydroxide. Retrieved November 22, 2023, from https://www.ltschem.com/msds/LiOH.pdf.

[14] K. Mukai et al., Int. J. Hydrog, Energy, 47, (2022), 6154-6163, doi: 10.1016/j.ijhydene.2021.11.225.

[15] A. Ipponsugi et al., Nucl. Mater. Energy, 25, (2020), 100777, doi: 10.1016/j.nme.2020.100777.

[16] J. F. Dorrian et al., Mater. Res. Bull, 4, (1969), 179–184, doi: 10.1016/0025-5408(69)90054-3.

[17] Y. V. Baklanova et al., J. Solid State Chem., 298, (2013), 43-49, doi: 10.1016/j.jssc.2013.09.030.

[18] T. Ernst, "Darstellung und Kristallstruktur von Lithiumhydroxyd," Zeitschrift für Physikalische Chemie, Abteilung B: Chemie der Elementarprozesse, Aufbau der Materie, 20, (1993), 65-88.

[19] Y. Someya et al., Plasma Fusion Res., 6, (2011), 2405108, doi: 10.1585/pfr.6.2405108.

[20] H. Utoh et al., Plasma Fusion Res., 6, (2011), 2405053, doi: 10.1585/pfr.6.2405053.

[21] S. Konishi et al., Nucl. Fusion, 57, (2017), 092014, doi: 10.1088/1741-4326/aa7e4e.

[22] M. Nishikawa et al., J. Nucl. Mater., 257, (1998), 162-171, doi: 10.1016/S0022-3115(98)00439-5.

Chapter 5. Tritium Release Behavior

Outline

This chapter pursues the tritium release behavior. First, the background and aim of this work are briefly explained. Next, the neutron irradiation procedure is carefully given. Then, the tritium release behavior is discussed, considering the tritium mass balance between the theoretical and experimental values. Finally, a summary of the results of this chapter is presented.

5.1 Introduction

The current JA-DEMO design employs the Li_2TiO_3 ceramic pebbles as the tritium breeding material [1, 2]. A new promising Li_2TiO_3-based material, LTZO, has been developed by QST. Its tritium release mechanisms have yet to be carefully studied. Moreover, it has yet to be clarified that the structural changes induced by long-term usage in a harsh environment cause any difference in tritium release properties. From the viewpoint of the feasibility of the tritium fuel cycle, it is essential to investigate the tritium release behavior experimentally from the as-received and long-term heated LTZO pebbles to contribute to designing the blanket system. To achieve the goals, this chapter aims to conduct experiments to clarify thoroughly its nuclear characteristics and tritium release behavior.

5.2 Neutron Irradiation

This section aims to clarify the nuclear characteristics of the LTZO pebbles, including the decay products and daughter products of LTZO.

5.2.1 Sample Preparation

Due to regulations regarding tritium, the amount of tritium that can be handled at the laboratory is limited to approximately 10^6 Bq. Therefore, minimizing the vapor concentration surrounding the irradiation samples is vital since even a trace amount of water vapor, 1 Pa, is detrimental to this limited tritium amount. Additionally, given the blanket temperature distribution [1, 2], tritium release behavior from 573 to 1173 K is important. Therefore, all the irradiation samples were heated at 573 K in advance under 1×10^5 Pa Ar gas until the completion of water vapor desorption from the samples using the device, as shown in Figure 4.1. Then, a quartz tube sealed at one end was filled with the samples. The other end was connected to a rotary pump to establish a vacuum environment within the tube. Usually, a rotary pump can evacuate up to 10^{-2} Pa. This end was subsequently sealed using a gas burner to maintain the vacuum state.

5.2.2 Neutron Irradiation

All the samples were carried to Kyoto University Research Reactor (KUR) for neutron irradiation tests. KUR transmits samples to the reactor core by pressurized CO_2. Therefore, each sample was cushioned with layers of absorbent cotton to protect the fragile quartz tubes from any damage that might allow produced tritium to leak outside. Then, they were housed within an exclusive polyethylene container that KUR provided. Figure 5.1 shows the fuel assembly of KUR. Pressurized CO_2 pneumatically transfers the sample to Pn-2, which experiences the highest neutron flux among all the pneumatic transportation tubes. Graphite rods surround the transmission tube to reflect the fission neutrons well. As a result, the LTZO samples were exposed to predominantly thermal neutrons at Pn-2 for a specific time, 1 or 5 minutes. The fission thermal output of KUR was carefully controlled to 5 MW, and the sample transportation piping tube was cooled at less than 323 K.

Figure 5.1. Schematic diagram of the fuel assembly in KUR [3].
F, G, and Pn denote the fuel, graphite, and pneumatic transmission tubes.

The composition of LTZO pebbles includes elements capable of absorbing thermal neutrons and undergoing a transmutation process, except for ^6Li. The radioactivity produced by each nuclear reaction is obtained theoretically by combining equations (2.11), (2.12), and (2.16) using the index, i.

$$A_i = \sigma_i N_i \phi \left(1 - e^{-\lambda_i t_1}\right) e^{-\lambda_i t_2}, \tag{5.1}$$

where A [Bq] is the produced radioactivity, σ [m^{-2}] is the neutron capture cross-section of the reactant, N [-] is the number of the reactant atoms, ϕ [cm^{-2} s^{-1}] is the thermal neutron flux, λ [s^{-1}] is the decay constant of the product, and t_1 and t_2 [s] are the irradiation time and cooling time, respectively. The neutron cross-section and the decay constant were based on a nuclear database, JENDL-5 [4]. The molar mass of the LTZO, $Li_{2.15}Ti_{0.8}Zr_{0.2}O_{3.075}$, gave the number of the reactant atoms N_i. Each sample had roughly 0.5g LTZO pebbles.

Table 5.1 and Table 5.2 summarize the neutron irradiation conditions and radioactivity of the produced nuclei right after the 5-minute neutron irradiation. The gaseous species, except tritium, promptly decay due to their short half-life. Therefore, they do not affect the following tritium release experiment. Also, as seen in Table 5.2, ^{7}Li does not contribute to tritium production, as in equation (1.3), because of its low cross-section to thermal neutron compared with ^{6}Li [5]. Thus, this work only focuses on the contribution from ^{6}Li, as in equation (1.2). It should be noted that the ^{93}Zr atom that emits gamma rays has a long half-life. This is a massive drawback regarding the nuclear characteristics of the LTZO. During the operation, LTZO pebbles generate gaseous species (e.g., ^{3}He, ^{4}He, and ^{19}F) and metal species (e.g., ^{51}V, ^{93}Nb, ^{95}Mo, and ^{97}Mo).

Table 5.1. Neutron irradiation conditions.

Symbol	Value		Unit	Ref.
	As-received LTZO	Heated LTZO (3, 10, 30 days)		
Φ	2.75×10^{13}		[cm^2 s^{-1}]	[6]
t_1	1	5	[min]	
t_2	54	47	[day]	

Table 5.2. Radioactivity of the produced nuclei right after the 5-minute neutron irradiation.

| Nuclear reaction	Activity (Bq g^{-1})	Decay	Half-life [4]		Cross-section [4] (×10^{-24} cm^2)
			Value	Unit	
^{6}Li (n, α)T	1.30×10^7	beta	12.32	year	9.40×10^2
^{7}Li (n, γ)^{8}Li	1.21×10^{10}	beta	0.838	second	4.50×10^{-2}
^{18}O (n, γ)^{19}O	1.20×10^5	beta/gamma	26.88	second	1.60×10^{-4}
^{50}Ti (n, γ)^{51}Ti	4.60×10^8	beta/gamma	5.76	minute	1.79×10^{-1}
^{92}Zr (n, γ)^{93}Zr	4.38×10^{-5}	beta	1.61×10^6	year	2.29×10^{-1}
^{94}Zr (n, γ)^{95}Zr	8.83×10^3	beta/gamma	64.03	day	5.07×10^{-2}
^{96}Zr (n, γ)^{97}Zr	5.11×10^4	beta/gamma	16.75	hour	2.03×10^{-2}
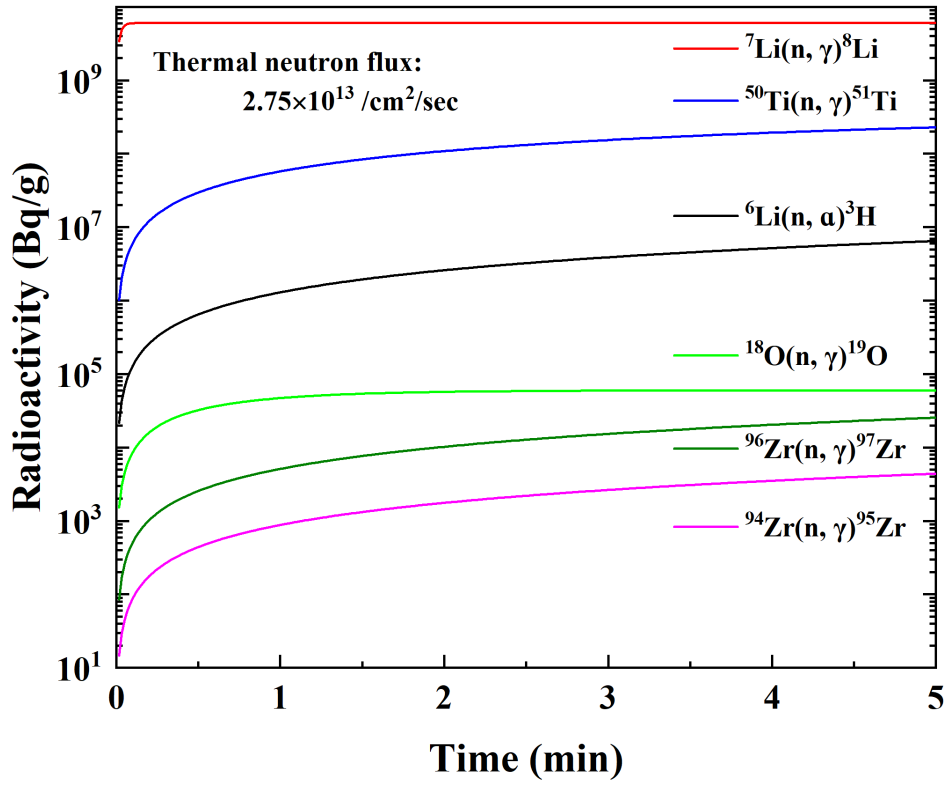
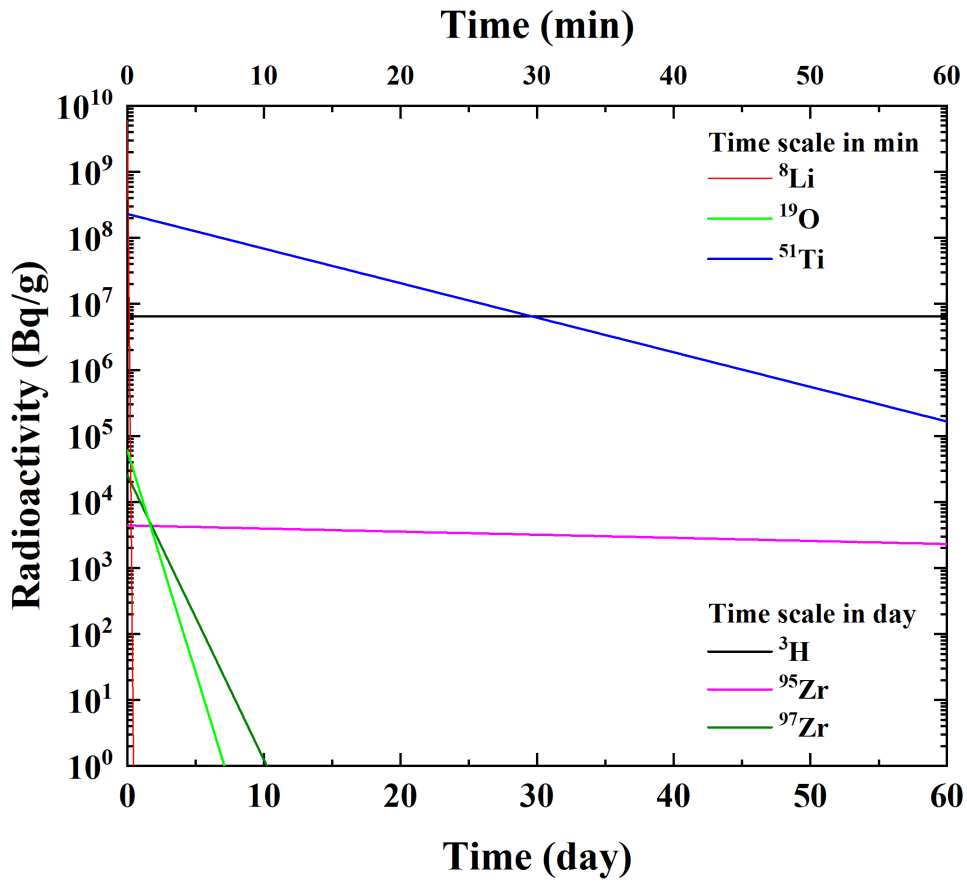Figure 5.2. Produced radioactivities over the irradiation time.

Figure 5.3. Declining in the produced radioactivities over the cooling time.

5.3 Tritium Release Experiment

This section aims to elucidate the tritium release behavior from the as-received LTZO pebbles and identify the long-term heating effects on the tritium release behavior.

5.3.1 Experimental Procedure

All the samples were transported to the laboratory after the specific cooling time at KUR. The decay of tritium until each experimental date was negligible. Figure 5.4 illustrates the experimental setup for the post-irradiation experiment (PIE). The irradiated pebbles were removed from the tube in a glove box filled with Ar gas, placed in a quartz tube, and centered with quartz wool on both ends.

The experimental procedure was divided into four parts. Firstly, 1×10^5 Pa Ar gas purged each sample to remove the physisorption. Secondly, it was heated from room temperature to 1173 K at the rate of 5 K min^{-1} and kept heated until the tritium release stopped. During the heating process, the purge gas species were chosen from 1×10^5 Pa Ar, 1×10^3 Pa H$_2$/Ar, or 1×10^3 Pa H$_2$O/Ar gas. The total pressure was maintained at the atmospheric level with a controlled flow rate of 100 mL min^{-1}. H$_2$O gas was generated through a Pt catalyst, supplying 1×10^3 Pa H$_2$/Ar with 80 mL min^{-1} and 4×10^4 Pa O$_2$/Ar with 20 mL min^{-1}. As a result, H$_2$O gas contained the residual O$_2$ gas. Subsequently, 1×10^3 Pa H$_2$O/Ar thoroughly cleansed the experimental device except for the sample bed. Due to its polarity, HTO adheres to the piping, resulting in what is known as the system effect [7], and is one of the factors contributing to inaccurate measurement. Finally, 1×10^3 Pa H$_2$O/Ar expelled the tritium from the sample bed to eliminate the unrecovered tritium due to the purging gas species and the system effect.
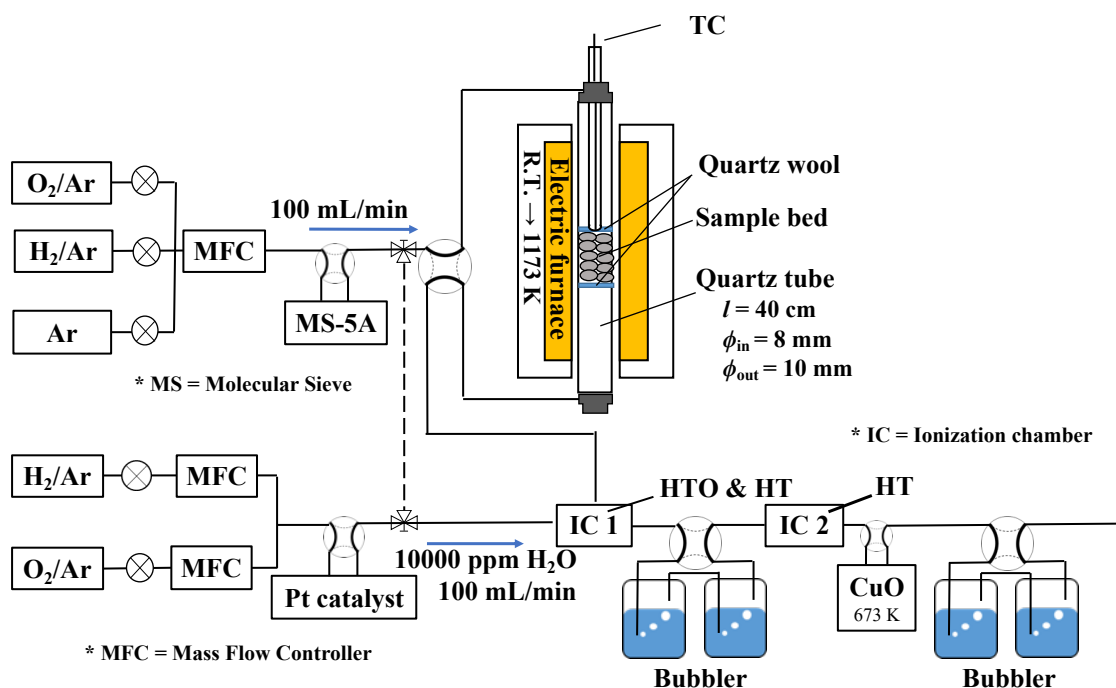

Figure 5.4. Experimental apparatus for the tritium release experiment.

As mentioned in section 2.7, isotope reactions, as in equations (2.22) and (2.23), determine the tritium chemical form, HT or HTO. The two ionization chambers (IC) applied 90 V continuously monitored the tritium desorption spectrum. Besides, two sets of bubblers filled with 150 mL of distilled water were installed right after each IC to collect the released tritium. While HTO gas is quickly swapped by hydrogen in the first bubblers, HT gas hardly dissolves into water and interacts with hydrogen in the bubblers. Therefore, the CuO bed heated at 673 K converted HT to HTO to collect HT gas. Installing two bubbler sets and the CuO bed enabled two ICs to observe tritium based on its chemical form. HTO easily adheres to the electrodes of the ICs and amplifies the signal, a phenomenon known as the memory effect [8]. Therefore, H_2O gas with 100 mL min^{-1} was introduced to ICs to continuously assist in swapping the adsorbed tritium atom and suppress the background signal fluctuation. In a few words, 200 mL min^{-1} gas was constantly delivered to the ICs. Figure 5.5 presents the tritium release spectrum according to the experimental procedure.
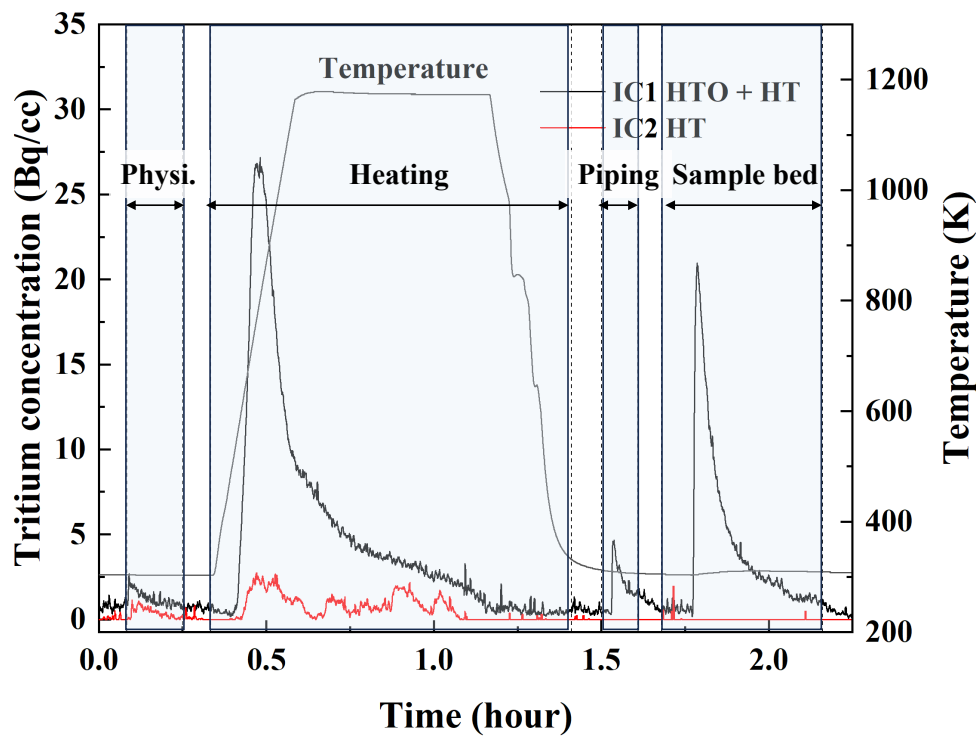

Figure 5.5. An example of tritium release spectrum purged with Ar gas.

After each purging process, the tritium collected in two scrubbers was quantified with a liquid scintillation counter (LSC) (LSC-5100, ALOKA) to verify the IC response. Each IC underwent calibration using tritium-containing gas and LSC. Appendix A carefully conveys the calibration procedure.

Finally, about 0.02 g of the heated sample was immersed in 5 mL of 46% HF solution at room temperature to see if tritium was still present, for instance, at trapping sites. The top lid was sealed with Teflon tape. The sample was decomposed completely in a few days. As Figure 5.6 illustrates, a diaphragm pump evacuated gaseous tritium and carried it to the bubblers filled with about 15 mL of distilled water. In parallel, 1×10^3 Pa H_2O/Ar was constantly introduced to the clove box to lower the system effect. The LSC measured the tritium dissolved in the acid solutions and collected in bubblers. Because a pH meter denied the existence of TF in the bubblers, each bubbler collected HT and HTO, respectively.
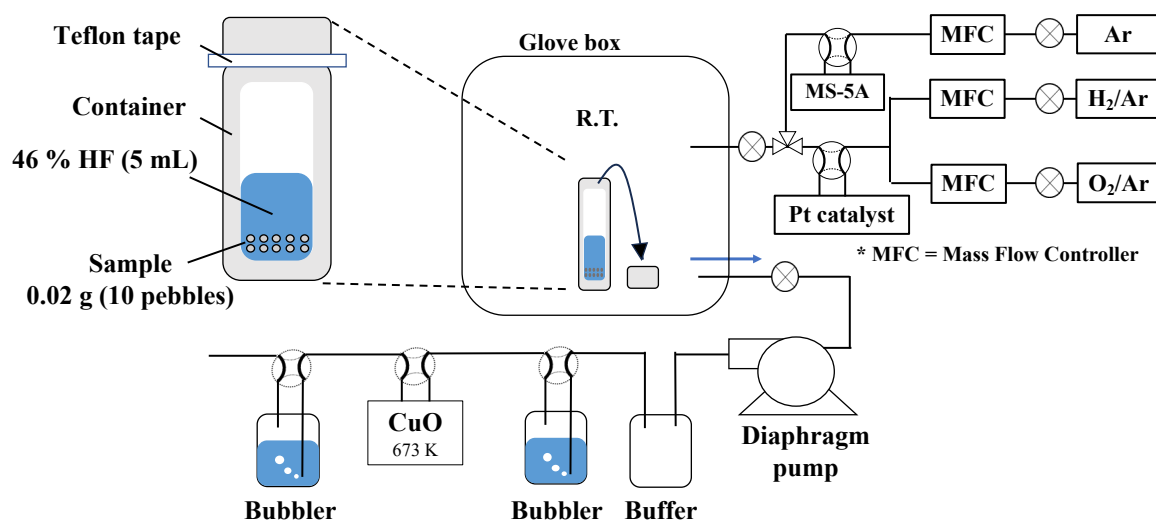

Figure 5.6. Experimental apparatus for the acid decomposition experiment.

5.3.2 Results and Discussion

Firstly, the tritium release behavior from the as-received samples was investigated. The most important thing is the tritium release behavior in the blanket temperature regions, roughly from 573 to 1173 K. Hence, Figures 5.7, 5.8, and 5.9 represent the tritium release curves when heating each under Ar, H_2O, and H_2 purging conditions, respectively.

Three samples had an HTO peak of around 600 K in common. This peak temperature nearly matched the chemisorption release, as seen in Figures 3.7 and 3.8. Based on the model introduced in section 2.7, the produced tritium diffused quickly inside the grain as the temperature rose from room temperature, interacting with the defects generated by the recoiled tritium. Then, it came into contact with the equilibrium water vapor. Although the sample was heated at 573 K in advance and stored under a vacuum, possibly as low as 10^{-2} Pa, until the experimental date, the quantity of adsorbed water vapor was still significant compared to the number of generated tritium atoms. Therefore, chemisorption release initiated the HTO release.

The peak temperature, height, and width of these HTO peaks differed slightly even though they came from the exact mechanism. While Ar and H_2 gas species merely resulted in chemisorption release around 600 K, H_2O gas species facilitated the isotope exchange reaction, as in equation (2.23), in addition to the chemisorption release. The effects of the chemisorption release and the isotope exchange reaction overlapped around 568 K. Consequently, the surface reaction between bred tritium and purge gas species determined the overall tritium migration rate from the bulk to the gas phase, as the previous work [9] reported. Otherwise, their appearance should be nearly alike. This is partly attributed to the grain size. As the grain size decreases, the diffusion path and the surface area for interaction become shorter and larger, respectively.

Ar gas purging detected only the peak from the chemisorption. The absence of hydrogen atoms resulted in no more tritium recovery. Even 1×10^3 Pa H_2O purge at the end found no noticeable peaks.
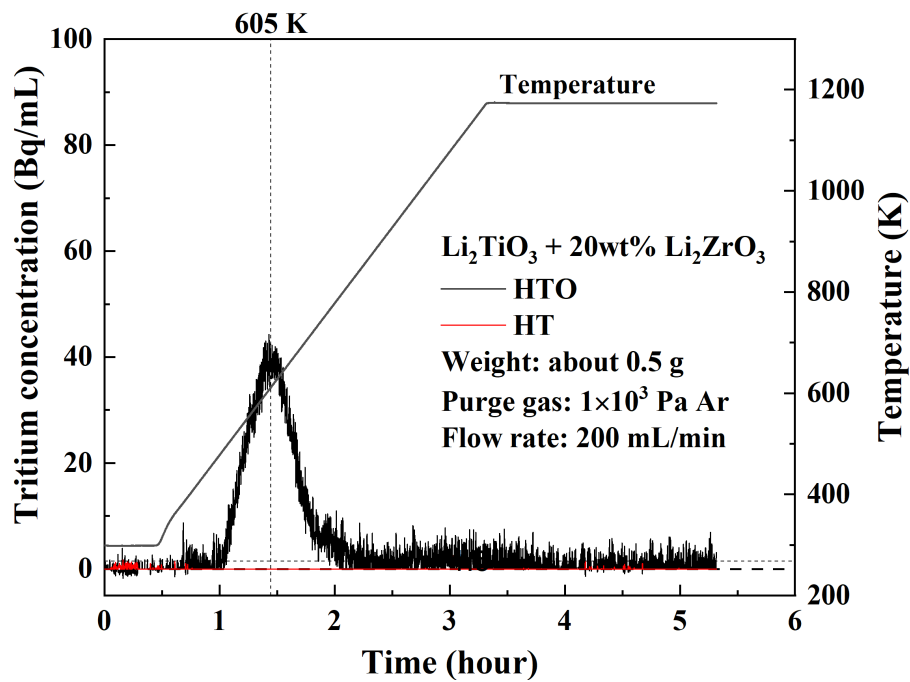

Figure 5.7. Tritium release spectrum when heating the LTZO under the Ar gas purging condition.

In the H_2O gas purging, the tritium release spectrum was deconvoluted into four peaks. It started releasing even as soon as the temperature rose. It peaked at 497 and 568 K, close to the peak temperatures of the chemisorption, as shown in Figures 3.7 and 3.8. Another HTO peak at 722 K was derived from the thermal decomposition of the LiOH. The other HTO peak at 927 K was derived from the isotope exchange reaction, as in equation (2.23). The isotope exchange rate with H_2O [10] is assumed to be constantly higher than the one with H_2 [11] in the blanket region. Therefore, the isotope exchange reaction with H_2O amplified the overall spectrum. The H_2O gas purging suppressed the tritium release as HT.
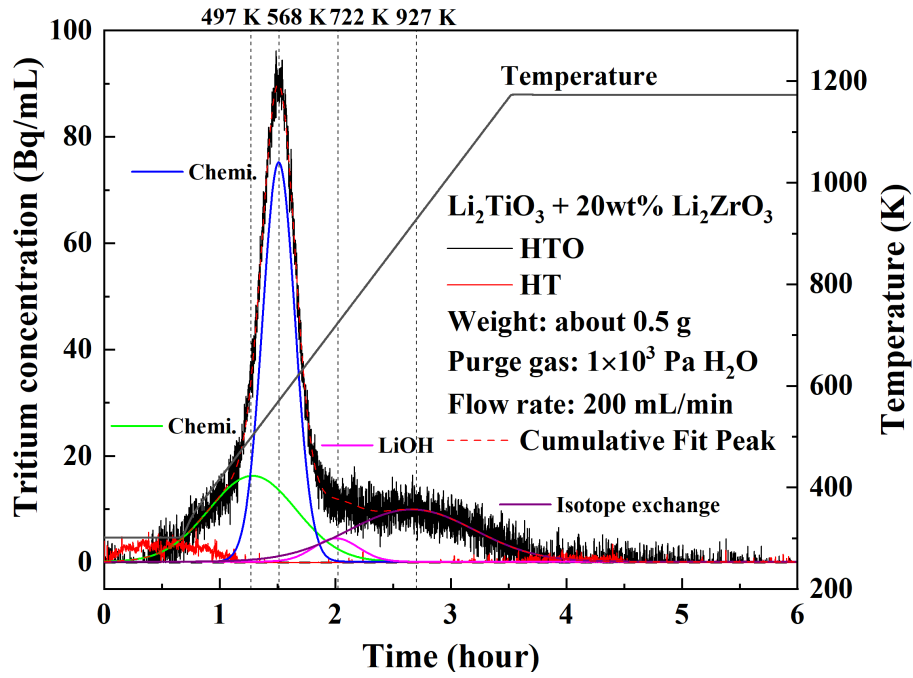
Figure 5.8. Tritium release spectrum when heating the LTZO under the H2O gas purging condition.

In the H2 gas purging, another prominent HTO peak was found at around 772 K. This temperature was caused by the LiOH thermal decomposition, as shown in Figures 3.7 and 3.8. Since the isotope reaction rate with H2 [11] soared following the temperature rise, partial tritium was recovered at around 837 K. It was experimentally found that the LTZO had the potential to competitively release HT over HTO, which is beneficial in reducing the workload of the tritium fuel system, as mentioned in section 1.2.2.
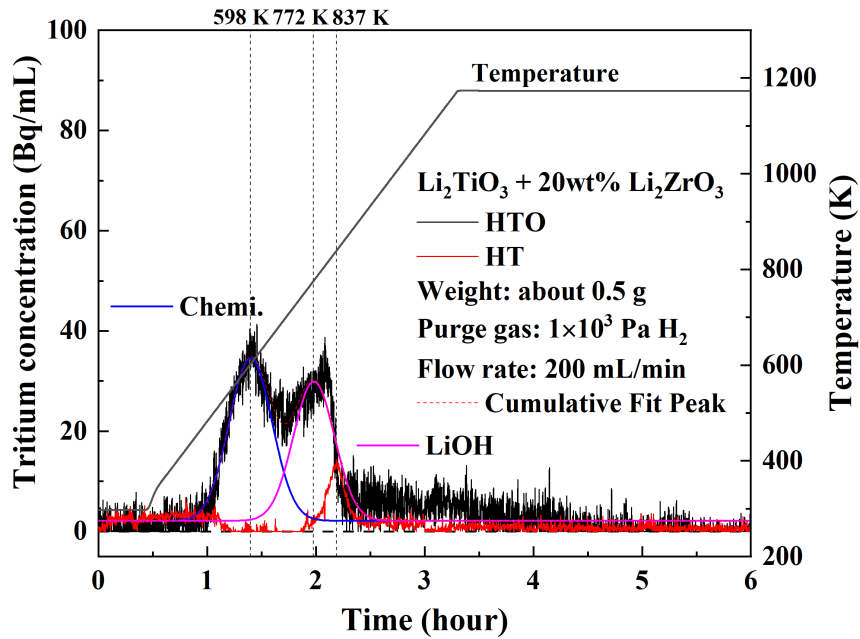

Figure 5.9. Tritium release spectrum when heating the LTZO under the H2 gas purging condition.

In summary, the presence of H_2O species, including sweep gas and vapor release, impeded the desired HT release. Additionally, it concluded that tritium production was insufficient to see the spectrum in the high-temperature region. If pebbles had been irradiated with sufficient thermal neutron fluence, this work would have enabled observing HTO release at around 993 and 1143 K, as seen in Figure 3.8.

Other literature reporting in-situ experiments using LTZO [12, 13] helps anticipate that HT will overcome HTO in all the temperature regions once the water vapor desorption has been completed. In addition, previous works implied that T_2 recovery from stoichiometric Li_2TiO_3 ceramic pebbles [14] and Li_4SiO_4 + 25 mol% Li_2TiO_3 [15, 16] without the hydrogen atom in the sweep gas. These experimental results indicate that generated hot tritium atoms were directly released to the gas phase. Therefore, tritium recovery from LTZO in the molecular form will be dominant except in the initial phase. Moreover, T_2 recovery can be attainable, which helps substantially reduce the burdens of the TEP and ISS. On the other hand, this increases tritium permeation loss through the coolant piping, but the ceramic coating technique [17-19] can effectively suppress the tritium permeation loss.

The HF acid solution could perfectly decompose the stable components, namely Li_2O, TiO_2, and ZrO_2. Speaking of the residual tritium, only a negligible amount was detected, unlike the Pebble200 [20]. These results were preferable from the tritium safety perspective regarding operation and maintenance, especially the blanket exchanges. In other words, almost all the generated tritium was successfully extracted by heating at 1173 K. Defects [21-24], for example, at oxygen vacancy O^- center [23] and Li vacancy [24], annihilated and did not adversely affect tritium retention.

Table 5.3 recapitulates the recovered tritium amount by the PIE and acid digestion experiment based on the tritium chemical forms. It presents the integrated value of all peaks from the beginning to the end, as exemplified in Figure 5.5. As a result, the overall recovered tritium amount was much smaller than the theoretical value.

Table 5.3. Experimentally recovered tritium and theoretical tritium production in Bq g^{-1}.

Gas species	T recovery by PIE		T recovery by HF	Theoretical T production
	HTO	HT		
Ar	5.4×10^5	≈ 0	≈ 0	2.48×10^6
H_2	9.9×10^5	1.7×10^5	≈ 0	
H_2O	1.4×10^6	≈ 0	≈ 0	

Some possible reasons may enlarge the gaps. The first one was the difference in the thermal neutron flux between the one given by KUR and the effective one. The surrounding cotton and container had abundant hydrogen atoms. Hence, hydrogen atoms may have scattered the thermal neutron away before reaching ^6Li atoms. Alternatively, the self-screening effect of the ^6Li atoms may stop the thermal neutron from reaching the bulk of LTZO. Based on the recovered tritium under the Ar, H_2, and H_2O gas environment, equation (5.1)

calculated the effective neutron flux to be 6.0×10^{12}, 1.3×10^{13}, and 1.6×10^{13} cm^{-2} s^{-1}, respectively. Another possible reason is that this work missed the tritium quantification when breaking the tube. As mentioned above, the generated tritium may be directly released into the air inside the quartz tube. This is because the tritons have 2.78 MeV of energy, which is extraordinarily higher than the surrounding bonding energy, for instance, Li-O and trap sites. Besides, tritium may reach the grain surface and interact with the water vapor floating in the quartz tube. During the thermal neutron irradiation, every nuclear reaction and short half-life nuclei deposit tremendous energy on the samples. It rose highly enough to get the surrounding cotton burnt, and the polyethylene container darkened, as shown in Figure 5.10, which increased tritium diffusivity. Plus, the longer time passes, the more tritium can reach the grain surface, even at room temperature. Because of the time limitation and chaotic situation concerning the pandemic since 2020, the experiment was conducted approximately 1.5 years after the neutron irradiation had been performed. Regarding the tritium mass balance, it is recalled that Appendix A elaborates on the calibration of ICs. Appendix B identifies the causes, examining these possible reasons for the gigantic gap.
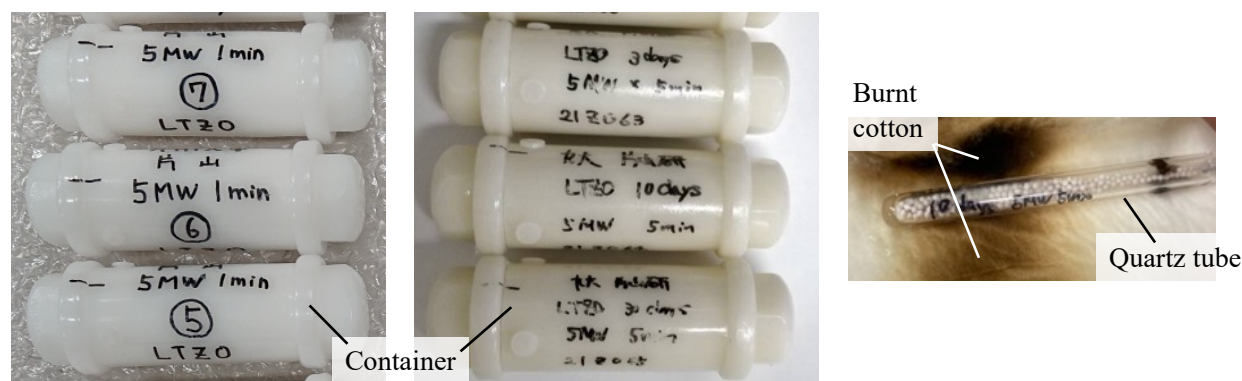

Figure 5.10. Appearance changes of the container (left) before and (center) after the neutron irradiation. The appearance of the burnt cotton (right) after the thermal neutron irradiation.

Subsequently, tritium behavior from the long-term heated samples was investigated to see if the structural changes affect tritium release behavior. In parallel, this work attempted to pursue the HT release. Following the results in Appendix B, two new steps were incorporated into the experimental procedure to rectify the gap using the apparatus, as seen in Figure 5.6. Firstly, the quartz tube was cut in the glove box under the Ar atmosphere to recover tritium floating in the air inside the quartz tube. Secondly, about 0.02g of the sample was immersed in 5 mL of 46% HF solution at room temperature to quantify the tritium amount in advance to become independent of the theoretical value. Additionally, the temperature ramping rate was modified from 5 K min^{-1} to 60 K min^{-1} to eliminate the HTO release due to the chemisorption and LiOH decomposition and to see the isotope exchange reaction with hydrogen atoms, as in equation (2.22).

Table 5.4 summarizes the amount of tritium experimentally recovered before the PIE. The column named Equilibrium is the tritium recovered when cutting the quartz tube. The column called Overall is the tritium

recovered when immersing the sample in the acid solution. Consequently, it was found that about one-third of the produced tritium drifted in the air. This work experimentally reinforced the direct tritium release from the Li sites into the air. Assuming that the volume of the quartz tube is the same as that of a simplified cylindrical geometry, whose diameter is 2 cm and height is 7 cm, the partial pressure of Q_2O and Q_2 at 298 K was 5.61×10^{-3} and 1.61×10^{-3} Pa, respectively. Considering the rotary pump performance, the total pressure was approximately 1×10^{-2} Pa. Given the composition of air, the partial pressure of O_2, H_2O, and H_2 were approximately 2×10^{-3} Pa, 1×10^{-4} Pa, and 5×10^{-9} Pa, respectively. Hence, the tritium gas was expected to exist as T_2O and T_2. Besides, the rising temperature due to the nuclear reaction facilitated the interaction between T_2 and O_2 gas. In addition, dangling O atoms originating from Li_2O seemed to contribute to T_2O.

The summation of Equilibrium and Overall was still less than the theoretical value even though a new procedure was incorporated. On top of that, the gap between the experimental and theoretical values got worse. For now, the following discussion is based on the experimental value.

Table 5.4. Recovered tritium amount in Bq g^{-1}.

Sample	theoretical	Equilibrium			Overall			
		T_2O	T_2	Total	HTO	HT	HF	Total
3-day	1.30×10^7	1.07×10^5	3.06×10^4	1.38×10^5	3.19×10^4	6.91×10^3	2.17×10^5	2.56×10^5
30-day		missed			3.95×10^4	4.97×10^3	5.05×10^5	5.49×10^5

Figures 5.11 and 5.12 show the tritium release curve from the 3-day and 30-day heated samples under H_2 purging conditions. They had multiple prominent HTO and HT peaks in common in the high-temperature region. This was the first case of observing significant tritium release curves, except for the chemisorption and LiOH thermal decomposition. A higher ramp rate allowed two ICs to monitor HTO and HT peaks because the water vapor could quickly desorb from the grains before tritium reached the grain surface.
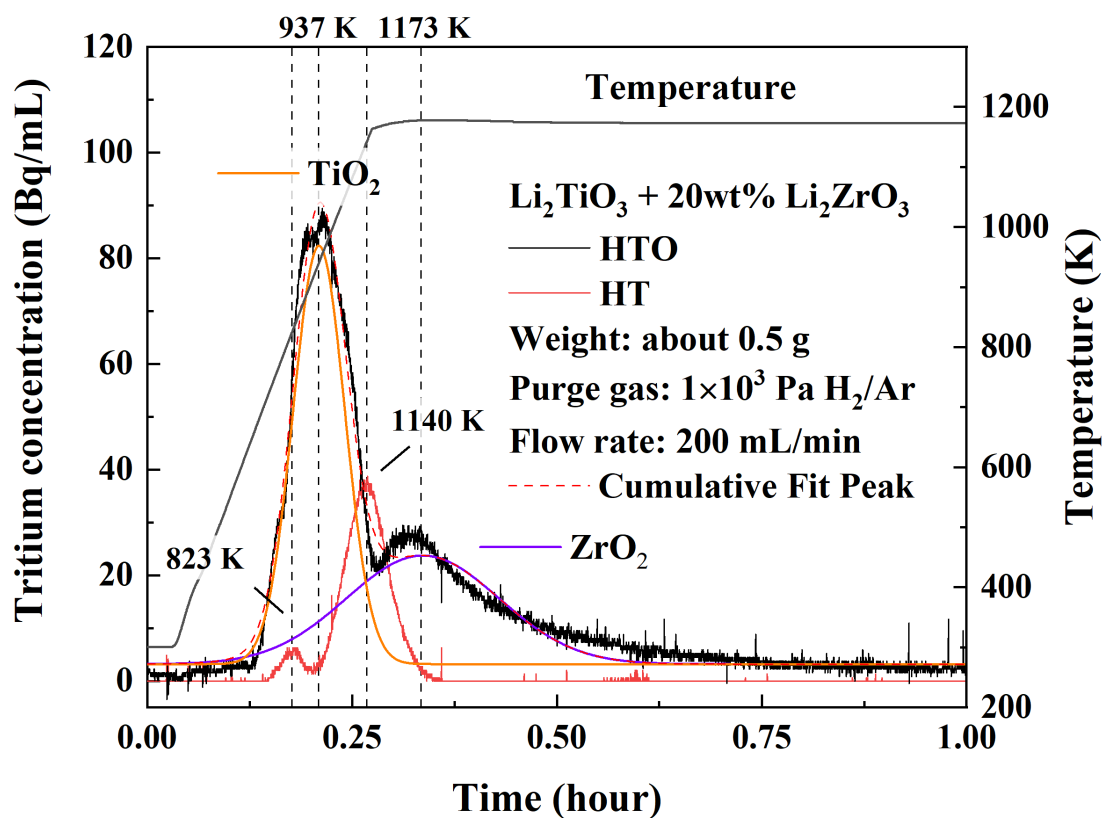
Figure 5.11. Tritium release spectrum from the 3-day heated LTZO.
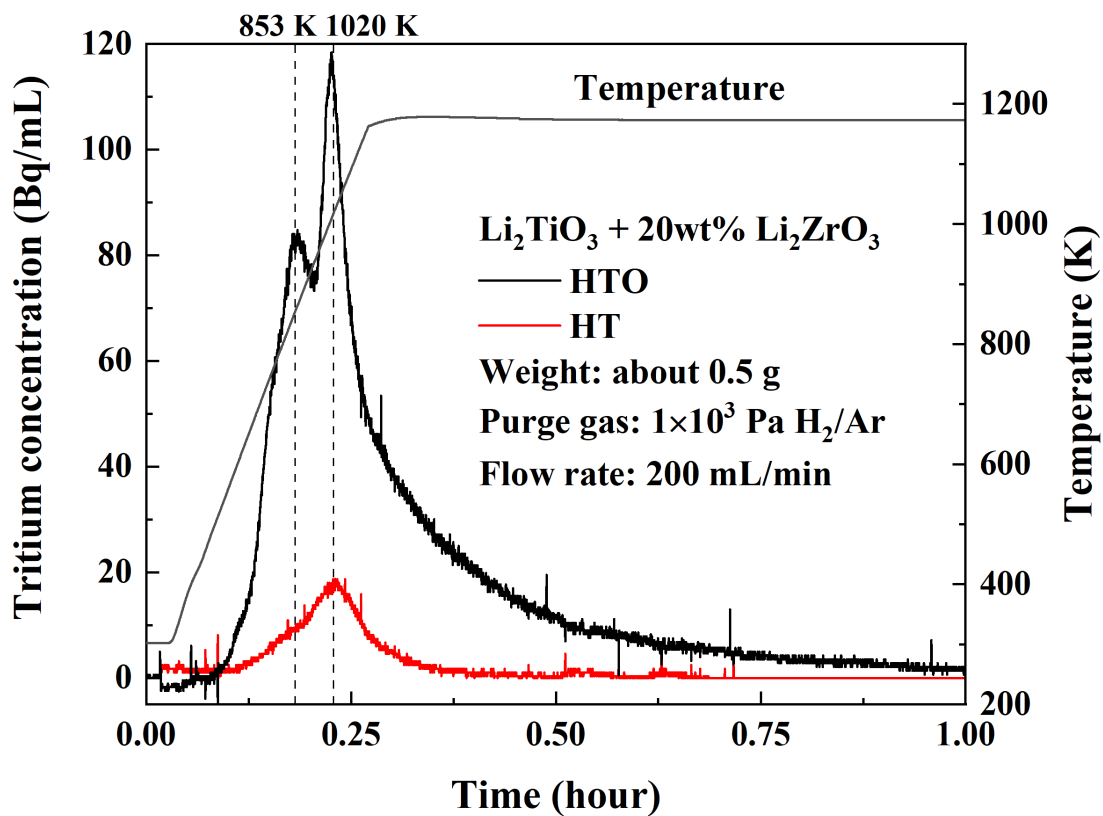

Figure 5.12. Tritium release spectrum from the 30-day heated LTZO.

66

After the experiment, they turned gray. This implied that the redox reaction occurred during the PIE. In the case of the 3-day heated sample, an HTO peak at 937 K and an HTO peak at 1173 K were genuinely attributed to the reduction of TiO_2 and ZrO_2, respectively, as in equations (3.2) and (3.3). In contrast, in the case of the 30-day heated sample, a fitting curve did not converge well with the experimental HTO release curve. However, nothing but the redox reaction can explain these peaks in the high-temperature region when purging under H_2 because no noticeable structural changes were observed in Chapter 4.

As in equation (2.22), the isotope exchange reaction with hydrogen molecules was enhanced thanks to the presence of hydrogen atoms in the purge gas. A more intense HT curve could have been observed if it had been heated at 1173 K until the vapor release ceased before the neutron irradiation.

Table 5.5 presents a concise overview of the tritium counted by the ICs, indicating that the PIE retrieved as much tritium as the acid decomposition. The emission of HT constituted 10% of the total. Apparently, the tritium release curves were different, but the total tritium recovery amount was similar. Hence, it can be concluded that the long-term heating up to 30 days did not adversely influence tritium recovery.

Table 5.5. Recovered tritium amount counted by the ICs in Bq g^{-1}.

Sample	Overall	IC		
		HTO	HT	Total
3-day	2.56×10^5	5.46×10^5	6.47×10^4	6.11×10^5
30-day	5.49×10^5	3.76×10^5	4.06×10^4	4.17×10^5

Table 5.6 recapitulates the tritium mass balance. In this case, the HF acid solution recovered tritium more than the Pebble200 [20]. The HF solution detected roughly 10% of the tritium recovery by the PIE. This resulted from either the PIE experimental procedure or the long-term heating effects. Further investigations are necessary to identify the cause.

Table 5.6. Recovered tritium amount counted by the ICs in Bq g^{-1}.

Sample	Overall	IC	Residual			
			HTO	HT	HF	Total
3-day	2.56×10^5	6.11×10^5	4.97×10^4	1.23×10^4	5.83×10^3	6.78×10^4
30-day	5.49×10^5	4.17×10^5	7.06×10^3	6.20×10^3	1.20×10^3	1.45×10^4

5.4 Summary

Chapter 5 delves into the tritium release behavior. A comprehensive list of the principal discoveries derived from experimental observations is presented here.

Key Findings:

1. **Nuclear Characteristic**: ^{93}Zr atom has a long half-life of 1.61×10^6 years, emitting gamma rays. Neutron irradiation generates gaseous species (e.g., ^{3}He, ^{4}He, and ^{19}F) and metal species (e.g., ^{51}V, ^{93}Nb, ^{95}Mo, and ^{97}Mo).

2. **Surface-Reaction Limited**: The purge gas with H_2 and H_2O gas considerably promoted the tritium release and recovery amount. Otherwise, the diffusion process would determine the overall mass transfer rate, and the curves would become similar.

3. **Tritium Direct Release**: The tritium floating in the quartz tube was experimentally recovered. This demonstrated that some generated tritium could directly jump off the Li sites into the air.

4. **Tritium Release**: A rapid ramping rate allowed ICs to monitor the tritium release behavior in the high-temperature region instead of the ordinary chemisorption release.

5. **Long-Term Heating Effects**: No adverse effects on the tritium release curve were found. In contrast, this possibly increased the tritium residual inventory.

References

[1] Y. Someya et al., Fusion Eng. Des., 146, (2019), 894-897, doi: 10.1016/j.fusengdes.2019.01.107.

[2] Y. Kawamura et al., Fusion Eng. Des., 161, (2020), 112050, doi: 10.1016/j.fusengdes.2020.112050.

[3] Kyoto University Research Reactor Institute, KUR Annual Operating Plan [KUR 年間運転計画]. Retrieved November 22, 2023, from https://www.rri.kyoto-u.ac.jp/KURdiv/info_kur.html.

[4] O. Iwamoto et al., J. Nucl. Sci. Technol., 60, (2023), 1-60, doi: 10.1080/00223131.2022.2141903.

[5] E. Bezak et al., Radiat. Prot. Dosimetry, 167, (2015), 591–601, doi: 10.1093/rpd/ncu362.

[6] Kyoto University Research Reactor Institute. (n.d.). Pressurized Air Transport Pipe Irradiation Facility [圧気輸送管照射設備]. Retrieved November 22, 2023, from http://www.rri.kyoto-u.ac.jp/JRS/inst/pn.pdf.

[7] N. Nakashio et al., Fusion Technol., 33, (1998), 287-297, doi: 10.13182/FST98-A34.

[8] M. Nishikawa, Nucl. Instrum. Methods Phys. Res., 278, (1989), 525-531, doi: 10.1016/0168-9002(89)90875-9.

[9] T. Kinjyo et al., Fusion Eng. Des., 83, (2008), 580–587, doi: 10.1016/j.fusengdes.2007.11.011.

[10] N. Nakashio, "System effect of tritium in the piping system of D-T fusion reactor," Doctoral dissertation of Kyushu Univ., 1998.

[11] K. Hashimoto et al., Fusion Eng. Des., 61–62, (2002), 375–381, doi: 10.1016/S0920-3796(02)00220-X.

[12] T. Hoshino et al., J. Plasma Fusion Res., 93-02, (2017), 83-90 in Japanese.

[13] Y. Kawamura et al., Fusion Eng. Des., 136, (2018), 1550-1556, doi: 10.1016/j.fusengdes.2018.05.055.

[14] Y. Edao et al., Fusion Eng. Des., 112, (2016), 480-485, doi: 10.1016/j.fusengdes.2016.06.013.

[15] T. Kulsartov et al., Nucl. Mater. Energy, 30, (2022), 101115, doi: 10.1016/j.nme.2022.101115.

[16] T. Kulsartov et al., Nucl. Mater. Energy, 30, (2022), 101129, doi: 10.1016/j.nme.2022.101129.

[17] W. Zhang et al., Surface Coat. Technol., 410, (2021), 126960, doi: 10.1016/j.surfcoat.2021.126960.

[18] J. Enels et al., Int. J. Hydrogen Energy, 46, (2021), 13142-13149, doi: 10.1016/j.ijhydene.2021.01.072.

[19] T. Chikada et al., Corrosion Sci., 182, (2021), 109288, doi: 10.1016/j.corsci.2021.109288.

[20] A. Ipponsugi et al, Fusion Eng. Des., 170, (2021), 112495, doi: 10.1016/j.fusengdes.2021.112495.

[21] M. Kobayashi et al., J. Nucl. Mater., 487, (2017), 84-90, doi: 10.1016/j.jnucmat.2017.02.008.

[22] M. Kobayashi et al., Plasma Fusion Res., 13, (2018), 3405048, doi: 10.1585/pfr.13.3405048.

[23] M. Kobayashi et al., J. Nucl. Mater., 458, (2015), 22-28, doi: 10.1016/j.jnucmat.2014.11.047.

[24] R. Shah et al., Phys. Rev. B, 53, (1996), 8257-8261, doi: 10.1103/PhysRevB.53.8257.

Chapter 6. Tritium Permeation Behavior

Outline

This chapter investigates the tritium permeation behavior between the high-temperature and high-pressurized water. First, the background and aim of this work are briefly explained. Next, the essence of the previous tritium and hydrogen permeation research is carefully given. Subsequently, their results are integrated, and in-depth discussion is performed. Then, tritium permeation transient simulation is carefully executed. Finally, a summary of the results of this chapter is presented.

6.1 Introduction

The current JA-DEMO design employs high-temperature and high-pressurized water coolants as the primary and secondary coolants to remove the heat and generate electricity [1-4]. In this case, the primary water coolant carries tritium permeated from the edge plasma and tritium breeding zone through the metal exposed to high temperature. Then, tritium will inevitably reach the secondary coolant through the heat exchanger. Ultimately, tritium is expected to spread to the ocean through the condenser. From the tritium control, safety, and social acceptance viewpoint, it is necessary to experimentally investigate the tritium permeation phenomena. Therefore, this chapter will elaborate on the tritium water-to-water permeation behavior for better understanding and contribute to designing the WDS. To fulfill the goals, the study aims to integrate experimental data to provide new insights into tritium permeation between water, particularly on concentration dependence. Then, a simulation employs the experimental data to investigate the transition of the tritium concentration in the primary and secondary water coolant and the required specifications for the WDS based on global standards.

6.2 Overview of the Previous Studies

The previous studies [5, 6] detailed the tritium and hydrogen permeation experiments. Figure 6.1 illustrates the schematic of the experimental device and provides its details. Inconel, a nickel alloy, is a candidate material for the heat exchanger between the water coolants [7]. Therefore, a one-sided sealed Inconel 600 tube filled with about 14 mL of permeation medium was inserted into a SUS 316 austenite tube filled with about 40 mL of another medium. The Inconel 600 and SUS 316 tubes had been designated primary and secondary sides for permeable medium. Tables 6.1 and 6.2 recapitulate the chemical composition of the Inconel 600 and the geometry of the Inconel 600 and SUS 316. They were equipped with various features like pressure gauges, valves, ribbon heaters, and thermocouples, which allow pressurizing and heating mediums as high as the primary water coolant loop [1–3].
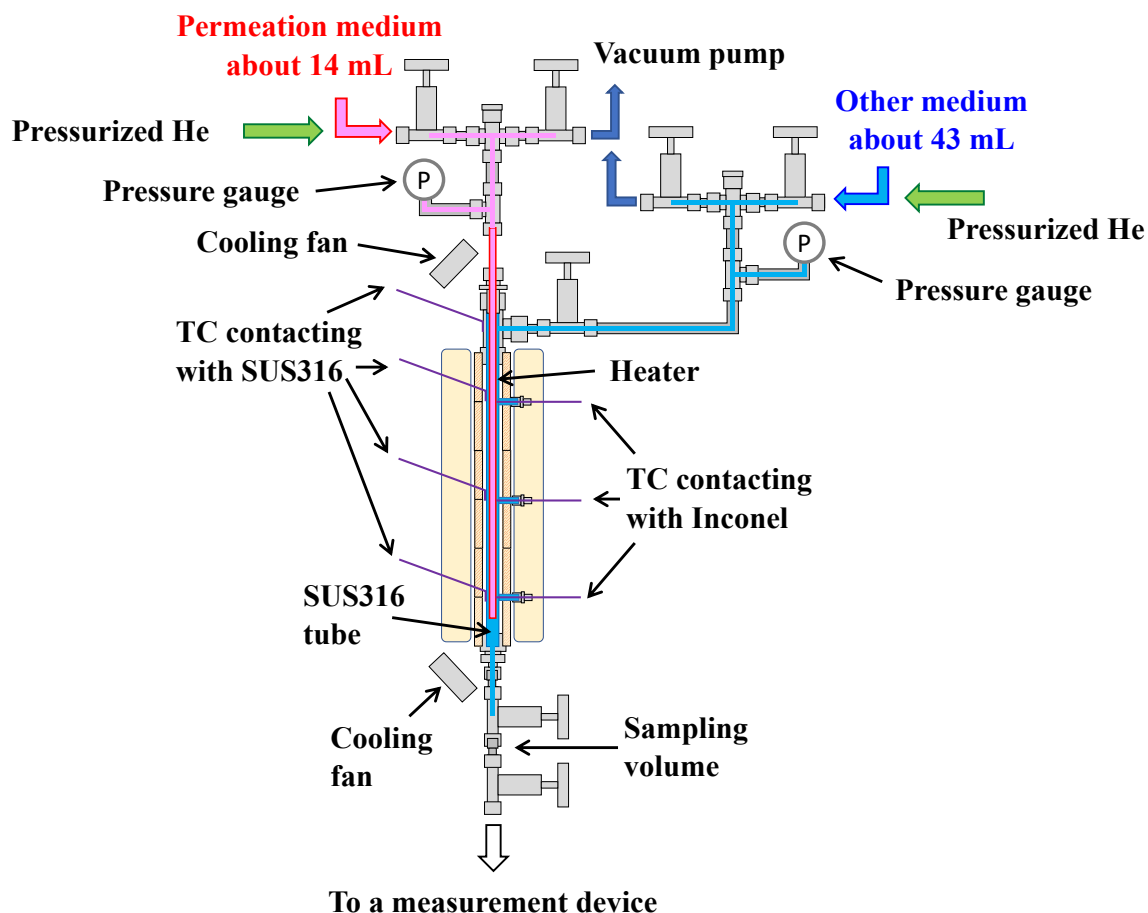
Figure 6.1. Experimental apparatus for the tritium/hydrogen permeation experiment.

Table 6.1. The chemical composition of Inconel 600 (Morimoto Seikan Co., LTD.) in at%.

Ni	Cr	Fe	C	Si	Mn	P	S	Cu
75.04	16.54	7.26	0.01	0.31	0.28	0.01	0.00	0.16

Table 6.2. Dimension of the tubes.

	Inconel 600	SUS 316	Unit
Outer diameter	6.35	12.7	[mm]
Thickness	0.50	1.00	[mm]
Length	400	300	[mm]

The permeated medium outside the Inconel 600 tube was periodically carried to a measurement device by two valves opening and closing, and then its permeation flux was obtained as follows:

$$J_{exp} = Q / A_{eff}, \tag{6.1}$$

where J_{exp} [mol m^{-2} s^{-1}] is the experimental permeation flux, Q [mol s^{-1}] is the permeation rate obtained by the periodic measurement, and A_{eff} [m^2] is the effective surface area of the Inconel 600 tube. In the case of this experimental setup, the effective surface area, A_{eff}, is seen as the outer surface of the Inconel 600 tube, A_s [m^2]. Permeation through the bottom surface of the sealed Inconel 600 tube, A_b [m^2], is negligible when assuming that the diffusion process in bulk controls the permeation rate.

$$A_s = 2\pi L t / \ln(r_2 / r_1), \tag{6.2}$$

$$A_b = \pi r_1^2, \tag{6.3}$$

where L [m] is the length of the permeation area, t [m] is the thickness of the Inconel 600 tube, and r_1 and r_2 [m] are the inner and outer radii, respectively. Hence, A_{eff} was calculated to be 4.58×10^{-4} m^2.

Also, the theoretical permeation flux, J_{theor} [mol m^{-2} s^{-1}], was gained by equation (2.31). The permeation model between gas phases was temporally applied to the permeation between the high-temperature and high-pressurized water. It was assumed that water vapor drove the permeation independently of the hydrogen isotope species, and the diffusion process limited the tritium permeation rate. This work employed the permeation coefficient, K, previously reported [8], investigating hydrogen permeability through Inconel 600 between 600 and 1000 K, and the one [9], studying hydrogen as well as deuterium permeation through Inconel 600 between 943 and 1093 K. Those permeation coefficients were tailored to tritium by multiplying the mass ratio, as in equations (2.37) and (2.38). There is no clue to guess the partial pressure of gas species dissolved in the permeation medium, so it is calculated based on the saturated pressure of the water vapor at 573 K, 8.59 MPa based on a steam table [10]. The gas pressure on the secondary side was assumed to be negligible enough to be set to zero.

Figure 6.2 details where the permeation occurs in the case of tritium permeation. The Inconel 600 and SUS 316 tubes were filled with 0.166 MBq mL^{-1} of tritium-containing and distilled water, respectively. They were pressurized to some degree by He and heated to around 573 K, resulting in a pressure as high as 17 MPa at most. For safety reasons of tritium and high-pressurized fluid, especially when the laboratory was closed, they had to be heated intermittently. The LSC (LSC-5100, ALOKA) periodically measured permeated tritium. Every time it was sampled, the level of the distilled water and the total pressure dropped, so the sampling times were limited to more or less five times to avoid unwanted experimental conditions. Nothing can identify and measure permeated hydrogen from both the primary and secondary sides. Therefore, despite the experimental condition where two hydrogen isotope species existed, it was simplified that tritium permeated independently through the Inconel 600 tube at that moment, as in equation (2.31). The pressure of tritium gas required for equation (2.31) was calculated as follows:

$$P_{T1} = y_T P_{sat} = (C_T \, \varepsilon / 18) \, P_{sat}, \tag{6.4}$$

where P_{T1} and P_{sat} [Pa] is the partial pressure of tritium gas dissolved in water on the primary side and the saturated water vapor pressure, y_T [-] is the atomic fraction of tritium to hydrogen, C_T [Bq-T mL^{-1}-H$_2$O] is the tritium concentration of the permeation medium, 0.166 MBq mL^{-1}, and ε [mol-T Bq^{-1}-T] is the conversion coefficient, as listed in Table 2.1. Any changes in density due to the high temperature and high pressure were not considered to keep it simple, so 18 indicates the molar mass of the water in g mol^{-1}. The tritium partial pressure, $P_{T,1}$, was calculated to 1.19×10^{-2} Pa.
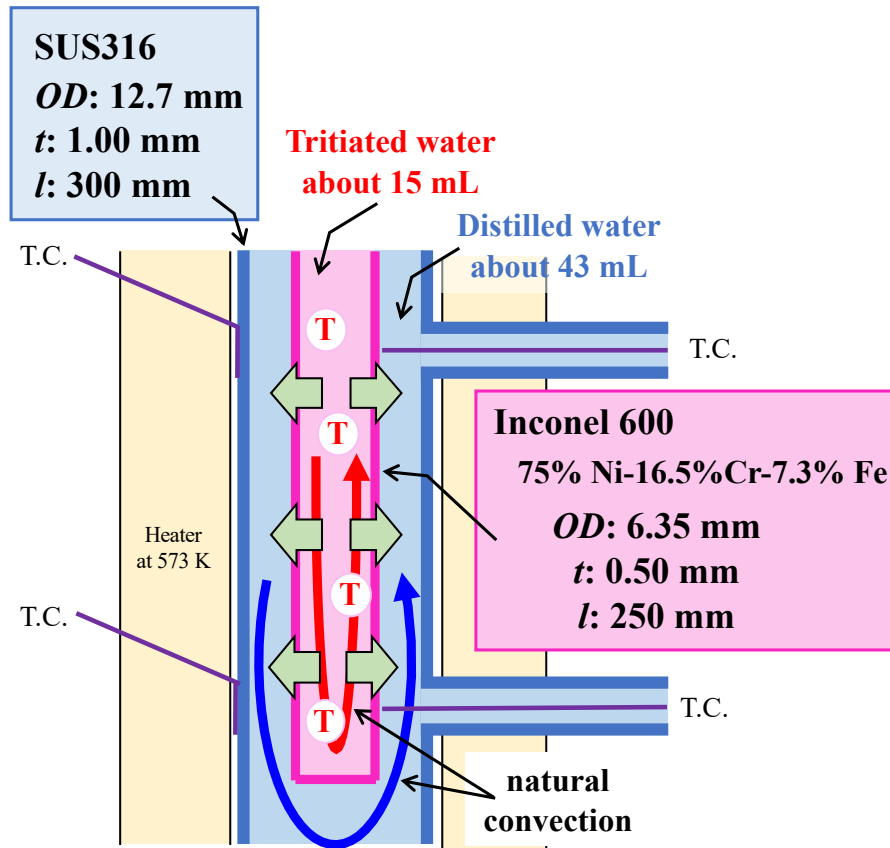

Figure 6.2. The detailed schematic diagram of the tritium permeation experimental device.

Figure 6.3 details where the permeation occurs in the case of hydrogen permeation. While the Inconel 600 tube was filled with distilled water, the SUS 316 tube was filled with Ar gas. Only the distilled water was pressurized to some degree by He gas. Then, they were heated to around 573 K. While the total pressure in the Inconel 600 tube reached as high as 17 MPa at most, the one in the SUS 316 tube was always as high as atmospheric pressure. A gas chromatography (GC) (Tracera, SHIMADZU Co.) periodically measured permeated hydrogen. The area of permeated hydrogen measured by the GC was converted to the concentration with the coefficient obtained when calibrating. Then, it was eventually converted to the permeation rate based on the ideal gas law. Every time it was sampled, the pressure in the Inconel 600 tube fluctuated. To keep the pressure high, heating stopped after every sampling, then re-pressurized to about 17 MPa. In this case, only one hydrogen isotope species existed, so equation (2.31) was applied to obtain theoretical hydrogen permeation values, where the hydrogen gas pressure was equal to the saturated water vapor pressure at 593 K, 8.60 MPa.
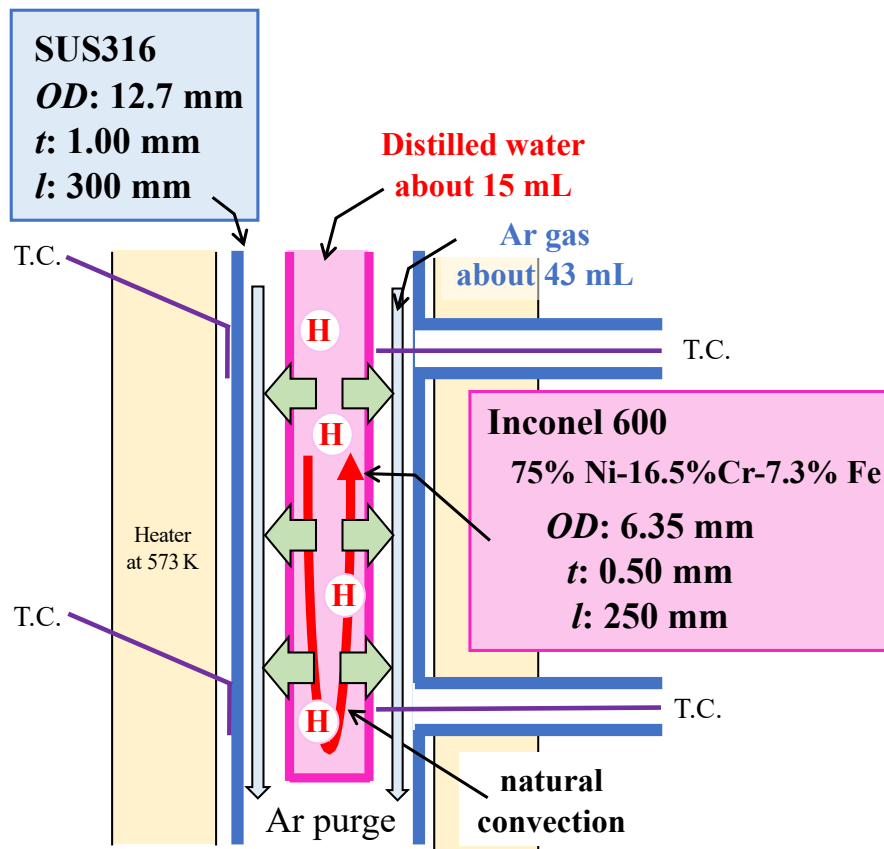
Figure 6.3. The detailed schematic diagram of the hydrogen permeation experimental device.

6.3 Integrated Results and Discussion

The results of the permeation flux gained by equation (6.1) are shown in Figure 6.4, where the theoretical permeation flux obtained by equation (2.31) with the literature values [8, 9] are also presented. Experimentally obtained values were 2.53×10^{-8} and 5.40×10^{-16} mol m^{-2} s^{-1} for hydrogen and tritium experiments, respectively. As a result, there was a gigantic difference in the permeation flux by about 10^8 for the same cumulative heating duration. The difference in the permeability between hydrogen isotopes through the Inconel 600 tube at 593 K no longer creates such a huge gap. In conclusion, the difference in the driving force, namely the atomic ratio between tritium and hydrogen, brought this vast gap. The atomic ratio, T/H, was 1.39×10^{-9}. This roughly nine-orders-of-magnitude gap agreed well with the eight-orders-of-magnitude gap between the experimental fluxes. In short, it was experimentally clarified that the tritium permeation behavior was likely proportional to one order of magnitude of tritium concentration.
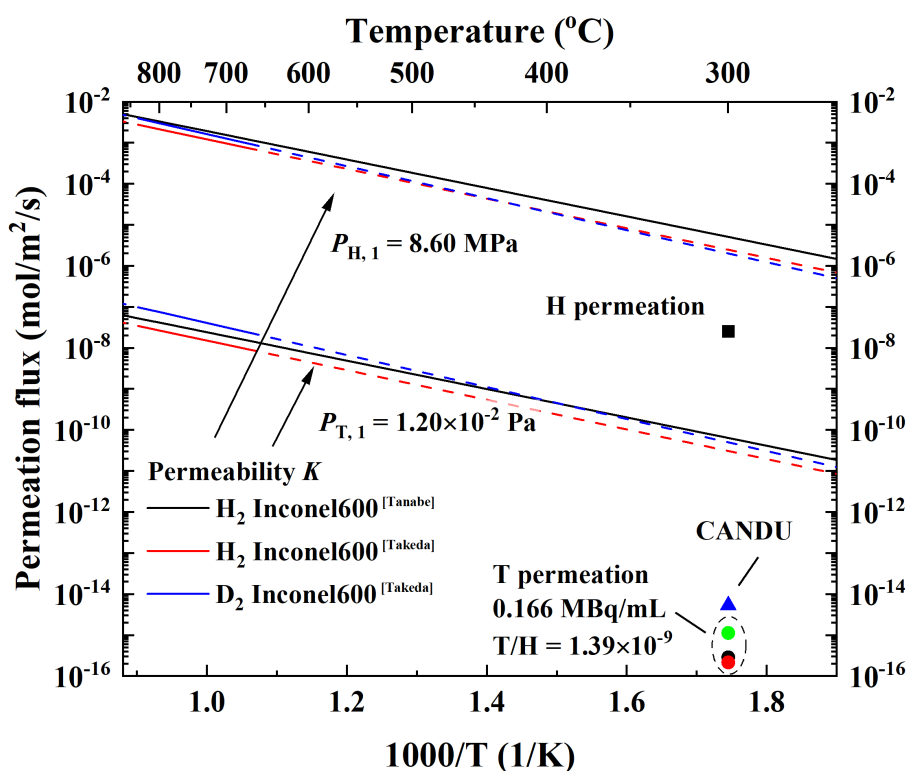
Figure 6.4. Comparison of the experimental and theoretical permeation fluxes
for hydrogen and tritium with the CANDU report value [11].

In addition, the tritium permeation flux was slightly lower than the CANDU experience, 5.35×10^{-15} mol m^{-2} s^{-1} [11], where the heat exchanger employs the same material, Inconel 600. Additionally, there are multiple hydrogen isotope species since hydrogen is usually added to scavenge the oxygen produced from heavy water radiolysis. Although the operation conditions are relatively close, nothing but the permeation fluxes between this work and CANDU experiences can be comparable due to a lack of information on CANDU.

Figure 6.4 also displays a considerable disparity between the experimental and theoretical values. There were roughly two and five orders of magnitude for hydrogen and tritium permeation, respectively. This is likely because the assumption that the saturated vapor pressure at 573 K triggers the permeation led to overestimating the theoretical permeation values. Based on the literature value [8] and the experimental values, the effective gas pressure at 573 K was expected to be 2.11×10^2 and 2.40×10^{-11} Pa for hydrogen and tritium, respectively. This meant that not all the equilibrium water vapor drove the permeation phenomenon.

Growth of the oxide layer is also a key factor affecting the permeation rate. It helps reduce the permeation rate as a mass transfer barrier. The diffusion process inside the oxide layer can be a rate-controlling step because it is porous. The SEM-EDX (JSM-6010PLUS/LA, JEOL Ltd.) observed that the inner and outer surfaces of the Inconel 600 tube were blackened, as shown in Figure 6.5, and precipitations were found, as shown in Figure 6.6. These experimental facts comforted the previous reports that concluded the following oxidation reactions happened, originating from diluted Ni [12, 13] and Fe [14] from the wall into the water. Those products were thermodynamically stable. After the experiment, the LSC detected the tritium molecular-form gas stored inside the Inconel 600 tube. In other words, the water-to-water permeation model should incorporate the redox reaction as another elementary process, and it is expected to be driven by not only the hydrogen isotope molecular-form gas constantly present based on Henry's law but also generated by the redox reaction.
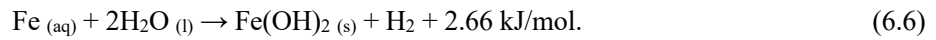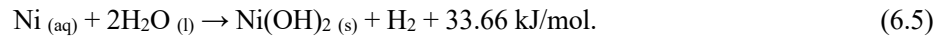
$$Ni_{(aq)} + 2H_2O_{(l)} \rightarrow Ni(OH)_{2\,(s)} + H_2 + 33.66 \text{ kJ/mol.} \tag{6.5}$$

$$Fe_{(aq)} + 2H_2O_{(l)} \rightarrow Fe(OH)_{2\,(s)} + H_2 + 2.66 \text{ kJ/mol.} \tag{6.6}$$

$$3Fe(OH)_{2\,(s)} \rightarrow Fe_3O_{4\,(s)} + 2H_2O_{(g)} + H_2 + 105.0 \text{ kJ/mol.} \tag{6.7}$$
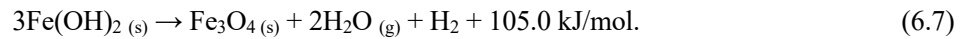
Figure 6.5. Appearance changes of the Inconel 600 tube before and after the experiment.

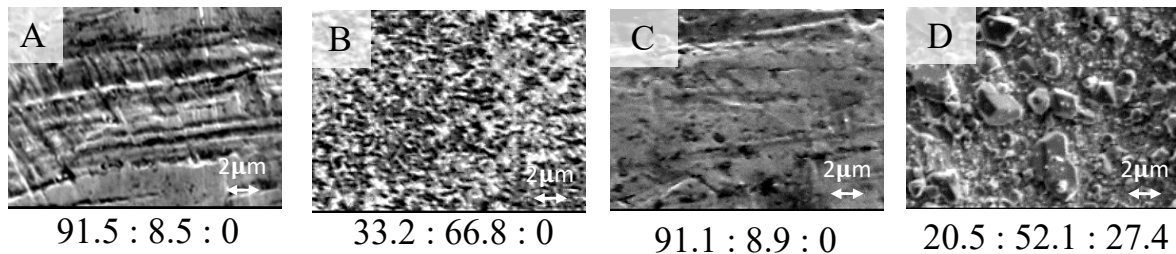| A	B	C	D
91.5 : 8.5 : 0	33.2 : 66.8 : 0	91.1 : 8.9 : 0	20.5 : 52.1 : 27.4

Figure 6.6. SEM images of Inconel 600 and the elemental ratio of Ni : O : Fe in at%.

A and B represent the internal surface before and after experiment, respectively.

C and D represent the external surface facing SUS 316 before and after experiment, respectively.

As discussed in section 2.9, the tritium permeation phenomenon is a series of many elementary processes. Therefore, it is vital to clarify the difference between gas-to-gas and water-to-water permeation and know which elementary process is the rate-controlling step. While the dissolution and diffusion processes do not depend on the surrounding fluid, the surface reaction depends. In short, the critical difference between them is the process until the gas dissolves into the metal. A science handbook [10] says it is energetically harder for water vapor to dissociate into three atoms than dissolved hydrogen gas into two atoms. Hence, it is speculated that the tritium molecular-form gas generated by the redox reactions initiates to pass through the metal despite lots of the equilibrium water vapor.

$$H_{2\,(g)} \rightarrow 2H + 432.07 \text{ kJ/mol.} \tag{6.8}$$

$$H_2O_{\,(g)} \rightarrow 2H + O + 917.8 \text{ kJ/mol.} \tag{6.9}$$
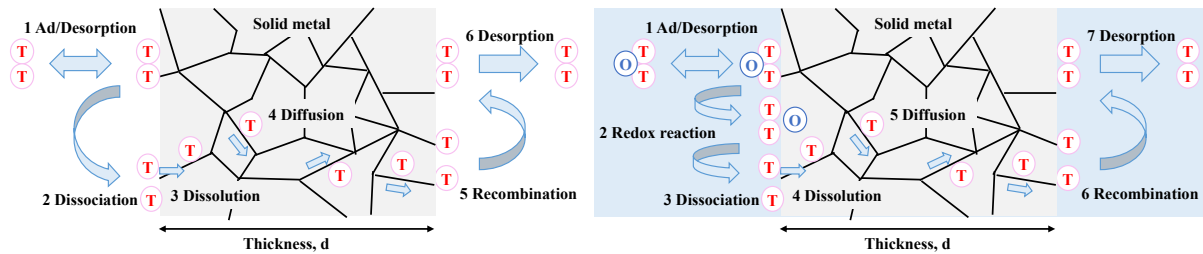
Figure 6.7. Schematic of the tritium permeation behavior
(left) between gas phases and (right) between water.

Based on the currently contemplated water-to-water permeation model, the driving force is the partial pressure of tritium molecular-form gas dissolved in the primary water coolant loop. However, measuring its pressure in the circulated water coolant loop is practically challenging. Meanwhile, the tritium concentration in the primary water coolant is more straightforward to measure. Therefore, organizing the tritium permeation behavior is advisable considering the tritium concentration.

Although there is still uncertainty in the contemplated model, the tritium permeation behavior can be organized by the 0.5, 1, and 2 powers of tritium concentration. Many combinations of the elementary process result in these patterns. For example, suppose water vapor directly dissolves into the metal without the redox reaction. In that case, the permeation flux is proportional to the square root of the tritium concentration if the diffusion process determines the overall rate. In contrast, in the case of water vapor dissolving into the metal with the redox reaction, the permeation flux is proportional to the square of the tritium concentration if the redox reaction process determines the overall rate. As seen in equation (6.5), the chemical reaction between water and the heat exchanger produces tritium gas in proportion to the square of the tritium concentration from the viewpoint of the chemical kinetics. As discussed above, the experimental results showed the possibility that the permeation behavior is proportional to the tritium concentration. This is where the diffusion process of the tritium generated by the redox reaction determines the overall rate.

In Figure 6.8, three green, red, and blue lines are extrapolated from each experimental point. Each color represents tritium concentration dependence when proportional to the 0.5, 1, and 2 powers of tritium concentration. Also, the black broken line represents the expected safety guideline of the primary water coolant loop, 1 TBq kg^{-1} [2]. The hydrogen permeation experiment mocked the situation where the high-temperature and high-pressurized water is exclusively T$_2$O. Those experimental values were not perfectly on the extrapolated line, but those points were located entirely between the supposed lines. As introduced in section 2.9, the previous research on gas-to-gas permeation [15] reported that the pressure dependence of the permeation flux changed by varying the rate-controlling process. Hence, the tritium concentration dependence might also change by altering the rate-controlling process from surface reaction to diffusion. Figure 6.8 discloses four potential boundary values.
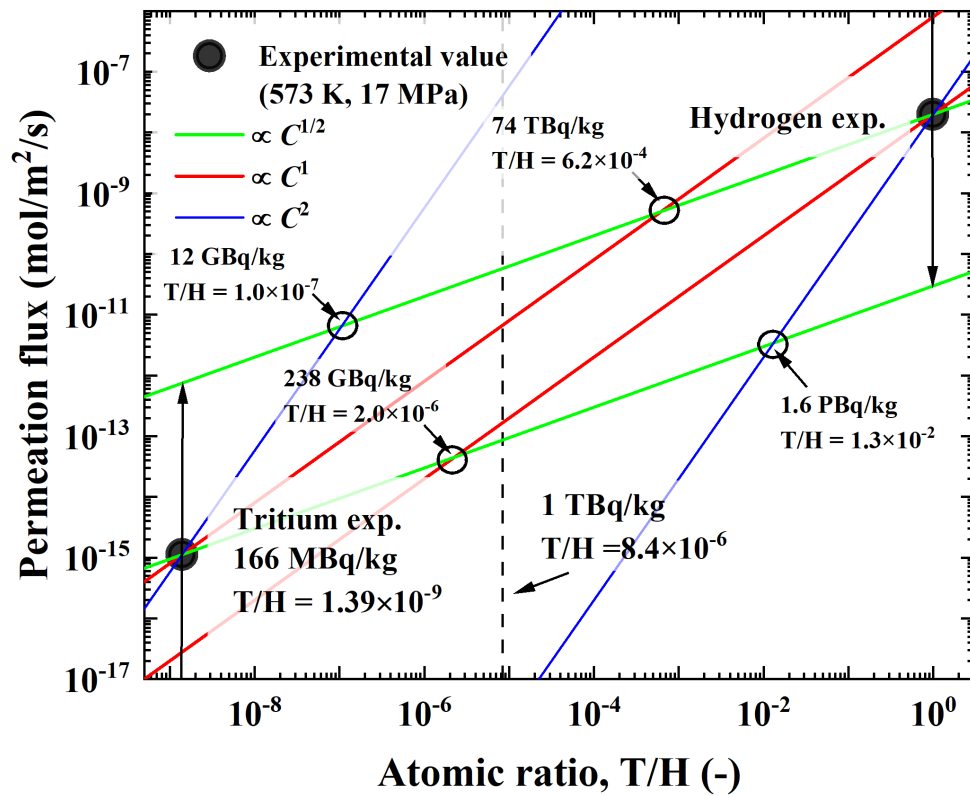
Figure 6.8 Tritium concentration dependence in water-to-water permeation.

6.4 Simulation

This simulation aims to expect the tritium concentration in both water coolant loops at a specific time and clarify the required WDS feed rate based on the experimentally obtained tritium permeation rate.

6.4.1 Simulation Methodology

In general, the following equations can simulate the time transition of the tritium concentration in the primary and secondary coolants with the detritiation system (DS).

$$V_1 \, dC_1 / dt = F_1 - F_2 - F_{DS}, \tag{6.10}$$

$$V_2 \, dC_2 / dt = F_2 - F_3, \tag{6.11}$$

where subscripts (i.e., 1, 2, and 3) denote the primary, secondary, and ternary coolants, respectively, V [m^3] is the volume of the coolant, C [mol m^{-3}] is the tritium concentration in the coolant, t [s] is the operation time, F [mol s^{-1}] are the tritium permeation rate into the coolant through metallic walls, and F_{DS} [mol s^{-1}] is the tritium removal rate from the primary coolant by the DS. Based on the Euler method, this simultaneous ordinary differential equation is extended as follows:

$$V_1 \, (C_1^n - C_1^{n-1}) = \Delta t \, (F_1 - F_2 - F_{DS}), \tag{6.12}$$

$$V_2 \, (C_2^n - C_2^{n-1}) = \Delta t \, (F_2 - F_3), \tag{6.13}$$

where n is the index for the elapsed time since the operation started, and Δt [s] is a mesh width for the calculation loop in time. The initial values for C_1 and C_2 are set to be zero.

The tritium permeation into the primary coolant is driven by the impingement of tritons from the plasma and by the gas released from the breeding materials to the air. The physics transportation model is developed so the operation scenario can fix the permeation rate into the primary coolant.

This work applied equations (6.12) and (6.13) to a computation based on the JA-DEMO design [4]. As discussed above, the water-to-water permeation physics model has yet to be fully established. Therefore, the permeation rate into the secondary water coolant was expressed as follows:

$$F_2 = k_i \, S \, (C_1^i - C_2^i), \tag{6.14}$$

where i ($i = 0.5, 1, 2$) is the index for this calculation based on the assumption of tritium permeation between water coolants through a heat exchanger being proportional to the i power of the tritium concentration, k is the mass transfer coefficient, and S [m^2] is the surface area of a heat exchanger.

The tritium permeation rate into the condenser as the ternary coolant was simplified to zero. Based on the experimental data, the permeation flux into the condenser was expected to be less than that into the secondary coolant by eight orders of magnitude. It was judged to be negligible.

Moreover, the tritium removal rate by the WDS is depicted with the tritium removal efficiency, η [-], and the feed rate, Q [kg s^{-1}], as follows:

$$F_{\text{WDS}} = \eta \, C_1 \, Q. \tag{6.15}$$

Figure 6.9 expounds the calculation geometry. Table 6.3 lists all parameters required for this simulation. The detailed JA-DEMO design concerning the water coolant system still needs to be fixed, such as the water amount and loop number. In this way, it was assumed that each system was composed of a single loop with water volumes of 1300 m^3 and 7000 m^3. The permeation rate into the primary water coolant was assigned based on the previous report [16], which concluded that 3 g of tritium permeated into the primary coolant daily. The mass transfer coefficient referred to the experimental results [5]. Since the tritium concentration heavily relies on the water coolant volume, this work executed a parametric study, ranging the secondary water coolant volume from 4000 to 10000 m^3. The WDS was assumed to be as large as Wolsong [17, 18] in Korea, whose feed rate is 100 kg h^{-1}. After all, each concentration was converted in Bq kg^{-1} with a coefficient listed in Table 2.1. The density of high-pressurized and high-temperature water is set to 1 g mL^{-1}. The plant availability was simplified to 100%.
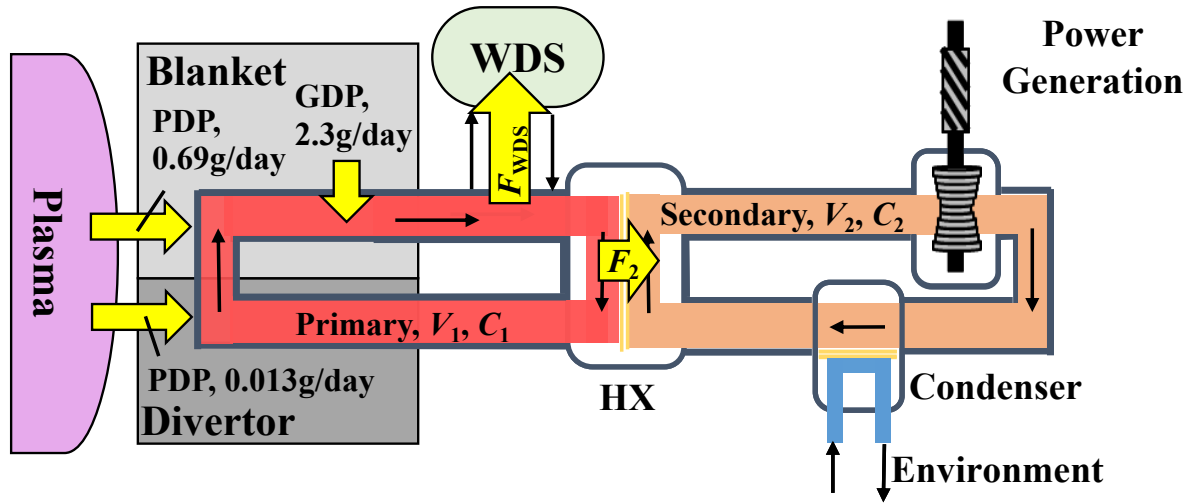
Figure 6.9. Schematic of the water-cooling system

Table 6.3. Parameters used in this calculation.

Symbol		Value	Unit	Ref.
V_1		1,300	[m^3]	
V_2		7,000 ± 3,000	[m^3]	
F_1		0.5	[mol-T$_2$O day^{-1}]	[16]
k	$i = 0.5$	1.10×10^{-8}	[mol$^{1/2}$ m$^{-1/2}$ day^{-1}]	[5]
	$i = 1$	1.25×10^{-6}	[m day^{-1}]	
	$i = 2$	1.62×10^{-2}	[m^4 mol^{-1} day^{-1}]	
S		3,280	[m^2]	[7]
η		0.96	[-]	[2]
Q		100	[kg h^{-1}]	[17, 18]
Δt		1	[day]	

Thanks to the WDS, the tritium concentration in the primary water coolant will be kept at a specific value. Therefore, tritium mass conservation can obtain the required WDS feed rate, varying the tritium control level of the primary water coolant as follows:

$$Q_{\text{WDS}} = R_{\text{by-pass}} \, Q_{\text{prim}},$$ (6.16)

$$R_{\text{by-pass}} = (F_1 / \eta) \, Q_{\text{prim}} \, \varepsilon \, C_{1\text{cont}},$$ (6.17)

where Q_{WDS} and Q_{prim} [kg s^{-1}] is the required feed rate and the mass flow rate of the primary water coolant, respectively, $R_{\text{by-pass}}$ [-] is the by-pass ratio from the primary water coolant to the WDS, $C_{1\text{cont}}$ [Bq-T$_2$O kg^{-1}] is the control value of the tritium concentration in the primary water coolant, and ε [mol-T$_2$ Bq^{-1}-T$_2$] is the conversion coefficient, as listed in Table 2.1.

6.4.2 Results and Discussion

As highlighted in the previous study [18], the tritium concentration, when introduced to the liquid phase catalytic exchange system, which is equivalent to WDS in this case, varied between 37 GBq kg^{-1} (coolant) and 2.2 TBq kg^{-1} (moderator). Therefore, in the following discussion, the upper limit of the tritium concentration in the primary water coolant was set at 1 TBq kg^{-1} to feed into WDS safely, as in the design report [2].

Figure 6.10 illustrates the tritium concentration in the primary water coolant, both with and without the WDS, over three operational years. At the three-year operating point, the tritium concentration amounted to 0.40 TBq kg^{-1} with WDS and 0.90 TBq kg^{-1} without WDS, both figures remaining below 1 TBq kg^{-1}. Notably, the tritium concentration is projected to rise incrementally in extended operations. This is because the concentration disparity between the water coolants drives the permeation into the secondary coolant in this model. Contrary to this model, it is expected that the permeation rates, F_1 and F_2, and the tritium extraction rate of the WDS, F_{WDS}, eventually get balanced, and the tritium concentration in the primary water coolant will reach a steady state in practice. The substantial volume of water coolant can suppress a rapid escalation in tritium concentration, even at a high permeation rate. Hence, the advantages of the WDS are presumed to be modest initially. Therefore, the primary coolant volume and feeding rate to the WDS need to be optimized, considering the heat removal performance of the primary coolant. As a result, the WDS can extract 0.2, 0.74, and 1.4 mg of tritium across one-, two-, and three-year operational periods, respectively, and they are reprocessed to fuel into the plasma again.
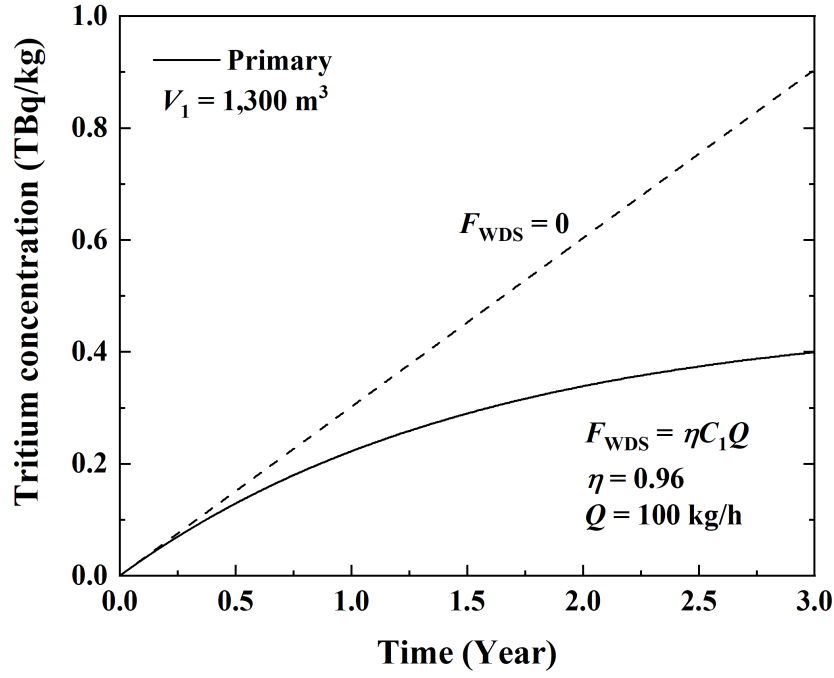
Figure 6.10. T_2O concentration in the primary coolant

Figure 6.11 displays the tritium concentration in the primary and secondary water coolants when employing a Wolsong-like WDS. As elucidated in section 6.3, experimental data revealed that the tritium permeation between high-temperature and high-pressurized water coolants is nearly linear to the tritium concentration. Hence, subsequent discussion centers on the computational outcome based on equation (6.14) for the scenario of $i = 1$ to delve into the tritium concentration in the secondary coolant.
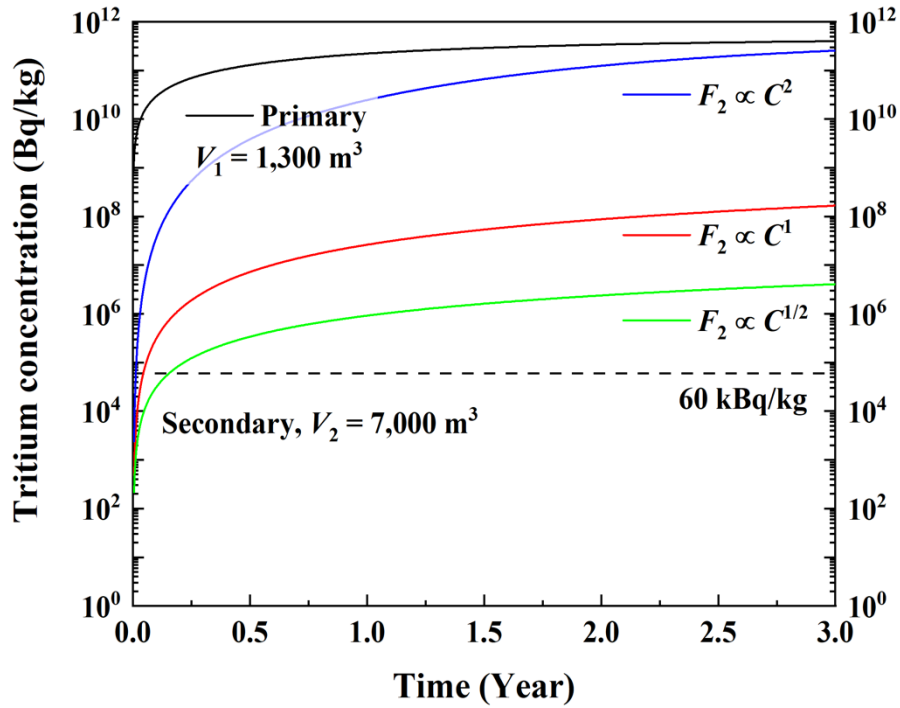
Figure 6.11. T_2O concentration in the coolants, varying the concentration dependence.

82

At the three-year operating point, the tritium concentration in the secondary water coolant loop reached 1.7×10^2 MBq kg^{-1}. If the tritium concentration dependence did change midway, it would occur during the first two weeks when the tritium concentration in the primary water coolant would sharply spike.

Figure 6.12 exhibits the outcome of the parametric analysis for the water coolant volume. No notable discrepancy is observed, even with a variation within the bracket of $7,000 \pm 3,000$ m^3. Additionally, all values markedly exceeded 60 kBq kg^{-1}, the regulatory value in Japan for discharging tritium-containing effluent into the ocean, at more or less 17-day operation. From an operation and maintenance perspective, tritium concentration in the secondary coolant is encouraged to be lessened. As it gets higher, tritium potential risks increase. Besides, the power generation building might need to be decontaminated. In addition, the tritium concentration gap between the secondary and condenser drives the permeation into the condenser. If the tritium concentration exceeds the regulatory value, it requires extra diluting energy before being released into the ocean. Hence, initiatives to mitigate tritium permeation between the three should be advocated to dispose of it without any energy input. Most recently, the possibility of minimizing tritium permeation loss and its potential risks using a ceramic coating [19-21] has been explored.
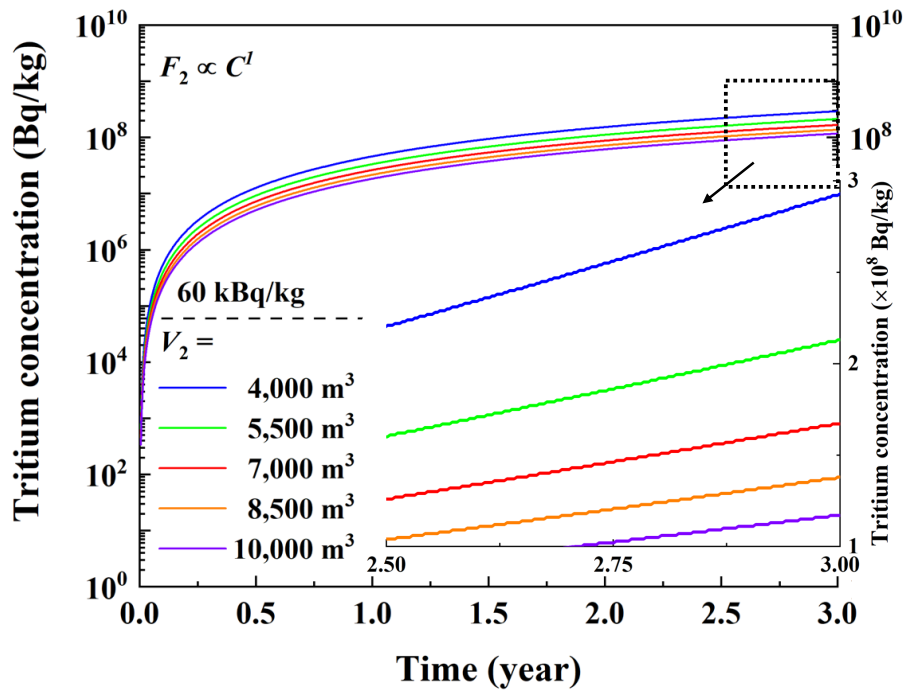
Figure 6.12. T$_2$O concentration in the secondary coolant, whose volume varies from 4000 to 10000 m^3.

Figure 6.13 delineates the required WDS feed rate using equation (6.16) when applying the different control values in equation (6.17). Consequently, in the case of the tritium permeation rate into the primary water coolant loop is 0.5 mol-T_2O/day [15], a feed rate of 46.5 kg h^{-1} was adequate to uphold the primary water coolant tritium concentration at 1 TBq kg^{-1}. This rate is significantly lower than any prevailing WDS globally, such as those at Darlington [22] in Canada, Wolsong [16, 17] in Korea, and ITER [23]. In short, JA-DEMO can downscale the existing WDS specifications to meet a constraint of the primary water coolant tritium concentration, 1 TBq kg^{-1}.
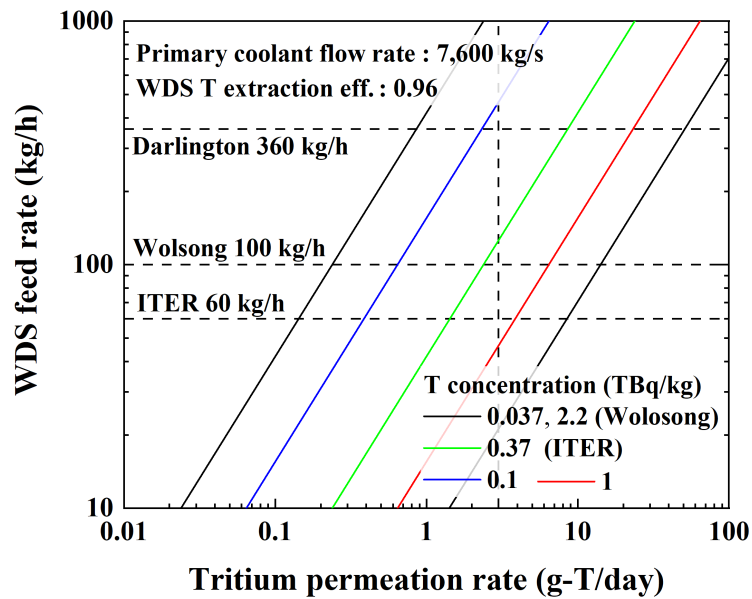
Figure 6.13. Relationship between WDS feed rate and permeation rate.

It should be remembered again that this simulation is based on the experimental data. In other words, it is independent of the water-to-water tritium permeation physics model, for example, the actual tritium concentration dependence, rate-controlling step, etc. Instead, attention should be paid to the figures' firm reliance on the primary and secondary coolant volumes. Even though these figures gave some positive results regarding the design work, there is still a chance that the volume was overestimated in this work. Those values should be optimized with the other factors, especially the thermal energy removal capability.

6.5 Summary

Chapter 6 delves into the water-to-water tritium permeation behavior from the fusion engineering aspects. A comprehensive compilation of the principal discoveries derived from experimental observations and computational simulations is presented here.

Key Findings:

1. **Water-to-Water Tritium Permeation Behavior**: The permeation flux was likely proportional to the first power of the tritium concentration, or the tritium concentration dependence altered midways, resulting from the changes in the rate-degerming process.

2. **Water-to-Water Tritium Permeation Model**: The redox reactions partly constituted the water-to-water physics model. At this moment, the diffusion process potentially constrained the tritium permeation rate.

3. **Tritium Concentration in Coolants**: A 3-year successive operation resulted in 0.4 TBq kg^{-1} in the primary water coolant and 1.7×10^2 MBq kg^{-1} in the secondary coolant when the permeation was proportional to the tritium concentration.

4. **WDS Specification**: 46.5 kg h^{-1} of the WDS feed rate was adequate to hold the tritium concentration in the primary water coolant at 1 TBq kg^{-1}. JA-DEMO can even downscale the WDS specifications operating worldwide.

References

[1] K. Tobita et al., Fusion Sci. Technol., 75, (2019), 372–383, doi: 10.1080/15361055.2019.1600931.

[2] R. Hiwatari et al., Fusion Eng. Des., 143, (2019), 259-266, doi: 10.1016/j.fusengdes.2019.03.174.

[3] Y. Someya et al., Fusion Eng. Des., 146, (2019), 894-897, doi: 10.1016/j.fusengdes.2019.01.107.

[4] Y. Iwai et al., Fusion Eng. Des., 166, (2021), 112261, doi: 10.1016/j.fusengdes.2021.112261.

[5] K. Katayama et al., J. Nucl. Mater., 565, (2022), 153723, doi: 10.1016/j.jnucmat.2022.153723.

[6] A. Ipponsugi et al., Fusion Sci. Technol., Online published, doi: 10.1080/15361055.2023.2271228.

[7] Y. Miyoshi et al., Fusion Eng. Des., 136, (2018), 1577-1580, doi: 10.1016/j.fusengdes.2018.05.060.

[8] T. Tanabe et al., J. Nucl. Mater., 123, (1984), 1568-1572, doi; 10.1016/0022-3115(84)90304-0.

[9] T. Takeda et al., Nucl. Technol., 146, (2004), 83-95, doi: 10.13182/NT04-A3490.

[10] Handbook of Chemistry: Pure Chemistry, 4th ed., Maruzen Publishing Co., Ltd., 1999.

[11] S. Tosti et al., Fusion Eng. Des., 43, (1998), 29–35, doi: 10.1016/S0920-3796(98)00191-4.

[12] N. S. Mclntyre et al., J. Electrochem. Soc., 126, (1979), 750–760, doi: 10.1149/1.2129132.

[13] J. B. Ferguson et al., Metall. Mater. Trans. A, 37, (2006), 2471-2479, doi: 10.1007/BF02586220.

[14] E. M. Field et al., Corrosion Sci., 5, (1965), 361-370, doi: 10.1016/S0010-938X(65)90520-2.

[15] H. D. Röhrig et al., Nucl. Eng. Des., 34, (1975), 157-167, doi: 10.1016/0029-5493(75)90164-8.

[16] K. Katayama et al., Fusion Eng. Des., 169, (2021), 112576, doi: 10.1016/j.fusengdes.2021.112576.

[17] K.M. Song et al., Fusion Sci. Technol., 48, (2005), 290-293, doi: 10.13182/FST05-A929.

[18] K.M. Song et al., Fusion Eng. Des., 82, (2007), 2264-2268, doi: 10.1016/j.fusengdes.2007.07.026.

[19] W. Zhang et al., Surface Coat. Technol., 410, (2021), 126960, doi: 10.1016/j.surfcoat.2021.126960.

[20] J. Enels et al., Int. J. Hydrogen Energy, 46, (2021), 13142-13149, doi: 10.1016/j.ijhydene.2021.01.072.

[21] T. Chikada et al., Corrosion Sci., 182, (2021), 109288, doi: 10.1016/j.corsci.2021.109288.

[22] T.S. Drolet et al., Nucl. Technol. Fusion, 5, (1984), 17-29, doi: 10.13182/FST84-A23074.

[23] M. Glugla, "Detritiation systems for ITER," Rayonnements Ionis. Tech. Mes. Prot., 4, (2014), 6-15.

Chapter 7. Conclusion

This thesis specializes in the tritium fuel cycle to contribute to the engineering design of the blanket, water coolant loops, and the WDS. Specifically, this work elaborates on the Li mass loss and tritium release behaviors from the LTZO ceramic pebbles and tritium permeation behavior between the water coolants. This work presents the conclusion based on the following discoveries.

Blanket

Regarding the LTZO ceramic pebble, it is expected that the LTZO had intrinsic point defects to house extra Li. LTZO had the same monoclinic crystal structure as β-Li_2TiO_3, consisting of Li_2O, TiO_2, and ZrO_2. It had versatile water vapor release mechanisms, for example, two chemisorption releases, LiOH thermal decomposition, and water formation reactions derived from the TiO_2 and ZrO_2. The grain size is 3.3 μm on average and smaller than the desired grain size of 5 μm. The BET-specific surface area was found to be 0.15 m^2 g^{-1}. Regarding the nuclear characteristic of the LTZO, activating the ^{92}Zr atom, whose natural abundance is 17.15%, is detrimental. Thermal neutrons generate gaseous species (e.g., ^3He, ^4He, and ^{19}F) and metal species (e.g., ^{51}V, ^{93}Nb, ^{95}Mo, and ^{97}Mo).

The Li mass loss behavior is represented by $Y = 0.985 + 0.015 \exp(- 0.029 P_{H2O}^{1/2} \exp(- 16839 / RT) t)$. It was likely that energetically unstable Li_2O preferentially interacted with the water vapor in the gas phase to reduce its chemical potential. LTZO would lose 1.5 wt% of the pebble at most. The long-term heating at 1173 K under H_2 purging conditions for up to 30 days did not significantly change its chemical composition, crystal structure, and grain diameter. The presence of ZrO_2 and quick desorption of LiOH prevented LTZO from grain growth.

On the other hand, it was experimentally found that LiOH adhered to the pebble bed and traveled away downstream. On top of that, it was simulated that Li was swiftly depleted in a fusion environment in the early stage of operation, limiting the benefit of the higher Li density. In contrast, Li mass loss did not profoundly affect the tritium production.

Due to its small grain size, the purging gas species determined the overall tritium release rate from the LTZO grain to the air. The various water vapor release mechanisms helped release tritium as HTO. Isotope exchange reactions with water vapor and hydrogen molecules enhanced tritium release. Furthermore, it was disclosed that some generated tritium could directly jump off the Li sites into the air. The negative impacts of the long-term heating on the tritium release behavior were not confirmed but could potentially affect the residual inventory.

In conclusion, this work recommends the usage of the LTZO ceramic pebbles in the blanket. The additional Li_2ZrO_3 achieves special features of the LTZO ceramic pebble, which regular Li_2TiO_3 ceramic pebble lacks. Above all, the primary strength of LTZO is it can be treated as β-Li_2TiO_3 and has the advantages that ordinary Li_2TiO_3 ceramic pebbles have. It boosts the Li density and realizes efficient tritium production. Also, thanks to ZrO_2, the water vapor formation reaction facilitates the tritium release and significantly prevents grain growth. Therefore, the prompt tritium release can be guaranteed even in the later operation phase. Although it causes the energetically unstable Li_2O mass loss and interaction between ZrO_2 and the water vapor, it is an acceptable loss of chemical stability and manageable from the fusion engineering aspect because they will eventually cease. Also, the existence of ^{93}Zr is manageable in the future if the nuclear spallation reaction is applied [1, 2], while lithium zirconate pebbles are avoided [3, 4]. In contrast, LTZO can cause a problem regarding material compatibility with the structural material because it releases the corrosive gas containing LiOH and ^{19}F (e.g., F_2, and TF) more than ordinary Li_2TiO_3 pebbles.

Water Coolant and WDS

Regarding the tritium permeation behavior, the permeation flux was likely proportional to the first power of the tritium concentration because the diffusion process limited the overall mass transfer rate. There was room for consideration that the tritium concentration dependence altered midways, resulting from the changes in the rate-degerming process from the surface reaction to the diffusion. It was simulated using the experimental results that tritium concentration in the primary and secondary water coolant loop reached 0.4 $TBq\ kg^{-1}$ and $1.7 \times 10^2\ MBq\ kg^{-1}$, respectively. 46.5 $kg\ h^{-1}$ of the WDS feed rate was adequate to hold the tritium concentration in the primary water coolant at 1 $TBq\ kg^{-1}$, allowing JA-DEMO to downscale the worldwide operating WDS specifications.

In conclusion, the surface interaction between metal and water causes the permeation behavior of the generated hydrogen isotope gas from water to water. The dependence on tritium concentration varies by a power of 0.5, 1, or 2, depending on the process that determines the rate. Currently, the rate is considered proportional to the tritium concentration in the primary cooling water. Based on the previous study [5], JA-DEMO can adopt and even downsize the existing WDS specification or optimize the primary cooling water volume. If a tritium permeation barrier is implemented, its specifications could be further reduced.

References

[1] T. Wakabayashi, Sci. Rep., 11, (2021), 22443, doi: 10.1038/s41598-021-01986-w.

[2] X. Y. Sun et al., Sci. Rep., 13 (2023), 1693, doi : 10.1038/s41598-023-29002-3.

[3] F. A. Hernández et al., Fusion Eng. Des., 137, (2018), 243-256, doi: 10.1016/j.fusengdes.2018.09.014.

[4] S. J. Piet et al., Fusion Technol., 19, (1991), 146-161, doi: 10.13182/FST19-1-146.

[5] K. Katayama et al., Fusion Eng. Des., 169, (2021), 112576, doi: 10.1016/j.fusengdes.2021.112576.

Chapter 8. Future Outlooks

The chemical engineering approach is mandatory to solve engineering problems and design complex tritium fuel cycles. This approach constructs scientifically reliable engineering models by analyzing macroscopic phenomena. Fundamental physical and chemical microscopic elementary processes at each time and spatial scale emerge as visible phenomena overlappingly. This is why chemical engineering only requires details of some critical elementary processes. Therefore, the following studies are encouraged to be performed from a chemical engineering standpoint to compensate for this dissertation and proceed toward realizing fusion power.

Li Mass Loss Behavior

Limiting the corrosion layer formed by LiOH is crucial to guarantee the structural soundness of components subjected to high-temperature and corrosive environments for a long time. Hence, it is imperative to identify the spatial distribution (i.e., how far it will reach), chemical composition (i.e., Li, LiOH, or other Li compounds with the species of the structural material), and the thickness of the corrosion layer.

In addition, the existing model says that the disparity in chemical potential drives Li mass loss behavior. This study experimentally demonstrated that Li mass loss from LTZO proceeded toward the stoichiometric ratio and would eventually stop. Nevertheless, whether this phenomenon will cease during neutron irradiation, which consistently introduces defects and changes the local crystal structure and chemical state, remains to be investigated. Hence, it is necessary to carry out in-situ experiments to see if equation (4.3) can accurately project the mass transfer.

Tritium Release Behavior

Advanced numerical models are required to forecast the tritium release behavior in fusion reactors accurately. First of all, it is urgent to integrate the primary tritium release models [1, 2]. Then, the missing elements should be augmented. For example, the grain size varies with time, which extends the diffusion process and potentially modifies the rate-determining processes. Furthermore, it needs to be considered that some tritium is released into the gas without surface reactions. Eventually, it needs to be validated by in-situ experimental results.

Furthermore, it is necessary to experimentally examine the effects of dangling O and He resulting from the ^{6}Li(n, α)T reaction and tritium decay. The bond-free oxygen can potentially alter T_2 into T_2O. ^{4}He from the nuclear reaction and ^{3}He from the decay of tritium could impact tritium retention, as discussed when employing tungsten as a plasma-facing material [3, 4].

Tritium Permeation Behavior between Water

Further investigation is necessary to thoroughly examine the tritium permeation behavior in water-to-water systems to establish a physics model that is highly credible for this occurrence. The discussion assumes that the hydrogen isotopes permeate independently, as in equation (2.31). Future work demands the exploration of the potential for hydrogen isotope co-permeation, as in equation (2.33). Furthermore, it is essential to acknowledge that the metal surface on the secondary side is consistently exposed to an equivalent amount of hydrogen as on the primary side. In other words, while tritium only permeates from the primary side, hydrogen can permeate from both ends. This phenomenon of hydrogen isotope crossover permeation is exclusive to the water-to-water permeation. Moreover, although experiments are challenging, additional data points from previous studies are essential to facilitate a productive discourse on tritium concentration dependence, as shown in Figure 6.8. Ultimately, this research necessitates experiments in a dynamic and circulated field, focusing on the mass transfer within the fluid film layer.

Regarding corrosion, it is crucial to thoroughly examine additional parameters related to material deterioration, including pH, dissolved oxygen, dissolved concentrations of Ni and Fe, and temperature. Figures 6.5 and 6.6 and equations (6.5), (6.6), and (6.7) provide insights into these aspects. The presence of precipitation on the heat exchanger significantly hinders the efficient heat transfer by fluids. Conversely, a thick oxide layer can dramatically decrease the tritium permeation amount, referred to as the permeation reduction factor (PRF) [5, 6]. Future work can examine the variation of the oxide layer and tritium permeation rate with time.

References

[1] T. Kinjyo et al., Fusion Eng. Des., 83, (2008), 580-587, doi: 10.1016/j.fusengdes.2007.11.011.

[2] M. Kobayashi et al., Plasma Fusion Res., 13, (2018), 3405048, doi: 10.1585/pfr.13.3405048.

[3] M. Shimada et al., Nucl. Mater. Energy, 12, (2017), 699-702, doi 10.1016/j.nme.2016.11.006.

[4] Y. G. Li et al., Tungsten, 2, (2020), 34-71, doi: 10.1007/s42864-020-00042-w.

[5] S. Tosti et al., Fusion Eng. Des., 43, (1998), 29–35, doi: 10.1016/S0920-3796(98)00191-4.

[6] H. Nakamura et al., J. Nucl. Mater., 329-333, (2004), 183-187, doi: 10.1016/j.jnucmat.2004.04.009.

Appendix A

Outline

This chapter carefully describes the procedure to calibrate the ICs. This builds a foundation for the tritium mass balance between experimentally recovered tritium amount and theoretical tritium production.

A.1 Introduction

As presented in Figure A.1, the IC is a device that detects and measures the gas containing ionizing radiation, for instance, alpha, beta, gamma, and neutron rays. The radioactive element emits radiation inside the chamber and ionizes the gas molecules, and then IC records the ionization current as radioactivity. Hence, it is compulsory to relate the radioactivity concentration, C [Bq L^{-1}], to the ionization current, I [A]. The relationship is written using the unit conversion coefficient, K [Bq L^{-1} A^{-1}].

$$C = KI. \tag{A.1}$$
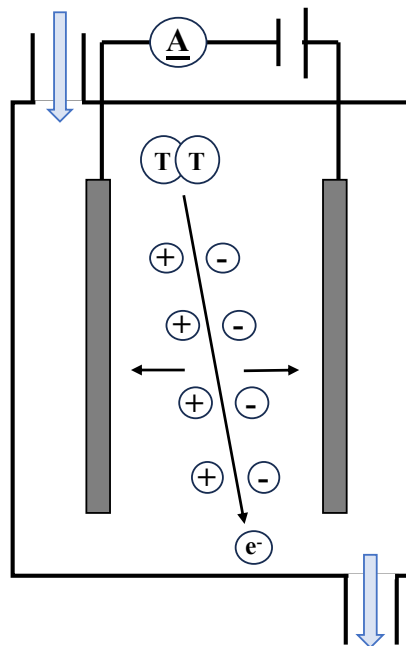
Figure A.1. The schematic of the ionization chamber.

A.2 Procedure

Figure A.2 shows the experimental setup to gain the unit conversion coefficient, K. First of all, the tritium concentration of the supply gas was identified. The gaseous tritium existed as both HT and HTO. A molecular sieve trapped HTO gas and H_2O gas was introduced to the ICs to lower the memory effect. Therefore, only HT gas flowed to the ICs. The tritium concentration of the HT gas, C, was substituted into equation (A.1).

The HT gas went through two ICs and a CuO bed, transforming HT into HTO. Subsequently, the first bubbler collects almost all the generated HTO. Then, the LSC quantified its tritium concentration. In general, the LSC can accurately measure the low-energy beta particles within subtle measurement errors. Considering the tritium mass balance, the HT gas concentration, C, is obtained as follows:

$$Cvt = xV, \tag{A.2}$$

where v [L min^{-1}] is the mass flow rate of the tritium gas, t [min] is the cumulative duration that the tritium gas cylinder opens, x [Bq L^{-1}] is the tritium concentration in the bubbler, and V [L] is the volume of the bubbler. Given the experimental conditions for tritium release, the total mass flow rate is fixed at 200 mL min^{-1}, mixing HT and H_2O equally.
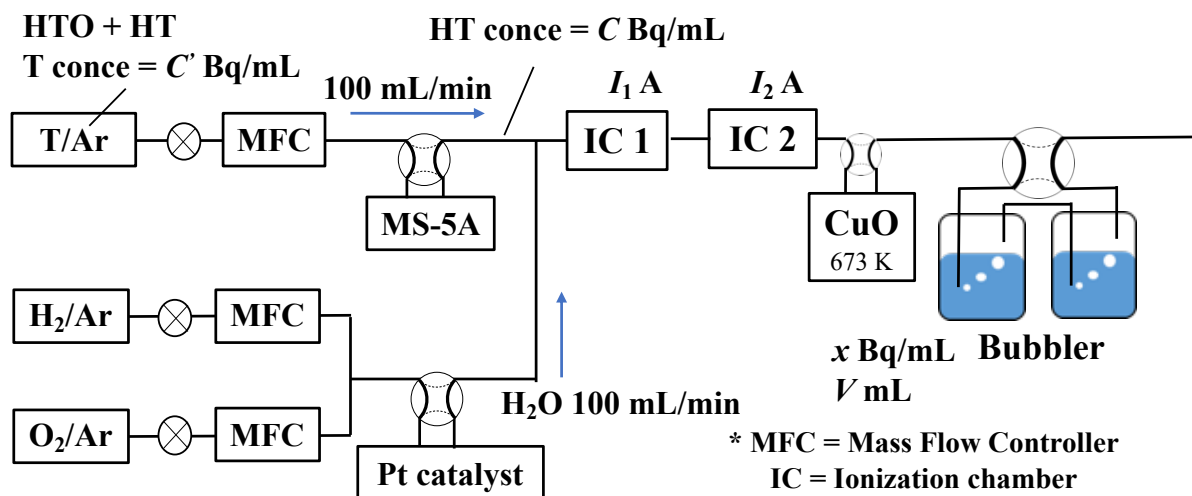
Figure A.2. Schematic of the experimental apparatus.

As illustrated in Figure A.3, the unit conversion coefficient, K, is gained from the steady current, I, corresponding to the known tritium concentration, C. Due to the system effect, it takes a few minutes for the ICs to reach a steady state. Additionally, their signal intensity is tiny enough to be amplified by just touching the cables and shaking and shocking the piping when sampling the tritium concentration in the set of bubblers. Therefore, the unit conversion coefficient was credited to the LSC and several iterations of the procedure. Table A.1 summarizes the coefficients used in this work.
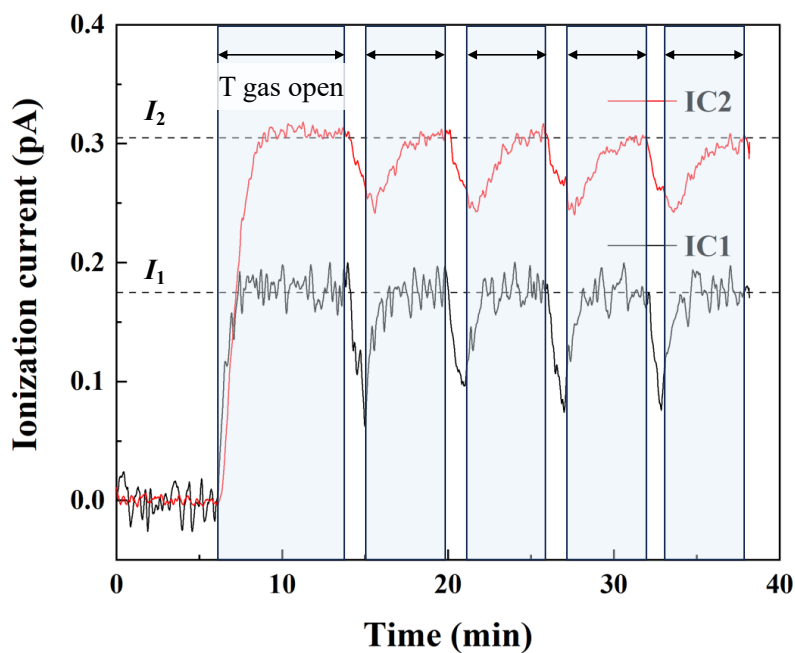
Figure A.3. Example of the ionization curves.

Table. A.1. Unit conversion coefficient, K, used for the tritium release experiments.

	IC 1	IC 2	Unit
As-received LTZO	2.63×10^{14}	1.53×10^{14}	Bq mL^{-1} A^{-1}
Long-term heated LTZO	7.26×10^{13}	7.05×10^{13}	Bq mL^{-1} A^{-1}

Appendix B

Outline

This chapter identifies the causes of the vast gap between the experimental tritium recovery amount and the theoretical tritium production, as discussed in section 5.3.2. First, three possible causes and two approaches are briefly explained. Next, two of the three causes are explored using simulation software. Subsequently, the last is carefully investigated with calculations. Finally, a summary of the results of this chapter is presented.

B.1 Introduction

As discussed in section 5.3.2, the potential causes are briefly listed here.

1. Difference in the thermal neutron flux.

2. Direct release from the Li site to the air.

3. Diffusion of tritium to the air.

There are many tools and methods to achieve this purpose. This work took two approaches. The first is the general-purpose simulation code to examine all items. The second is the manual calculation of the heat transfer of the pebble during the thermal neutron irradiation to explore the possibility of item 3.

Figure B.1 shows a schematic diagram of the actual geometry for simulation. The quartz tube filled with the sample pebbles was placed coaxially with the absorbent cotton, the polyethylene container, and the Pn-2 transportation tube.
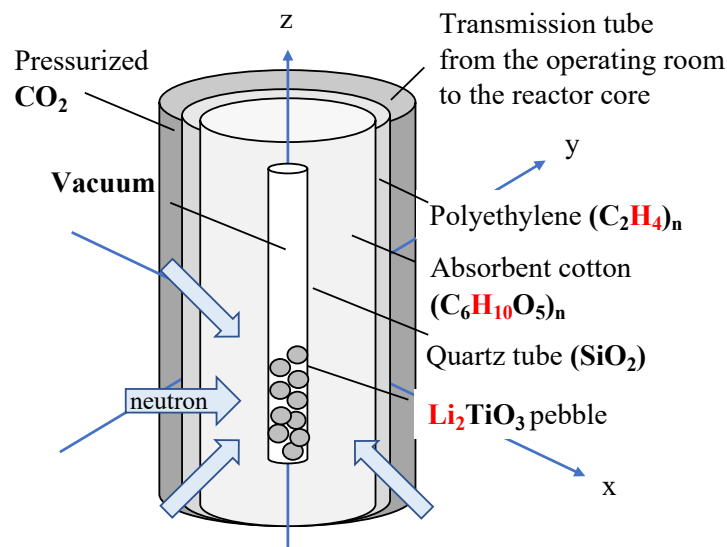
Figure B.1. Schematic diagram of the actual geometry when neutron irradiated.

B.2 PHITS Simulation

This work utilizes PHITS version 3.31 [1], a comprehensive Monte Carlo particle transport simulation code, to simulate tritium production based on neutron irradiation conditions, as listed in Table 5.1. It requires defining several module components that comprise the simulation input, for instance, Parameters, Material, Source, and Tally. The following sections detail the essential parts to clarify the process. Lastly, the outstanding results are presented.

B.2.1 Material

This part generally defines the properties of the materials used in the simulation, for instance, atomic or molecular composition, density, etc. This information constructs the simulation geometry.

Figure B.2 represents the simplified geometry for the simulation. The container was depicted with an integrated figure of a cylinder and two hemispheres based on the shape [2] and the thickness measured with a vernier scale. Likewise, the quartz tube was also illustrated based on the inner and outer diameters. The cotton occupied the space between them. The outside of the container was set to the void. As shown in Figure 3.4, the pebbles were simplified to spheres 1 mm in diameter. It is challenging to pile them up randomly on PHITS as the real thing. Instead, they were nested in a square column. Ultimately, the most critical factor for simulating tritium production is the Li density. Therefore, this work sacrificed their geometric shapes but maintained the Li density consistent with the neutron-irradiated samples. The simulated LTZO pebbles had no grains and pores. As the previous study [3] reported, the density was tailored to 83.4% of the theoretical density. The ratio of ^{6}Li and ^{7}Li was set equal to the natural abundance. Except for the pebbles, the space inside the quartz tube was placed to void.

Table. B.1. Objects in the Material module on PHITS.

	Object	**Color**	**Density [g cm^{-3}]**	**Ref**
Pebble	$Li_{2.15}Ti_{0.8}Zr_{0.2}O_{3.075}$	Pastel cyan	3.43×0.834	[3]
Quartz tube	SiO_2	Pastel blue	2.563	[4]
Cotton	Cellulose, $C_6H_{10}O_5$	White	1.5	[5]
Container	Polyethylene, $(C_2H_4)_n$	Gray	0.938	[6]
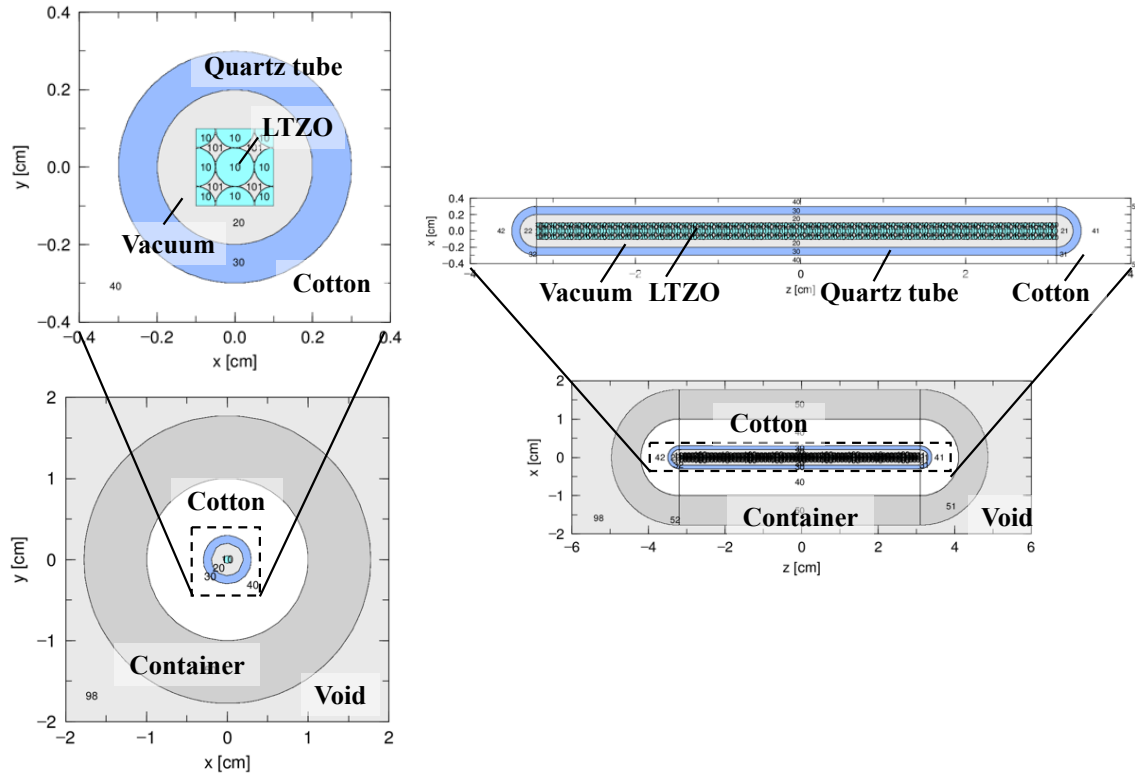
Figure B.2. Geometry of the irradiation sample on PHITS.

(Left) X-Y cross-section profile at z = 0. (Right) X-Z cross-section profile at y = 0.
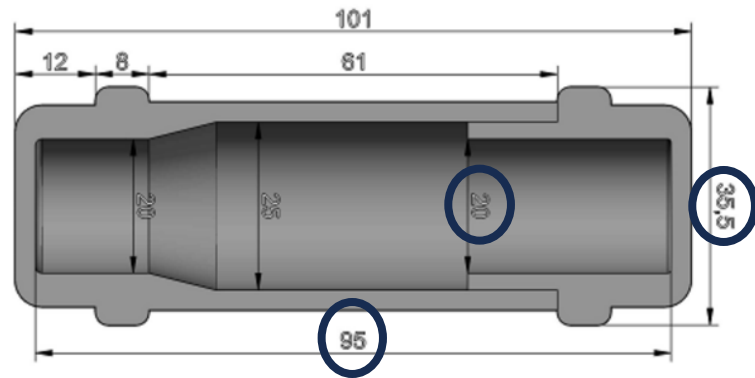
Figure B.3. The actual polyethylene container geometry [2].

This work referred to the numbers circled in black to establish the geometry.

B.2.2 Source

This part generally defines the characteristics of the particle source, such as source type (cylinder, rectangular, etc.), source energy, the spatial and angular distribution of the particles, etc.

The neutron particle incident profile is essential for the simulation of tritium production. Neutron injection into the sample geometry was set to isotropically come in all directions from a cylinder surrounding the created geometry with a height of 10 cm and a diameter of 2.0 cm. This is because multiple fuel rods and graphite reflectors surround the sample-loaded Pn-2 [2, 7]. Figure B.4 illustrates the neutron energy spectrum, carefully reproduced based on the official KUR report [2]. Figure B.5 exhibits the neutron cross-section of ^{6}Li and ^{7}Li, indicating that ^{6}Li enormously contributes to tritium production, especially for the given neutron energy spectrum.
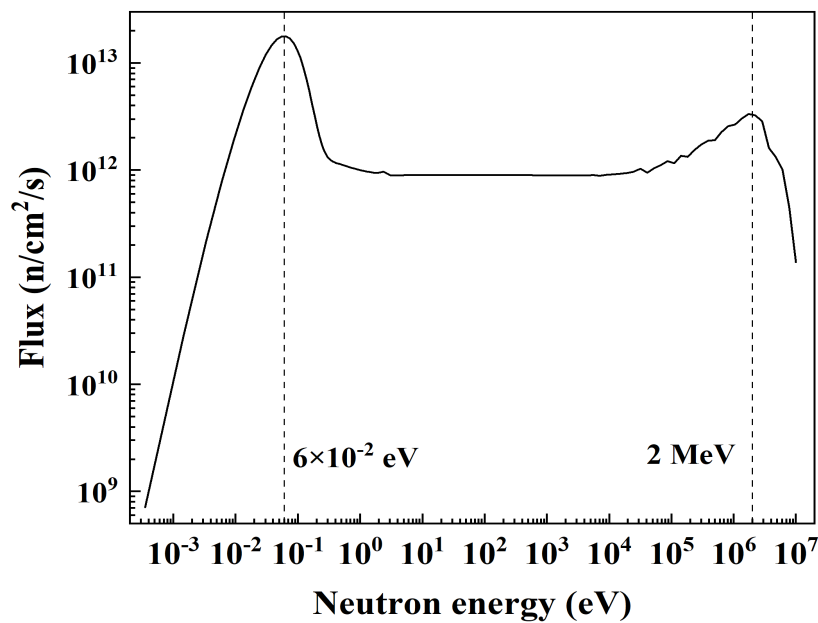
Figure B.4. Neutron energy spectrum at the Pn-2 [2].
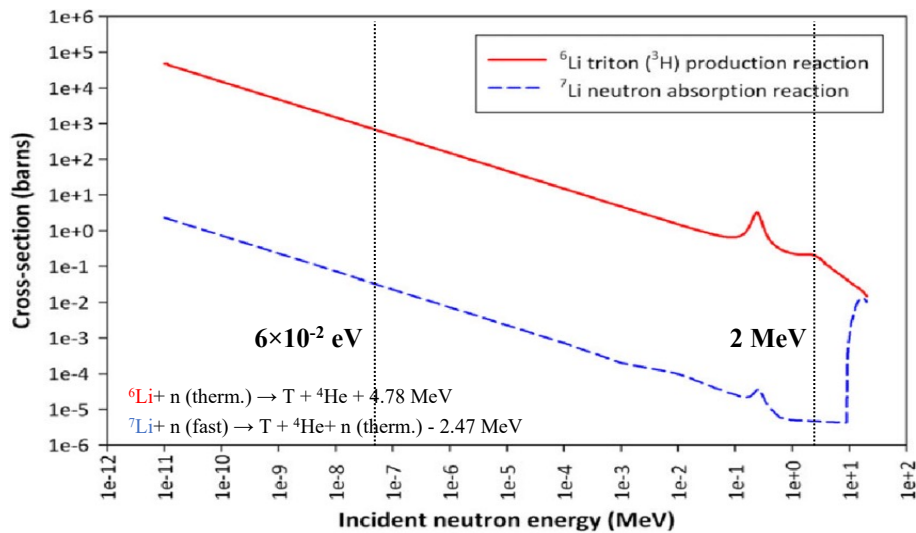
Figure B.5. Cross-section of Li isotopes [8].

B.2.3 T-Volume

This part defines volume within the simulation's geometry. It tracks specific quantities related to the particles as they interact within the specified volume, as in particle flux, energy deposition, production rates, etc. The Monte Carlo principle is employed to calculate the volume.

The tritium production simulation requires the volume of each LTZO pebble. As mentioned in section B.2.1, LTZO pebbles are described in various shapes nested in a square cylinder along the z-axis. Therefore, to ensure reliable outputs, the T-Volume tally iterated the calculation countless times until the error was less than 0.1%. Then, it was used to retain the tritium production and energy deposition to repeat the specific bunches of the neutron injections.

B.2.4 T-Product

This part returns particles and nuclei produced by nuclear reaction, decay, fission, and the input source particles. The energy and time distribution of produced particles and nuclei can also be obtained.

It is vital to carefully set the proper mesh width and choose the proper nuclei to visualize the produced nuclei energy spectrum. The target nuclear reaction is the ^{6}Li(n, α)T, as in equation (1.2). It creates a ^{4}He nuclide with 2.05 MeV and a ^{3}H nuclide with 2.73 MeV. As a result, Figure B.6 demonstrates that the setting environment successfully could produce them.
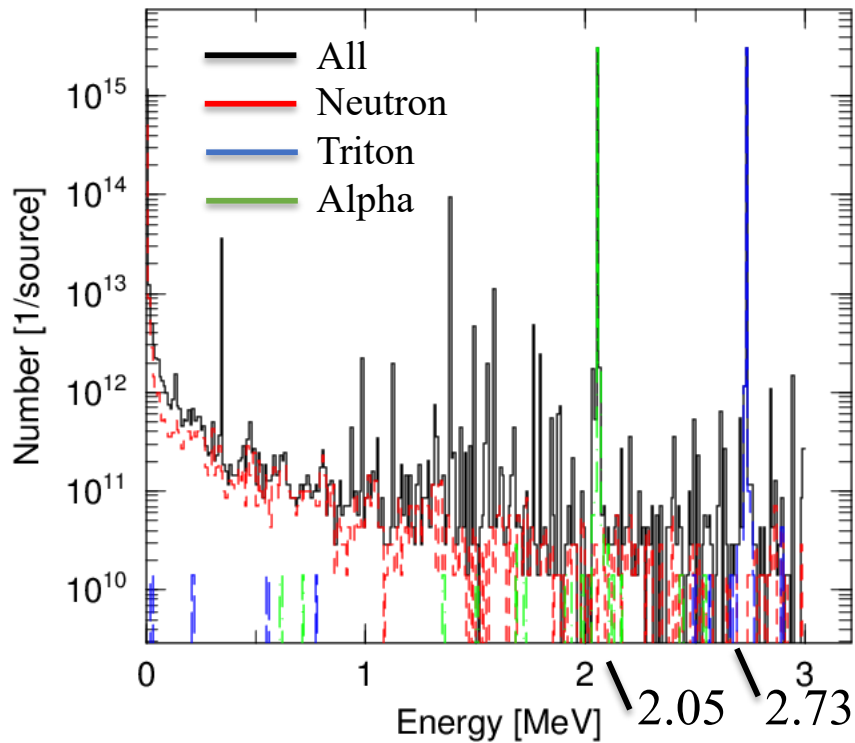
Figure B.6. Energy spectra of the incident neutrons, produced tritons, and helium.

B.2.5 T-Heat

This part outputs the imparted energy using the kinetic energy released per unit mass (KERMA) approximation. The energy that is eventually converted into heat is through the process of ionization of the charged particles.

Technically, the KERMA approximation is not applicable when considering the irradiation with the thermal neutron, and it misses the heat induced by the secondary generated gamma rays. However, Figure B.6 shows that the charged particles (i.e., ^{3}H and ^{4}He) are dominantly produced. Hence, the KERMA approximation can help estimate the temperature field during the neutron irradiation.

B.2.6 Results and Discussion

As seen in Figure B.7, the neutrons successfully hit the sample geometry thoroughly. This firmly denied the first item: scattering due to the light atoms and self-shielding due to ^{6}Li prevent neutrons from reaching the LTZO pebbles. Even in the case of the LTZO pebbles with ^{6}Li enriched to 90%, a noticeable difference was not found.
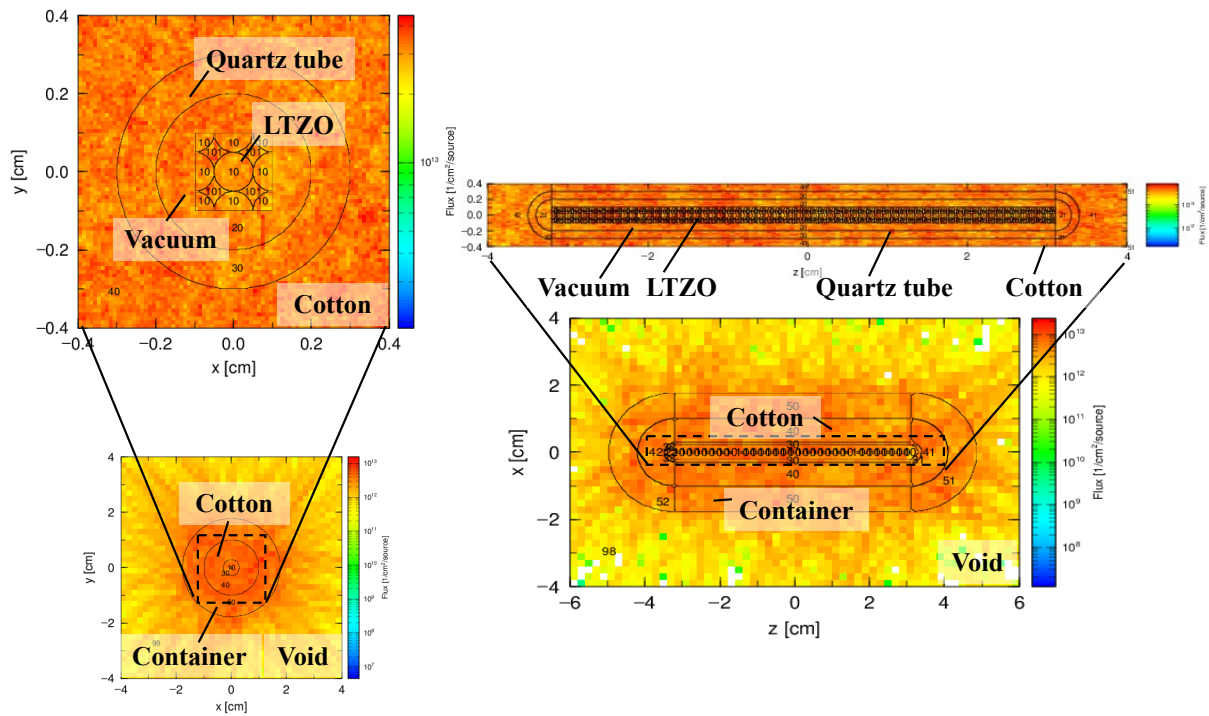
Figure B.7. Neutron particle profile in thermal neutron energy range (1×10^{-2} - 1×10^{-1} eV).
(Left) X-Y cross-section profile at z = 0. (Right) X-Z cross-section profile at y = 0.

Figure B.8 depicted that tritium was successfully produced as much as the theoretical value with minor relative errors, and most of the generated tritium was inside the quartz tube. This result implied the correctness of the second item: tritium is directly released from the Li sites into the air. This is because hot tritons are energetically excited enough to shake off the neighboring bonding energy, for example, Li-O and trap sites.
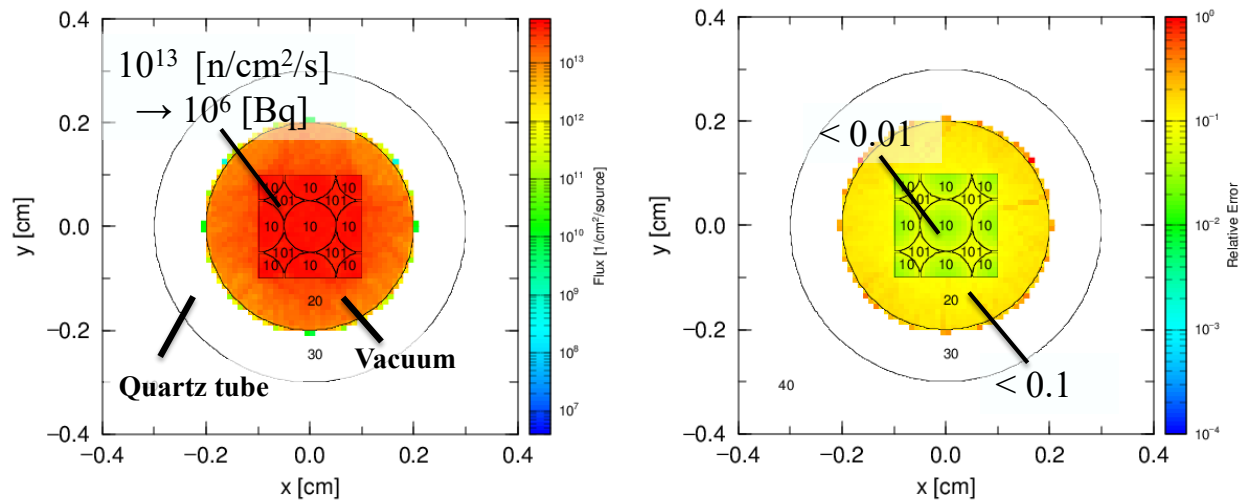
Figure B.8. Simulation results for (left) the tritium production and (right) the relative errors.

Figure B.9 reveals that the heat was mainly generated at the LTZO pebbles. Its volumetric heat was calculated to be approximately 10^2 MW m^{-3}. This figure agreed with the other reports [9, 10]. This value is large enough to raise the LTZO pebbles' temperature.
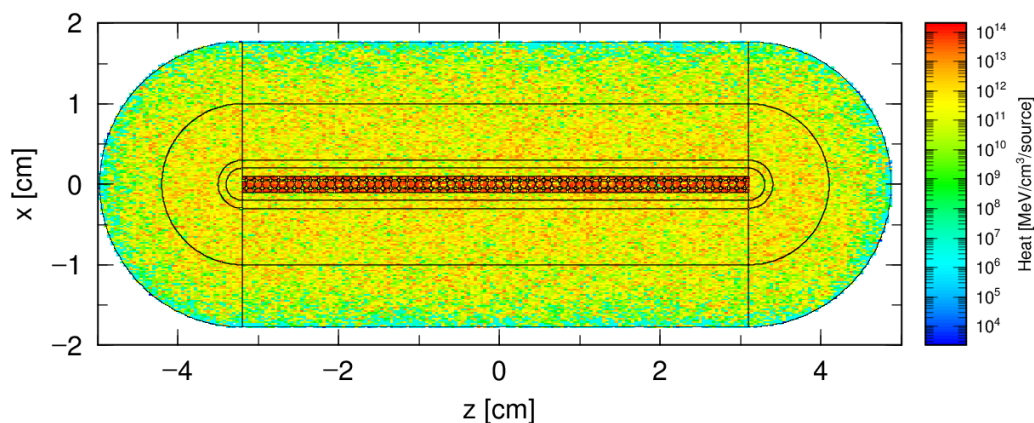
Figure B.9. Simulation results for (left) the tritium production and (right) the relative errors.

Given the simulation results, the experimental approach was refined to quantify the tritium precisely while cutting the quartz tube.

B.3 Heat Transfer Simulation

This work calculated the temperature distribution of the LTZO pebble during the thermal neutron irradiation. Given the thermal conductivity of LTZO, this work discusses the temperature distribution in a steady state.

B.3.1 Simulation Methodology

Heat flows within a substance by conduction when there is a temperature distribution within the substance. This thermal diffusion phenomenon is known as Fourier's law and is expressed as follows:

$$q = -\lambda \nabla T, \tag{B.1}$$

where q [W m^{-2}] is the heat flux crossing the substance, λ [W m^{-1} K^{-1}] is the thermal conductivity of the substance, and T [K] is the temperature. Generally, the differential equation for heat conduction can be derived by applying Fourier's law, considering the heat balance in finite volume elements within the substance. Given the volumetric heat, H [W m^{-3}], under the conditions of constant thermal conductivity, the differential equation can be written as follows:

$$\partial T / \partial t = a \nabla^2 T + H / c\rho, \tag{B.2}$$

$$a = \lambda / c\rho, \tag{B.3}$$

where a [m^2 s^{-1}] is the thermal diffusivity of the substance, c [J kg^{-1} K^{-1}] is the specific heat capacity of the substance, and ρ [kg m^{-3}] is the density of the substance.

In this work, nuclear reaction heat and nuclei decay heat are considered volumetric heat. Each nuclear reaction in Table 5.2 produces tremendous heat based on the mass-energy equivalence.

$$Q_i = (M_{\text{react}, i} - M_{\text{prod}, i}) c^2, \tag{B.4}$$

where i is the index for each nuclear reaction, Q [J] is the nuclear reaction heat, M_{react} and M_{prod} [kg] are the atomic mass of the reactants and products, and c [m s^{-1}] is the speed of light.

The radioisotopes start to decay as soon as it is created. There are various ways to decay, for instance, alpha, beta, and gamma decay. The decay heat, P [J], can be determined based on information on the energy of those particles in a nuclear database.

Therefore, based on equations (2.11), (2.16), and (2.17), the heat deposited by the reaction and decay heat during the neutron irradiation, h [W], can be described as follows:

$$h_{i\,(t)} = y_i Q_i + \lambda N_{\text{prod}, i} P_i. \tag{B.5}$$

$$h_{i\,(t)} = y_i (Q_i + P_i) - y_i P_i\, e^{-\lambda_i t}. \tag{B.6}$$

$$y_i = \sigma_i N_{\text{react}, i}\, \phi. \tag{B.7}$$

Hence, the volumetric heat, H, required to solve equation (B.2) is described using the volume of the substance, V [m^3], as follows:

$$H_{(t)} = \Sigma\, h_{i\,(t)}\, /\, V. \tag{B.8}$$

According to the specific ratio, some of the produced nuclei branch out to decay: beta or gamma decay. Considering the deposited decay heat in the pebble, whose diameter is 1 mm, gamma rays have too high a penetration power to deposit their energy. Therefore, only the maximum beta particle's energy described the decay heat, P. Above all, the reaction heat from ^{6}Li(n, α)T dominated the temperature field of LTZO according to Table B.2. As mentioned previously, the reaction heat is independent of time. Hence, the volumetric heat, H, was set to constant, 71 MW m^{-3}.

Table B.2. Energy deposited by each nuclear reaction and each radioisotope
right after 5-minute neutron irradiation in eV g^{-1} s^{-1}.

	^{6}Li(n, α)T	^{7}Li(n, γ)^{8}Li	^{18}O(n, γ)^{19}O	^{50}Ti(n, γ)^{51}Ti	^{92}Zr(n, γ)^{93}Zr	^{94}Zr(n, γ)^{95}Zr	^{96}Zr(n, γ)^{97}Zr
Q_i	$1.16{\times}10^{20}$	$2.47{\times}10^{16}$	$4.75{\times}10^{11}$	$6.48{\times}10^{15}$	$7.21{\times}10^{15}$	$1.52{\times}10^{15}$	$8.28{\times}10^{13}$
P_i	$2.42{\times}10^{11}$	$1.94{\times}10^{17}$	$5.78{\times}10^{11}$	$1.14{\times}10^{15}$	$3.96{\times}10^{2}$	$9.92{\times}10^{9}$	$1.36{\times}10^{11}$

Figure B.10 shows the radial build of Figure B.1. Its geometry, each material's physical properties concerning heat transfer, and the ambient temperature were given. These pieces of information guessed the macroscopic temperature distribution between the pebble and surrounding materials. The LTZO pebbles were piled up in a row because the major heat transfer mechanism was uncertain: either to the quartz tube through point contact or the surrounding air. Air and CO_2 were assumed to be at atmospheric pressure. Temperature dependence of the properties was not considered. It was assumed to neglect heat transfer in the altitude, polar, and azimuthal angle directions.
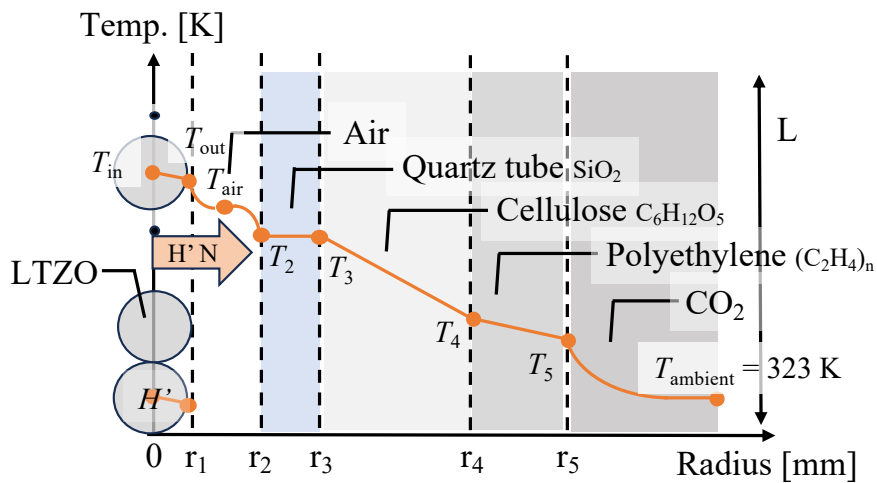
Figure B.10. The heat transfer model.

While the detailed temperature distribution within the substances is unnecessary, the temperature at both ends is necessary to explore the third item of potential causes. In general, the heat transfer can be expressed using the concept of thermal resistance.

$$Q = (T_{b1} - T_{b2}) / R, \tag{B.9}$$

where Q [W] is the heat, T_{b1} and T_{b2} [K] are the temperature at both ends, and R [K W^{-1}] is the resistance of the heat transfer.

In a steady state, the volumetric heat per pebble, H' [W m^{-3}-pebble], was conducted inside the pebble, and then, the total heat, NH' [W m^{-3}-pebble], was transferred to the subsequent materials. N [-] denotes the number of the pebbles. Therefore, equation (B.2) can be modified with the parameters shown in Figure B.10.

$$H' = (T_{in} - T_{out}) / R. \tag{B.10}$$

$$R = \frac{r_1}{4\pi r_1^2\, \lambda_{Li2TiO3}}. \tag{B.11}$$

The heat transfer to the air can be expressed with the heat transfer coefficient, h [W m^{-2} K^{-1}], of the air and heat transfer area of the pebble, A [m^2].

$$H' = h_{air}\, (T_{out} - T_{air})\, A. \tag{B.12}$$

Then, the heat was transferred from the air to the surrounding materials, which were cylindrical with different radii, as shown in Figure B.10 can be expressed using the overall heat transfer coefficient, k [W m^{-1} K^{-1}]. Therefore, equation (B.9) can be modified as follows:

$$NH' = k\, (T_{air} - T_{amb})\, L. \tag{B.13}$$

$$k = \frac{2\pi}{\frac{1}{h_{air}r_5} + \frac{1}{\lambda_{SiO2}}\ln\!\left(\frac{r_3}{r_2}\right) + \frac{1}{\lambda_{C6H12O5}}\ln\!\left(\frac{r_4}{r_3}\right) + \frac{1}{\lambda_{C2H4}}\ln\!\left(\frac{r_5}{r_4}\right) + \frac{1}{h_{CO2}r_5}}. \tag{B.14}$$

The temperature of the materials (i.e., T_2, T_3, T_4, and T_5) can be obtained by modifying equation (B.10) appropriately. Table B.3 summarizes all the parameters used in this work.

Table B.3. List of the parameters used to guess the temperature at the specific points.

Property	H'	N	$\lambda_{Li2TiO3}$	λ_{SiO2}	$\lambda_{C6H12O5}$	λ_{C2H4}	h_{air}	h_{CO2}
Value	3.72×10^{-2}	250	2.2	11.715	0.045	0.403	20	20
Unit	W Vol^{-1}-pebble	-	W m^{-1} K^{-1}				W m^{-2} K^{-1}	
Ref			[11]	[12]	[13]	[6]		

Geometry	r_1	r_2	r_3	r_4	r_5	L	A
Value	0.5	2	3	10	17.8	95	3.14
Unit	mm	mm	mm	mm	mm	mm	mm^2

B.3.2 Results and Discussion

Figure B.11 displays the temperature distribution in a steady state. It rose to 1790 K in the core of the LTZO pebbles, slightly below the melting point of 1813 K [14]. The total heat released into the air was only 9.31 W, as large as light bulbs, smartphone chargers, etc. Nevertheless, it was significant, considering the heat transfer. The absorbent cotton, whose thermal conductivity is tiny, also impeded the heat transfer. As a result, these figures appeared reasonable for getting the cotton burned and the polyethylene container colored.
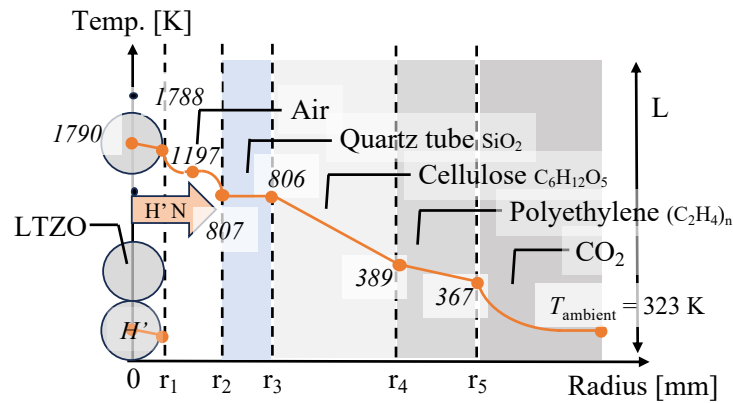
Figure B.11. Temperature distribution in a steady state when the heat transfers to the air.

In contrast, Figure B.12 displays the temperature distribution in the case in which heat was conducted directly from the pebbles to the quartz tube. The temperature of the pebbles dropped substantially to 810 K. The three-digit decrease in resistance between the air and the quartz tube facilitated the heat transfer. In fact, all pebbles had point contact with one another, so the heat must have been conducted between them towards the quartz tube. 810 K was high enough for tritium to diffuse through the grains.
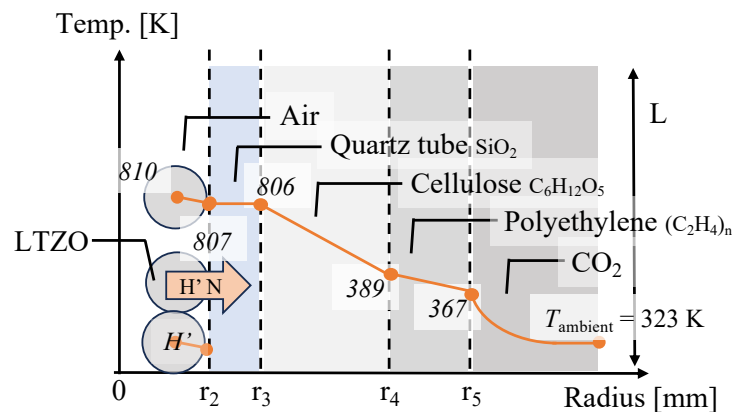
Figure B.12. Temperature distribution in a steady state, directly conducting the heat to the quartz tube.

Once it reached the surface of the grains, it would seem natural that it would interact with the water vapor in the quartz tube and be released into the gas phase. As seen in Figure 5.3 and Table B.2, even on timescale when some nuclides drastically drop the decay energy, energy deposition was 3- or 5-digit smaller than the ^{6}Li(n, α)T reaction heat. It did not contribute to raising the temperature during the cooling time.

B.4 Summary

The appendix explores the possibility of the massive gap between the experimental tritium recovery amount and the theoretical tritium production. Here is the list of the key findings through the simulation and calculation.

Key Findings:

1. **Thermal Neutron Flux**: PHITS firmly denied the disparities in the thermal neutron flux originating from the scattering and self-shielding.

2. **Tritium Direct Release to the Air**: PHITS showed the possibility that some of the tritium produced with excessive energy jumped off into the air.

3. **Nuclear Reaction Heat and Decay Heat**: In the case of thermal neutron irradiation, the simple manual calculation said the ^{6}Li(n, α)T reaction heat dominated the temperature field.

4. **Temperature Distribution**: The manual calculation disclosed that the LTZO pebbles reached 810 K during the neutron irradiation. It was high enough for tritium to diffuse towards the gas phase.

References

[1] T. Sato et al, J. Nucl. Sci. Technol. 55, (2018), 684-690, doi: 10.1080/00223131.2017.1419890.

[2] Kyoto University Research Reactor Institute, Pressurized Air Transport Pipe Irradiation Facility [圧気輸送管照射設備]. Retrieved November 22, 2023, from http://www.rri.kyoto-u.ac.jp/JRS/inst/pn.pdf.

[3] T. Hoshino, Nucl. Mater. Energy, 9, (2016), 221-226, doi: 10.1016/j.nme.2016.05.004.

[4] S. Tsuneyuki et al., Phys. Rev. Lett., 61, (1988), 869-872, doi: 10.1103/PhysRevLett.61.869.

[5] PubChem (n.d.), Cellulose. Retrieved November 22, 2023, from https://pubchem.ncbi.nlm.nih.gov/compound/Deae-cellulose.

[6] National Center for Forensic Science (n.d.), Thermal Properties: Databases Online Interface. Retrieved November 22, 2023, from https://ncfs.ucf.edu/burn_db/Thermal_Properties/material_thermal.html.

[7] Kyoto University Research Reactor Institute, KUR Annual Operating Plan [KUR 年間運転計画]. Retrieved November 22, 2023, from https://www.rri.kyoto-u.ac.jp/KURdiv/info_kur.html.

[8] E. Bezak et al., Radiat. Prot. Dosimetry, 167, (2015), 591–601, doi: 10.1093/rpd/ncu362.

[9] J. Shimwell et al., Nucl. Fusion, 59, (2019), 046019, doi: 10.1088/1741-4326/ab0016.

[10] R. Forte et al., Nucl. Mater. Energy, 29, (2021), 101058, doi: 10.1016/j.nme.2021.101058.

[11] J. W. Davis et al., J. Nucl. Mater., 232, (1996), 65-68, doi: 10.1016/0022-3115(96)00396-0.

[12] Thermtest Instruments (n.d.), Materials Thermal Properties Database. Retrieved November 22, 2023, from https://thermtest.com/thermal-resources/materials-database.

[13] P. B. Jelle, Start-Up Creation, (2016), 129-181, doi: 10.1016/b978-0-08-100546-0.00008-x.

[14] LTS Research Laboratories, Inc., Safety Data Sheet, Lithium Titanium Oxide. Retrieved November 22, 2023, from https://www.ltschem.com/msds/Li2TiO3.pdf.

Acknowledgments

I want to express my heartfelt appreciation to Professor **Y. Watanabe** and Associate Professor **K. Hashizume** for insightful reviewing as a vice chair examiner in my dissertation committee. Their constructive feedback considerably improved the quality of my work.

Furthermore, I cherish the assistance and small talks with all of my lab mates, Dr. **I. K. Aji**, Mr. **M. Portuphy**, Mr. **R. Oyama**, Mr. **K. Kubo**, Mr. **Y. Hara**, Mr. **T. Matano**, Mr. **A. Yamasaki**, Mr. **H. Isogawa**, Mr. **Y. Takahashi**, Mr. **J. Haruta**, Mr. **T. Matsumoto**, Mr. **Y. Wada**, Mr. **Z. L. Yang**, Mr. **H. N. Sun**, Mr. **T. Ichikawa**, Mr. **S. Katayama**, Mr. **S. Nakamura**, Mr. **K. Masuta**, Mr. **N. Yamada**, Mr. **T. X. Hu**, Mr. **S. Iwata**, Mr. **Y. Uwatoko**, Mr. **K. Asao**, Ms. **H. Inoue**, Mr. **S. Kobayashi**, Mr. **Y. Setoguchi**, Mr. **H. Nakamura**, and Ms. **Y. Mori**. Their diverse expertise always brought different viewpoints to my work through fruitful and informative discussions, deepening and broadening my knowledge and core competencies.

Special thanks to our secretary, Ms. **M. Katayama,** and predecessor, Ms. **M. Sakamoto**, for their unwavering daily support and prompt completion of paperwork, especially for my business trips, ensuring a conducive environment for my research endeavors.

Lastly, my **family** and **friends** have been my anchors through this voyage. Their unconditional love, continuous support, and considerable encouragement have been my refuge. Their belief in my capabilities fueled my perseverance and helped me hang in there.

March 2024

Akito Ipponsugi